ISSN: 1949-243X Volume 2, Number 2, May 2010

Scientific Research

Energy and Power Engineering

ISSN: 1949-243X

www.scirp.org/journal/epe

Journal Editorial Board

ISSN: 1949-243X (Print) ISSN: 1947-3818 (Online)

http://www.scirp.org/journal/epe

Energy and Power Engineering, **2010, 2, 73-136**
Published Online May 2010 in SciRes (http://www.SciRP.org/journal/epe/)

TABLE OF CONTENTS

Volume 2 Number 2 May 2010

Energy and Power Engineering (EPE)

Journal Information

SUBSCRIPTIONS

The *Energy and Power Engineering* (Online at Scientific Research Publishing, www.SciRP.org) is published quarterly by Scientific Research Publishing, Inc., USA.

Subscription rates:

Print: $50 per issue.
To subscribe, please contact Journals Subscriptions Department, E-mail: sub@scirp.org

SERVICES

Advertisements
Advertisement Sales Department, E-mail: service@scirp.org

Reprints (minimum quantity 100 copies)
Reprints Co-ordinator, Scientific Research Publishing, Inc., USA.
E-mail: sub@scirp.org

COPYRIGHT

PRODUCTION INFORMATION

For manuscripts that have been accepted for publication, please contact:
E-mail: epe@scirp.org

Energy and Power Engineering, **2010, 2, 73-77**
doi:10.4236/epe.2010.22011 Published Online May 2010 (http://www.SciRP.org/journal/epe)

Dopant Implantation into the Silicon Substrate with Non-Planar Surface

Gennady A. Tarnavsky[1], Evgenii V. Vorozhtsov[2]
[1]*Institute of Computational Mathematics and Mathematical Geophysics, Siberian Branch of the Russian Academy of Sciences, Novosibirsk, Russia*
[2]*Khristianovich Institute of Theoretical and Applied Mechanics, Siberian Branch of the Russian Academy of Sciences, Novosibirsk, Russia*
E-mail: *vorozh@itam.nsc.ru*
Received January 3, 2010; *revised February* 9, 2010; *accepted March* 29, 2010

Abstract

The influence of technological process parameters (aiming angle and implantation energy) on the distributions of dopant concentrations in a silicon substrate is investigated by computer modeling.

Keywords: Computer Modeling, Silicon Doping, Implantation, Donor, Acceptor Dopants

1. Introduction

Advanced technologies of the design and manufacturing of nano-electromechanical systems (NEMS technologies) are based on complex physical, chemical, and mechanical processes. These processes constitute a chain of base stages (segments) of the industrial production of various NEMS devices.

The doping is one of important technological processes. This is the process of adding the dopants of the acceptor and/or donor type (phosphorus, arsenic, antimony, boron, gallium, etc.) to a silicon plate for the purpose of creating the zones of increased conductivity of the n- and p-type in semiconductor for the arrangement of the diode and transistor channels.

The doping can, besides, be aimed at achieving some technological goals. For example, the doping by boron stops the process of the basic material etching.

The ion implantation, which consists of the introduction in the semiconductor material of ionized atoms accelerated in the electric field and possessing a high energy is at present the most efficient and widely used doping technology. This technology requires specialized complex setups, but it is much more accurate than the diffusion method, and it is applied for creating the hidden layers, the p- and n-pockets, domains in the chip, which form the transistor channels.

Computer experiments, which are more mobile and much cheaper in comparison with the physical ones (if one does not account for the expenses of intellectual efforts), with a possibility of considering hundreds and even thousands of variants, with a rapid and efficient analysis of their results as well as with a capability of increasing the levels of the employed physical and mathematical models, play an increasing role in the design of new semiconductor materials.

In the present work, the influence of technological process parameters (aiming angle and the implantation energy) on the distributions of dopant concentrations in a silicon substrate is investigated by computer modeling based on a new mathematical formulation proposed by one of the present authors (G.A.T.).

2. Computer Toolbox

The program complex NanoMod [1] is intended for conducting the scientific research and applied developments in the field of microelectronics, including the microprocessor technology. The complex may be used for teaching the specialists, postgraduates, and students in the given knowledge area.

The computer toolbox NanoMod has been developed on the basis of advanced original algorithms for modeling the electrophysical, thermochemical, and mechanical processes (see [2] and the bibliography therein) for computer support of the automated design of nanostructured semiconductor materials.

In the present work, we present the results obtained by using one of the segments of the program complex—the IMPL solver (IMPLantation).

The work was financially supported by the Russian Foundation for Basic Research (grant No. 08-07-12001-ofi).

2.1. The IMPL Solver

The algorithm of the segment is based on the method for numerical computation of the Gauss law for the distribution of dopant concentrations of various elements introduced in a silicon substrate by the ion implantation technique (see [3]):

$$C_1(\xi) = A \cdot \exp(B \cdot (\xi - \xi_0)^2) . \quad (1)$$

The coordinate direction ξ in (1) is the direction of ions motion from the acceleration device to the substrate. This direction is generally not perpendicular to the substrate surface but makes the angle α_I with the normal to it. The ξ coordinate is measured from the point of the start of the ion introduction into the substrate with the increasing ξ value at the motion deep into the material. The quantities A, B, and ξ_0 are the constants depending on physical factors—the type S_I and the dose D_I of the implant, the energy of ions acceleration E_I :

$$A = A(S_I, D_I, E_I) , \quad B = B(S_I, D_I, E_I) ,$$

$$\xi_0 = \xi_0(S_I, D_I, E_I) . \quad (2)$$

The quantity ξ_0 in (2) is the depth of the maximum introduction of ions into the substrate—the peak of the Gauss distribution (1) with the dopant concentration, which drops exponentially deep into the material and towards its surface.

In the presence of protective masks on the substrate surface, which are opaque for the flux of implanted ions, one can account for the dopant propagation in the tangential direction under the mask along the second coordinate direction η normal to ξ (see the details in [4]):

$$C_2(\eta) = F \cdot \mathrm{erf}(k \cdot (\eta - \eta_0)) , \quad (3)$$

$$F = F(S_I, D_I, E_I) , \quad k = k(S_I, D_I, E_I) ,$$

$$\eta_0 = \eta_0(S_I, D_I, E_I) . \quad (4)$$

The quantities F, k, and η_0 in (3), (4) have the following meaning. The parameter η_0 is the coordinate of the mask edge, from which the value of the η coordinate is measured (under the mask), and parameters F and k are the constants depending on the physical parameters of the problem.

The resulting concentration is expressed in the form

$$C(\xi, \eta) = C_1(\xi) \cdot C_2(\eta) . \quad (5)$$

In the (x,y) coordinates of real problems at a non-planar substrate surface and/or nonzero value of the implantation aiming angle, the function $C(x,y)$ in (5) cannot be presented in the form of a splitting into the product of $C_1(x)$ and $C_2(y)$. Because of this, the numerical algorithm for computing the problem (1)-(5) in (ξ,η)-coordinates is used in the solver. This solution is then represented in the (x,y)-coordinates.

The values of quantities S_I, D_I, E_I, and α_I are input by the user in accordance with the problem formulation. The values of parameters A, B, F, k, ξ_0, and η_0 are contained in a specialized database of the complex and are input by the system for supporting the tasks without involving the user.

It is to be noted that the completeness of tables of these parameters and their numerical values, which are permanently refined in physical experiments (executed on the advanced research setups) and which are input in a timely fashion in the solver database, increases the computer toolbox efficiency.

3. Results of Computer Modeling

3.1. Problem Formulation

The solution of problem (1)-(5) is to be found in the region R:

$$x \in [0, x_{\max}] , \quad y \in [0, y_{\max}] , \quad (6)$$

consisting of two subregions—the external medium subregion R_V and the silicon subregion R_{Si}, which are separated by the boundary

$$y = Y_{Si}(x) . \quad (7)$$

It is assumed here that the doping is made only in R_{Si} that is at $y < Y_{Si}$, and the concentrations of implanted dopants are equal to zero in R_V.

A discrete computational grid with the number of nodes N_x and N_y along the x- and y-directions, respectively, is generated in (6) for the numerical solution of problem (1)-(5). The appropriate values of N_x and N_y were determined within the framework of the grid refinement study as follows: several runs were done with sequentially increasing values $1 < N_x^{(1)} < \ldots < N_x^{(k-1)} < N_x^{(k)}$, $N_y^{(1)} < \ldots < N_y^{(k-1)} < N_y^{(k)}$, and the results obtained for sequential pairs $(N_x^{(k-1)}, N_y^{(k-1)})$ and $(N_x^{(k)}, N_y^{(k)})$ were compared with one another. As soon as the difference in the results obtained for these pairs becomes sufficiently small, the last pair $(N_x^{(k)}, N_y^{(k)})$ is chosen as the final one for the modeling. In the scope of problems presented below the modeling was carried out in the region with $x_{\max}$ = 100 nm and $y_{\max}$ = 60 nm. For this region, the grid with N_x = 151 and N_y = 151 was found to be appropriate. The following values of problem parameters were used in (2) and (4): the implantation of phosphorus P, boron B, and arsenic As was investigated (parameter S_I), the implant dose was fixed ($D_I = 10^{15}$ cm^{-3}), and the implantation energy E_I was varied from 5 eV to 20 eV.

The values of concentrations obtained in computations are presented in dimensional units [cm^{-3}].

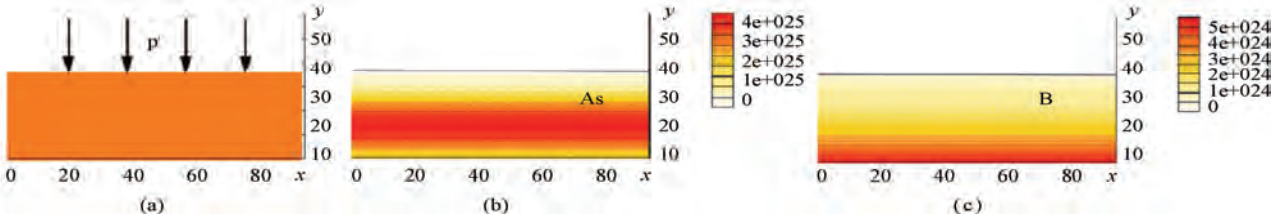

Figure 1. Implantation of dopant donor and acceptor admixtures into the silicon Si substrate with planar surface. The process scheme (a), the distributions of the concentrations of the arsenic As (b) and boron B (c). Implantation energy 15 eV.

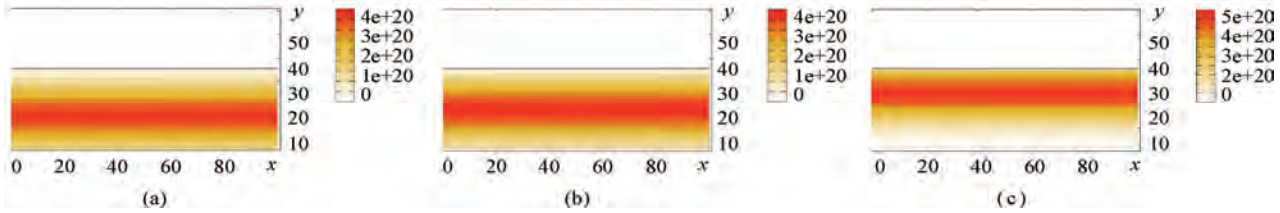

Figure 2. Phosphorus P implantation into the silicon Si substrate with planar surface. Implantation energy 15 eV. Distributions of concentrations of P in Si at the aiming angle of implantation 0° (a), 30° (b), and 60° (c).

3.2. Implantation into the Silicon with Planar Surface

Consider the results of problem solution at a constant value of $Y_{Si}(x) = 35$ in (7), the implantation energy 5 eV, and three doping types: As, B, and P.

Figure 1 illustrates the results of computing the segment. The implantation scheme and the distribution of the arsenic As and boron B concentrations in the silicon Si are shown.

Note that for the same implantation energy, the penetration depth of B in Si is higher than the penetration depth of As in Si. The maximum of the As distribution takes place at $y = 20$ (at the depth of 15 nm from the surface), and in the case of B, it takes place at $y = 0$ (the depth of 35 nm).

The maximum of the P concentration (**Figure 2(a)**) lies at the depth of 20 nm ($y = 15$). Thus, the phosphorus penetrates the silicon deeper than the arsenic for the same implantation energy, but it yields to boron in terms of this figure.

The implanted layer width is the largest in the case of As, and it is the least in the case of B. The process of dopant diffusion with time spreads this distribution at a speed depending on several factors (the temperature, the crystal lattice type, etc.).

Let us analyse the influence of the implantation aiming angle α_I. **Figure 2** shows the results of computing the phosphorus implantation for the values $\alpha_I = 0^\circ, 30^\circ$, and 60° (**Figures 2(a)**, **(b)**, and **(c)**, respectively). The angle α_I is measured from coordinate lines x = const, in the given problem it is measured from the direction normal to the basic substrate surface.

One can predict a priori that as a result of modeling the 2D problem, one must obtain the 1D structures of the distribution of concentrations $C = f(y)$, and such a problem statement is, besides the obtaining of scientific data, a test for the correctness of the functioning of the computational algorithm and the computer code implementing it.

Computed results correspond to the predictions: the distributions of phosphorus concentrations depend only on the y-coordinate.

The following fact takes place here: with increasing angle α_I, the penetration depth of P in Si drops, and it is naturally directly proportional to $\cos\alpha_I$, which is seen in **Figure 2**.

The distribution functions $C(\alpha_I, y)$, where α_I is considered as a parameter, correlate with one another under the variation of α_I with small differences.

So the function $C(60^\circ, y)$ has a narrower localization than $C(0^\circ, y)$, and its maximum is by about 15% higher. The form and the digital values of function $C(30^\circ, y)$ take the intermediate position between $C(0^\circ, y)$ and $C(60^\circ, y)$.

The differences in functions are due to the proximity of the Si boundary to the y-coordinate of the maximum of the Gauss distribution (1), and the "tail" of this distribution is "cut off" by the substrate surface.

3.3. Implantation into a Substrate with Non-Planar Surface

Consider the results of computer modeling of the phos-

phorus P implantation into the silicon Si with a non-planar surface under the variation of the aiming angle α_I and the activation energy E_I.

Figure 3(a) shows the configuration (the sizes are in nm) of the Si base substrate with the grooves cut therein. The stage of the technological cycle of operations with such configurations often takes place at the formation of semiconductor materials with given electrophysical properties of NEMS units, in particular, the elements of three-gate nano-transistors of SON designs ("silicon-on-nothing", see, for example, [5,6]).

Figures 3(b) and **(c)** show the distributions of $C(x,y)$ for the values $\alpha_I = 0^\circ$ and 60°, respectively.

At $\alpha_I = 0^\circ$, the dopants form the domains with a narrow localization, whose sizes are of the order of 5-10 nm and maxima of the penetration depth of about 7-8 nm (for the given implantation energy E_I = 5 eV. Note that in the zones of deep grooves, the implant reaches the substrate lower edge (the bottom).

At the implantation under a larger angle $\alpha_I = 60^\circ$ (**Figure 3(c)**) the doping domains naturally "turn" to the implant flow direction.

At such a nano-relief of the surface, shadow zones arise in the substrate. So the concentration of P is insignificant in the left Si bump, and on the boards of the grooves and at the plate bottom, the concentration $C(x,y)$ is nearly equal to zero.

Figure 4 illustrates the influence of the implantation energy E_I at a fixed aiming angle $\alpha_I = 30^\circ$ and the same nano-relief of the surface. An increase in E_I from 5 eV (**Figure 4(a)**) to 10 eV (**Figure 4(b)**) and so on, up to 15 eV (**Figure 4(c)**) alters significantly the pattern of the P distribution in Si.

The location, sizes, and intensity of doping spots prove to be variable. So, in particular, a doping domain arises at E_I = 5 eV in the central bump. Although it has a low intensity and a small size, it is well noticeable. At E_I = 10 eV, this domain is smeared significantly, and at E_I = 15 eV, the central bump is "transparent" for the implant flux, which "passes" through it and locates in the left segment of the substrate configuration.

The concentration of P in the left segment depends substantially on E_I and alters from a small domain (**Figure 4(a)**) to the formation of a vast zone (**Figure 4(c)**).

The right segment of the substrate configuration, as the non-obscured one, is more conservative to the E_I variation: the doping domain has here approximately equal sizes, but with increasing E_I it naturally shifts deep into the substrate down to its very bottom (**Figure 4(c)**).

Note in conclusion that the function $C(x,y)$ determines the arrangement in Si of the zones of an elevated electric conductivity, in which the arrangement of the channels of nano-transistors is possible (see, for example, [6,7]).

3.4. Miniaturization of NEMS: Problems of Mathematical Modeling

The improvement of industrial production of the electronics and the passage, during the last 5 years, from the 130 nm technologies to 90 nm, 65 nm, 45 nm, 32 nm, and 22 nm technologies puts in foreground new very complex problems of the mathematical modeling of electrophysical, thermochemical, and mechanical processes, which are used in these technologies, within the framework of a continuum model.

So the computational region size of the problem R,

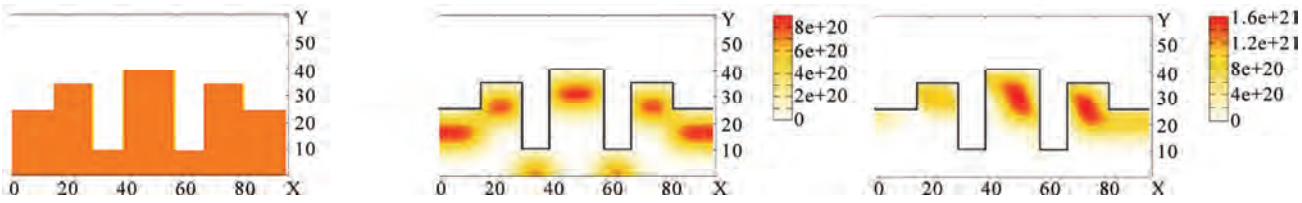

(a) (b) (c)

Figure 3. Phosphorus P implantation into the silicon Si substrate with a non-planar surface. The substrate configuration (a), distributions of the concentrations of P in Si at the aiming angle of implantation 0° (b) and 60° (c). Implantation energy 5 eV.

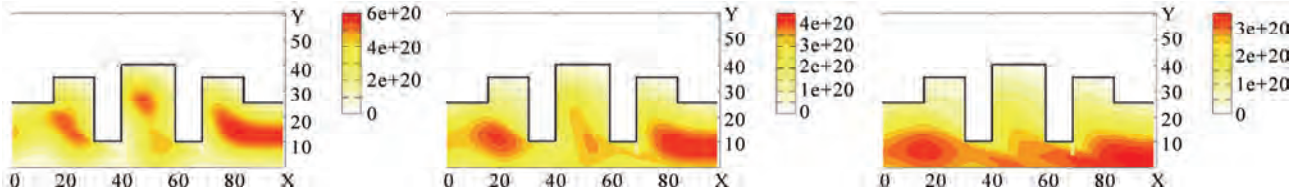

(a) (b) (C)

Figure 4. Phosphorus P implantation into the silicon Si substrate with non-planar surface. Distributions of the concentrations of P in Si at the aiming angle of implantation 30° and the implantation energy 5 eV (a), 10 eV (b), and 15 eV (c).

amounts, as a rule, already to about 100 nm (it is different in different coordinate directions depending on problem formulation).

Let us write down some physical characteristics of the silicon Si (at the temperature of about 300 deg. K and the pressure of 1 atm):

– 12 nm, the de Broile wave length (L_1);

– 0.54 nm, the crystal lattice step (L_2);

– 0.12 nm, the atom size according to Melvin-Hughes (L_3).

Comparing the R values with the values of L_1, L_2, and L_3 one can draw some important conclusions.

First, since R is higher than L_1 (the conditional boundary of the onset of the manifestation of quantum effects in Si), much higher than L_2, and much higher than L_3, then the continuum model is (still) well valid and applicable.

Second, there takes place, however, the following. Let a grid of N nodes be used in computation. The grid step is then $d = R / N$. At R = 100 nm and N = 100 we have d = 1 nm. Thus, the grid step d is less than L_1, is comparable with L_2, and is higher than L_3.

While aiming at increasing the accuracy of computation in the "classical" cases (we leave aside the bifurcation situation) one should increase N, for example, up to 1000 nodes. In this case, the grid step d equals 0.1 nm, and it is comparable with the silicon atom size L_3 and by a factor of five less than L_2, that is at the grid generation, each four nodes of five get into the inter-atomic space of the crystal lattice.

Thus, it becomes indefinite, what a process is modeled. Generally speaking, these considerations are not quite correct because an "averaging" of the real substance in which there are neither atoms nor their groups in the lattice is assumed at the use of the continuum model, where one can formulate a continuous differential problem in which the processes are described by differential equations, for example, diffusion equations with empirical coefficients obtained from reality (the standard or prestressed silicon, temperature, etc.).

The discretization of a continuous problem (the computational algorithm construction) naturally introduces its problems (approximation, convergence, solution uniqueness). These problems, however, have quite a different character and have nothing common to do with the problems of the adequacy of the continuum model as applied to real processes.

We can summarize the above said as follows. The model of continuum on the sizes of 100 nm is, on the whole, still sufficiently correct, but the *local* modeling of structures already requires a special analysis and the caution at the interpretation of obtained numerical results.

The advanced technologies enable the manufacturing of NEMS with sizes of elements less than 10 nm. So the two-layer gate dielectrics are used in the NEMS transistors. The first layer is a thermal silicon dioxide SiO_2 1 nm or less thick. The second layer is the silicon nitride Si_3N_4 (or a mixture of the oxide and nitride); it has about the same thickness. At such sizes, the accuracy of computing the oxidation process within the framework of the continuum model becomes very questionable. It is required to use more complex physical and mathematical models and the computational algorithms implementing them.

A passage to the quantum-mechanical model, which necessitates the derivation of the Hamilton operators and the solution of the Schroedinger equation, will require the development of new theoretical methods, computational algorithms, and the application of high-performance supercomputers.

4. Conclusions

In the present work, a computer modeling of one of the important technological processes applied at the design of new semiconductor materials with given electrophysical properties—the process of the implantation of dopants into the base silicon substrate with a non-planar surface has been carried out.

The influence of process parameters (the aiming angle and implantation energy) on the distributions of concentrations of the admixtures of phosphorus, boron, and arsenic in silicon has been investigated.

5. References

[1] G. A. Tarnavsky and V. S. Anishchik, "Solvers of a Processor System of Program Complex NanoMod," *Nano- and Microsystem Technology*, in Russian, No. 4, 2009, pp. 6-13.

[2] G. A. Tarnavsky and V. S. Anishchik, "Toolbox NanoMod for Computer Support of the Design of Nano-Structured Semiconductor Materials," *Computational Methods and Programming*, in Russian, Vol. 10, Section 2, 2009, pp. 34-50.

[3] H. Runge, "Distribution of Implanted Ions under Arbitrarily Shaped Mask," *Physical Status Solidi*, Vol. 39(a), 1977, pp. 595-607.

[4] S. Furikawa, H. Matsumura and H. Ishiwara, "Theoretical Consideration on Lateral Spread of Implanted Ions," *Japanese Journal of Applied Physics*, Vol. 11, No. 2, 1972, pp. 134-142.

[5] S. Monfray, T. Skotnicki, B. Tavel, *et al*., "Highly-Performant 38 nm SON (Silicon-On-Nothing) P-MOSFETs with 9 nm-Thick Channels," *IEEE Silicon-on-Insulator Conference Proceedings*, 2002, pp. 22-25.

[6] D. Yu. Adamov and O. S. Matveenko, "Improvement of Structures of MOP Transistors in Nanometer Technologies," *Nano- and Micro-system Technology*, in Russian, No. 2, 2008, pp. 53-63.

[7] Ar. G. Mustafaev and Ab. G. Mustafaev, "Problems of Scaling the Gate Dielectric for MOS Technologies," *Nano- and Micro-System Technology*, in Russian, No. 4, 2008, pp. 7-22.

Energy and Power Engineering, **2010, 2, 78-89**
doi:10.4236/epe.2010.22012 Published Online May 2010 (http://www.SciRP.org/journal/epe)

Analysis and Design of Derivative Free Filters against Derivative Based Filter on the Simulated Model of a Three Phase Induction Motor

Ravikumar Jagadeesan[1]*, Subramanian Srikrishna[1], Prakash Jagadeesan[2]
[1]*Department of Electrical Engineering, Annamalai University, Annamalainagar, India*
[2]*Department of Instrumentation Engineering, Madras Institute of Technology, Anna University, Chennai, India*
E-mail: *sriram*1505*@gmail.com*
Received December 4, 2009; *revised January* 16, 2010; *accepted February* 20, 2010

Abstract

Recursive state estimation methods have aroused substantial attraction among many researchers and in particular, the drives research fraternity has shown increased interest in recent years. State estimators that surrogate direct measurements play an integral part in the operation of modern a.c. drives. Their robustness and accuracy are very much decisive for the performance of the drive. In this paper, a comparative analysis of the three nonlinear filtering schemes to estimate the states of a three phase induction motor on the simulated model is presented. The efficacy of Ensemble Kalman Filter (EnKF) against the traditional Jacobian based Filter or Extended Kalman Filter (EKF) and almost forbidden, hitherto least-attempted Unscented Kalman Filter (UKF) is very much exemplified. Theoretical aspects and comparative simulation results are investigated comprehensively with respect to three different scenarios viz., step changes in load torque, speed reversal, and low speed operation. Also, "Monte Carlo Simulation" runs have been exploited very extensively to show the superior practical usefulness of EnKF, by which the minimum mean square error (MMSE), which is often used as the performance index, ostensibly gets mitigated very radically by the proposed approach. The results throw light on alleviating the intrinsic intricacies encountered in EKF in parlance with the observer theory.

Keywords: Ensemble Kalman Filter [EnKF], Extended Kalman Filter [EKF], Three Phase Induction Motor [IM], State Estimation,Unscented Kalman Filter [UKF]

1. Introduction

Nonlinear system design using observers is incredibly a very rich area and has been well-researched over the past five decades by the researchers of induction motor control. In general an estimator is defined as a dynamic system, whose state variables are estimates of some other system (e.g., electrical machine) [1].

A plethora of nonlinear state estimation tools are available in the literature and among those a number of workers in the observer design for state and parameter estimation of IM attempted by augmenting the state with unknown parameters, were extensively based on the conceptually simple and celebrated Extended Kalman Filter (EKF), which is very well-known as a recursive nonlinear state estimator, derived by the direct linearization of state transition function and measurement equation for extending the (linear) Kalman filter in to the nonlinear filtering area [2-13].

Whilst, the well-established EKF which has been distinguished to be the best for processing noisy discrete measurements and for attaining high accuracy state estimates of nonlinear dynamic system in most of the situations, it suffers from the following serious shortcomings [14].

- Costly calculation of Jacobian matrices which are trivial in most applications and often results in implementation difficulties.
- It requires linearization of state transition and measurement functions at each and every sampling instant and first order linearization introduces huge errors in mean and covariance of the state vector, thus leading

to biasedness of its estimate.

- Lack of unwieldy analytical methods for appropriate selection of model covariances.

More recently, derivative free nonlinear state estimation tools such as Unscented Kalman filter [UKF] with deterministic sampling and Ensemble Kalman Filter [EnKF] which utilizes stochastic sampling approach, have been proposed to address the well-recognized demerits of the most popular EKF. These relatively new nonlinear filtering strategies do not involve any linearization that is required by the well-known EKF, thus yielding enhanced state estimates and have been shown to be a viable alternative to EKF in a wide diversity of applications.

Unscented Kalman Filter [UKF] introduced by Julier and Uhlmann [15], can capture the posterior mean and covariance precisely to third-order for any nonlinearity. UKF, inarguably a novel state estimator, has received very little attention among the researchers in the drives research group. Owing to its numerous advantages possessed by UKF, which were even though exploited very well in the field of chemical engineering, the major flaws posed by the model-dependency deprived of it from the applications in state and parameter estimation as applied to induction motor drives. Results exhibit that the UKF consistently outperforms the EKF in terms of state prediction and estimation errors [16].

The studies make use of UKF for state observation, in which simulation results obviously depict that several inherent properties of UKF recommending its use over EKF in nonlinear filtering problems [17]. Ironically, the characteristics of a new evolutional algorithm Square Root Unscented Kalman Filter [SRUKF], proposed by Rudolph Van Der Merwe and Eric. A. Wan [18], have been very well explored against the EKF by Jie Li *et al.* [19], and the comparitive results indicate that SRUKF does not display its properties and rather it increases the complexity of the method and so the computational cost. This has led to a conclusion that EKF is still the more realistic state estimation algorithm of induction motor drives.

A radical step in the filtering of nonlinear systems was the development of the Ensemble Kalman Filter [EnKF]. EnKF, a derivative free filter, proposed by Evenson, and which employs a stochastic sampling approach, can be used for handling the state estimation problems connected with systems involving discontinuities. Sample points straddle the discontinuity by which they are approximated. EnKF approximates multi-dimensional integration involved in propagation and update steps using Monte-Carlo sampling. Computation steps are very similar to UKF. It is a new class of particle filter and reasonable estimates can be obtained even by the use of 50 to 100 ensemble sizes. The merits of EnKF are listed as below [20].

- The model need not be smooth and differentiable.
- The state noise can be placed anywhere, for example on uncertain parameters and the noise distribution pattern can either be non-additive or non-Gaussian.

Since linearization is not involved in the calculation of state prediction and covariance in EnKF, the Kalman gain estimates are very much exact. This accurate gain at the end leads to improved estimates. Evenson [20], provides a thorough assessment of the theoretical formulation and practical implementation of the EnKF. Also an excellent review of the theoretical properties and applications of EnKF were also asserted by Gerrit Burgers *et al.* [21].

Drawing inspiration from the encouraging results of EnKF in the fields of chemical engineering [22], weather forecasting etc., [20,21], the behaviour of the EnKF algorithm is explored on the simulated model of a three phase induction motor, which is the main contribution of this paper. It is to be understood that no detailed investigations on EnKF to estimate the states of a three phase induction motor were realized. The EnKF algorithm is designed, analyzed, implemented and its effectiveness is evaluated with EKF and UKF under three different circumstances viz., step changes in load torque, speed reversal and low speed operation. Computer simulations have been carried out in the presence of additive state and measurement uncertainties to substantiate the test results of EnKF.

The organisation of the paper is as follows: After the introduction in Section 1, Section 2 discusses in detail the formulation of EnKF algorithm for state estimation of a three phase IM. Simulation studies are reported in Section 3 and the main concluding remarks drawn from the analysis of the simulation results are discussed in Section 4. EKF and UKF algorithms are provided in Appendices A and B respectively.

2. State Estimation

Consider a nonlinear system represented by the following nonlinear differential equations:

$$\frac{dx}{dt} = F\left[x(t), u(t)\right] \tag{1}$$

$$y = G\left[x(t), u(t)\right] \tag{2}$$

Equation (1) is a state equation and Equation (2) describes the relation between state and measurement variables. In order to describe a discrete nonlinear system, Equations (1) and (2) can be functionally represented in discrete forms as:

$$x(k) = f\left[x(k-1), u(k-1)\right] + w(k) \tag{3}$$

$$y(k) = g\left[x(k-1), u(k-1)\right] + v(k) \tag{4}$$

where $x(k) \in R^n$ is the system state vector, $u(k) \in R^m$ is the known system input, $w(k) \in R^p$ is the state noise, $y(k) \in R^r$ is the measured variable and $v(k) \in R^r$ is the measurement noise .The parameter k represents the sampling instant and the symbol f is a (possibly nonlinear) state transition function and g is a (possibly nonlinear) measurement function.

The objective of the recursive Bayesian state estimation problem is to find the mean and variance of a random variable $x(k)$ using the conditional probability density function $p\left[\mathbf{x}(k)|\mathbf{Y}^{(k)}\right]$. $\mathbf{Y}^{(k)}$ denotes the set of all the available measurements, *i.e.* $Y^k \triangleq \{y(k), y(k-1),.....\}$ As reported by Arulampalam *et al.* [23], the posterior density $p\left[\mathbf{x}(k) \mid \mathbf{Y}^k\right]$ is estimated in two steps: (a) prediction step, which is computed before obtaining an observation, and, (b) update step, which is computed after obtaining an observation. In the prediction step, the posterior density $p\left[\mathbf{x}(k-1) \mid \mathbf{Y}^{k-1}\right]$ at the previous time step is propagated into the next time step through the transition density $\{ p\left[\mathbf{x}(k) \mid \mathbf{x}(k-1)\right] \}$ as follows:

$$p\left[\mathbf{x}(k) \mid \mathbf{Y}^{k-1}\right] = \int p\left[\mathbf{x}(k) \mid \mathbf{x}(k-1)\right] p\left[\mathbf{x}(k-1) \mid \mathbf{Y}^{k-1}\right] d\mathbf{x}(k-1) \tag{5}$$

The update stage involves the application of Bayes' rule:

$$p\left[\mathbf{x}(k) \mid \mathbf{Y}^k\right] = \frac{p\left[\mathbf{y}(k) \mid \mathbf{x}(k)\right]}{p\left[\mathbf{y}(k) \mid \mathbf{Y}^{k-1}\right]} \times p\left[\mathbf{x}(k) \mid \mathbf{Y}^{k-1}\right] \tag{6}$$

where,

$$p\left[\mathbf{y}(k) \mid \mathbf{Y}^{k-1}\right] = \int p\left[y(k) \mid x(k)\right] p\left[\mathbf{x}(k) \mid \mathbf{Y}^{k-1}\right] d\mathbf{x}(k) \tag{7}$$

Combining (5), (6) and (7)

$$p\left[\mathbf{x}(k) \mid \mathbf{Y}^k\right] = \frac{p\left[\mathbf{y}(k) \mid \mathbf{x}(k)\right] \left[\int p\left[\mathbf{x}(k) \mid \mathbf{x}(k-1)\right] p\left[\mathbf{x}(k-1) \mid \mathbf{Y}^{k-1}\right] d\mathbf{x}(k-1)\right]}{\int p\left[y(k) \mid x(k)\right] p\left[\mathbf{x}(k) \mid \mathbf{Y}^{k-1}\right] d\mathbf{x}(k)} \tag{8}$$

Equation (8) describes how the conditional posterior density function propagates from $p\left[\mathbf{x}(k-1) \mid \mathbf{Y}^{k-1}\right]$ to $p\left[\mathbf{x}(k) \mid \mathbf{Y}^k\right]$. The properties of the state transition Equation (3) are accounted through the transition density function $p\left[\mathbf{x}(k) \mid \mathbf{x}(k-1)\right]$ while $p\left[\mathbf{y}(k) \mid \mathbf{x}(k)\right]$ reflects the nonlinear measurement function. The prediction and update strategy provide an optimal solution to the state estimation, which, unfortunately, involves high-dimensional integration. The exact analytical solution to the recursive propagation of the posterior density is very difficult to obtain. But, solutions do exist in certain cases [25]. While dealing with nonlinear systems, it becomes necessary to develop approximate and computationally tractable sub-optimal solutions to the above sequential Bayesian estimation problem.

2.1. Unconstrained State Estimation Using Ensemble Kalman Filter

In this section we describe the most general form of the EnKF as available in the literature (Gillijns *et al.* [24], Prakash *et al.* [25]). The EnKF is initialized by drawing N particles $\{\mathbf{x}^{(i)}(0 \mid 0)\}$ from a given distribution. At each time step, N samples $\{\mathbf{w}^{(i)}(k-1), \mathbf{v}^{(i)}(k) : i = 1,..N\}$ for $\{ \mathbf{w}(k) \}$ and $\{ \mathbf{v}(k) \}$ are drawn randomly using the distributions of state noise and measurement noise. These sample points together with particles $\{\hat{\mathbf{x}}^{(i)}(k-1 \mid k-1) : i = 1,..N\}$ are then propagated through the system dynamics to compute a cloud of transformed sample points (particles) as follows:

$$\hat{\mathbf{x}}^{(i)}(k \mid k-1) = \hat{\mathbf{x}}^{(i)}(k-1 \mid k-1) + \left[\int_{(k-1)T}^{kT} F\left[\mathbf{x}(\tau), \mathbf{u}(k-1)\right] d\tau \right] + \mathbf{w}^{(i)}(k) : \; i = 1, 2, ...N \tag{9}$$

These particles are then used to estimate the sample mean and covariance as follows:

$$\bar{\mathbf{x}}(k \mid k-1) = \frac{1}{N} \sum_{i=1}^{N} \hat{\mathbf{x}}^{(i)}(k \mid k-1) \tag{10}$$

$$\bar{\mathbf{y}}(k \mid k-1) = \frac{1}{N} \sum_{i=1}^{N} H\left[\hat{\mathbf{x}}^{(i)}(k \mid k-1)\right] + \mathbf{v}^{(i)}(k) \tag{11}$$

$$P_{\varepsilon,\mathbf{e}}(k) = \frac{1}{N-1} \sum_{i=1}^{N} \left[\boldsymbol{\varepsilon}^{(i)}(k)\right] \left[\mathbf{e}^{(i)}(k)\right]^T \tag{12}$$

$$P_{\mathbf{e},\mathbf{e}}(k) = \frac{1}{N-1} \sum_{i=1}^{N} \left[\mathbf{e}^{(i)}(k)\right] \left[\mathbf{e}^{(i)}(k)\right]^T \tag{13}$$

where,

$$\boldsymbol{\varepsilon}^{(i)}(k) = \hat{\mathbf{x}}^{(i)}(k \mid k-1) - \overline{\mathbf{x}}(k \mid k-1) \quad (14)$$

$$\mathbf{e}^{(i)}(k) = H\left[\hat{\mathbf{x}}^{(i)}(k \mid k-1)\right] + \mathbf{v}^{(i)}(k) - \overline{\mathbf{y}}(k \mid k-1) \quad (15)$$

The Kalman gain and samples of updated particles are then computed as follows:

$$K(k) = P_{\boldsymbol{\varepsilon},\mathbf{e}}(k)\left[P_{\mathbf{e},\mathbf{e}}(k)\right]^{-1} \quad (16)$$

$$\Upsilon^{(i)}(k \mid k-1) = \left\{\mathbf{y}(k) - H\left[\hat{\mathbf{x}}^{(i)}(k \mid k-1)\right] + \mathbf{v}^{(i)}(k)\right\} \quad (17)$$

$$\hat{\mathbf{x}}^{(i)}(k \mid k) = \hat{\mathbf{x}}^{(i)}(k \mid k-1) + K\ (k)\Upsilon^{(i)}(k \mid k-1) \quad (18)$$

$$\Upsilon^{(i)}(k \mid k) = \left\{\mathbf{y}(k) - H\left[\hat{\mathbf{x}}^{(i)}(k \mid k)\right] + \mathbf{v}^{(i)}(k)\right\} \quad (19)$$

where i=1,2,…N. The updated state estimate is computed as the mean of the updated cloud of particles, *i.e*.

$$\hat{\mathbf{x}}(k \mid k) = \frac{1}{N}\sum_{i=1}^{N}\hat{\mathbf{x}}^{(i)}(k \mid k) \quad (20)$$

The covariance of the updated estimates can be computed as

$$\mathbf{P}(k \mid k) = \frac{1}{N-1}\sum_{i=1}^{N}\left[\boldsymbol{\gamma}^{(i)}(k)\right]\left[\boldsymbol{\gamma}^{(i)}(k)\right]^{T} \quad (21)$$

$$\boldsymbol{\gamma}^{(i)}(k) = \hat{\mathbf{x}}^{(i)}(k \mid k) - \hat{\mathbf{x}}(k \mid k) \quad (22)$$

While $\mathbf{P}(k \mid k)$ is not required in subsequent computations of the EnKF, it can serve as a measure of the uncertainty associated with the updated estimates. It may be noted that in Equation (15), the predicted observations have been perturbed by drawing samples from the measurement noise distribution. The random perturbations have to be carried out so that the updated sample covariance matrix of the ensemble Kalman filter matches with that of the updated error covariance matrix of the Kalman filter [20]. This step helps in creating a new ensemble of states having correct error statistics for the update step [24]. It may be noted that the accuracy of the estimates depends on the number of data points (N). Prakash *et al*. [25] have indicated that the ensemble size between 50 and 100 suffices even for large dimensional systems.

3. Induction Motor Model

In order to apply nonlinear filters for the state estimation of a three phase IM, the first step in the estimation process is the precise definition of a mathematical model, which appropriately represents the real behaviour of a motor. The most preferred way of capturing the dynamics of an induction motor is by a fifth-order differential equation with two inputs ($v_{s\alpha}$, $v_{s\beta}$) and five state variables($i_{s\alpha}$, $i_{s\beta}$, $\Psi_{r\alpha}$, $\Psi_{r\beta}$, w_m) are available for measurement. One of the model structures used by Murat Burat *et al.* [2], its associated parameters (see **Table 1**) and noise covariance matrices have been used to generate the true value of the state variables.

The IM is modelled by the following differential equations in the frame of references connected to the stator [2]:

$$\frac{di_{s\alpha}}{dt} = \dot{X}_1 = -\left[\frac{R_s}{L_\sigma} + \frac{R_r' L_m^2}{L_r'^2 L_\sigma}\right] i_{s\alpha} + \frac{R_r' L_m}{L_r'^2 L_\sigma}\psi_{r\alpha} + \frac{L_m}{L_\sigma L_r'} P_p \omega_m \psi_{r\beta} + \frac{1}{L_\sigma} V_{s\alpha} \quad (23)$$

$$\frac{di_{s\beta}}{dt} = \dot{X}_2 = -\left[\frac{R_s}{L_\sigma} + \frac{R_r' L_m^2}{L_r'^2 L_\sigma}\right] i_{s\beta} + \frac{R_r' L_m}{L_r'^2 L_\sigma}\psi_{r\beta} - \frac{L_m}{L_\sigma L_r'} P_p \omega_m \psi_{r\alpha} + \frac{1}{L_\sigma} V_{s\beta} \quad (24)$$

$$\frac{d\psi_{r\alpha}}{dt} = \dot{X}_3 = \frac{R_r'}{L_r'} L_m i_{s\alpha} - \frac{R_r'}{L_r'}\psi_{r\alpha} - P_p \omega_m \psi_{r\beta} \quad (25)$$

$$\frac{d\psi_{r\beta}}{dt} = \dot{X}_4 = \frac{R_r'}{L_r'} L_m i_{s\beta} - \frac{R_r'}{L_r'}\psi_{r\beta} + P_p \omega_m \psi_{r\alpha} \quad (26)$$

$$\frac{d\omega_m}{dt} = \dot{X}_5 = -\frac{3}{2}\frac{P_p}{J_L}\frac{L_m}{L_r'}\psi_{r\beta} i_{s\alpha} + \frac{3}{2}\frac{P_p}{J_L}\frac{L_m}{L_r'}\psi_{r\alpha} i_{s\beta} - \frac{1}{J_L} t_L \quad (27)$$

The measurement equation is given by:

$$Y = [i_{s\alpha} \quad i_{s\beta}]^T \quad (28)$$

The value of state variables were initialized as below:

$$X(0 \mid 0) = [0;0;0;0;0]$$

The evolution of true state variables is computed by solving the nonlinear differential equations, using the differential equation solver in MATLAB 7.7. The sampling time is chosen to be as 0.01 and the length of all the simulation trials as 2000, besides, the state and measurement noises are added in an additive fashion.

3.1. Design of Derivative Based and Derivative Free Filters

The algorithm reported in Section 2 and in the appendices A and B respectively, have been used to estimate the state variables of the IM, which takes into account of load torque as an additional state variable. In order to generate unbiased state estimates, in all the three nonlinear estimators taken for comparative analysis, it has been assumed that in the presence of load torque variation,

Table 1. Rated values and parameters of the IM used for simulation study.

P (KW)	f (Hz)	J_L (Kg.m^2)	P_p	V (V)	I (A)	R_s (Ω)	R_r (Ω)	L_s (H)	L_r (H)	L_m (H)	N_m (rpm)	T_L (Nm)
3	50	0.05	2	380	6.9	2.283	2.133	0.23	0.23	0.22	1430	20

the state equation is augmented with the differential equation which is of the form:

$$\frac{dt_L}{dt} = \dot{X}_6 = 0 \tag{29}$$

Equation (29) implies that the load torque can vary only in a step-like fashion. The afore-said equation, together with the differential Equations (23) to (27), listed in the preceding sub-section have been used for generating one step ahead predicted state estimates. The state and measurement noise covariance matrices (see **Table 2**) were initialized as specified in [2]. However the variance linked with the augmented state variable is changed, to attain good responses.

It is to be noted from **Table 2** that for EKF and EnKF, identical values of state and measurement noises have been realized. In the lime-light of UKF's supremacy over EKF and since the results produced by the UKF with the alike value of noise covariances, are somewhat not acceptable, the variance associated with the augmented state variable, is further fine tuned to get a fair estimate, and despite our several endeavours, the expected better results were not evolved. It is worth noting that manual tuning of the UKF using trial and error method is simple to carry, but the process is time consuming, and acceptable performance can only be acquired with a great effort from an experienced operator.

It has been assumed that the random errors were present in the noise covariance matrices and the estimation is started with the initial value as shown below:

$$X(0|0) = [0; 0; 0; 0; 0]$$

The initial error covariance matrices reported in [2] have been fixed and are as follows:

Table 2. Initial value of measurement and state noise covariance matrices.

State estimation schemes	State Noise Covariance matrix	Measurement Covariance matrix
EKF and ENKF	$Q_{EKF,\ ENKF}$ = diag {1.5×10^{-11}A^2 1.5×10^{-11}A^2 10^{-15}(V-s)^2 10^{-15}(V-s)^2 10^{-15}(V-s)^2 10^{-15}(rad/s)^2 10^{-6}(N-m)^{2*}}	$R_{EKF} = R_{UKF} = R_{ENKF}$ = diag{$1.5e^{-7}$A^2 $1.5e^{-7}$A^2}
UKF	Q_{UKF} = diag {$Q_{EKF\ and\ ENKF}$; $10^{-8+9/2*}$ (N-m)^2}*	

* Variance connected with the augmented state variable.

P= diag{ 1A^2 1A^2 1(V-s)^2 1(V-s)^2 1(rad-s)^2 1 (N-m)^2}

EKF tuning is performed in an ad-hoc style, but the EnKF algorithm differs substantially from the customary approach in the sense that, when the particle size is very small, the EnKF may not always converge or arrive at an optimal solution, and in order to get reasonable responses, the ensemble size must be more, and in our instance, the ensemble size for a single simulation trial, for all the situations tested in our study is chosen as 200. It should be noted that the EnKF algorithm is computationally intensive. The computation time per sampling instant, for a single simulation run with a particle size of 200, is about 45 minutes on an Intel Core 2 Duo PC.

4. Simulation Results and Discussion

4.1. Test Results

Computer simulations were performed to test the usefulness of the EnKF algorithm against other state prediction and estimation methods such as EKF and UKF. The simulations were carried out in MATLAB7.7-R2008(b) program on an Intel core 2 Duo Processor with 1.8GHz CPU and 2 GB RAM. Three different scenarios reported by Murat Burat *et al.* [2], have been used for the comparative analysis.

4.1.1. Scenario-I: Step Changes in Load Torque

The evolution of true and estimated state variables in the presence of step changes in load torque is shown in **Figure 1**. It is being observed that the estimated values of state variables and the filtered estimate of measured variables track their true value more closely throughout the operating range. The analysis of **Figure 1** enables us to conclude that relatively good estimates are obtained from EnKF in comparision with the EKF and UKF. Moreover the estimate of the augmented state variable is determined to be very accurate.

4.1.2. Scenario-II: Reversal of Speed

Figure 2 presents the emergence of true and estimated state variables for the speed reversal case and this is accomplished by changing the input frequency from +50 Hz to –50Hz. It is being inferred that the state estimates obtained by EnKF are very accurate, compared to the behaviour of the estimates produced by using the EKF and UKF formulations. It is noteworthy that all the three state estimation schemes taken for comparative study perform exceedingly well in this case.

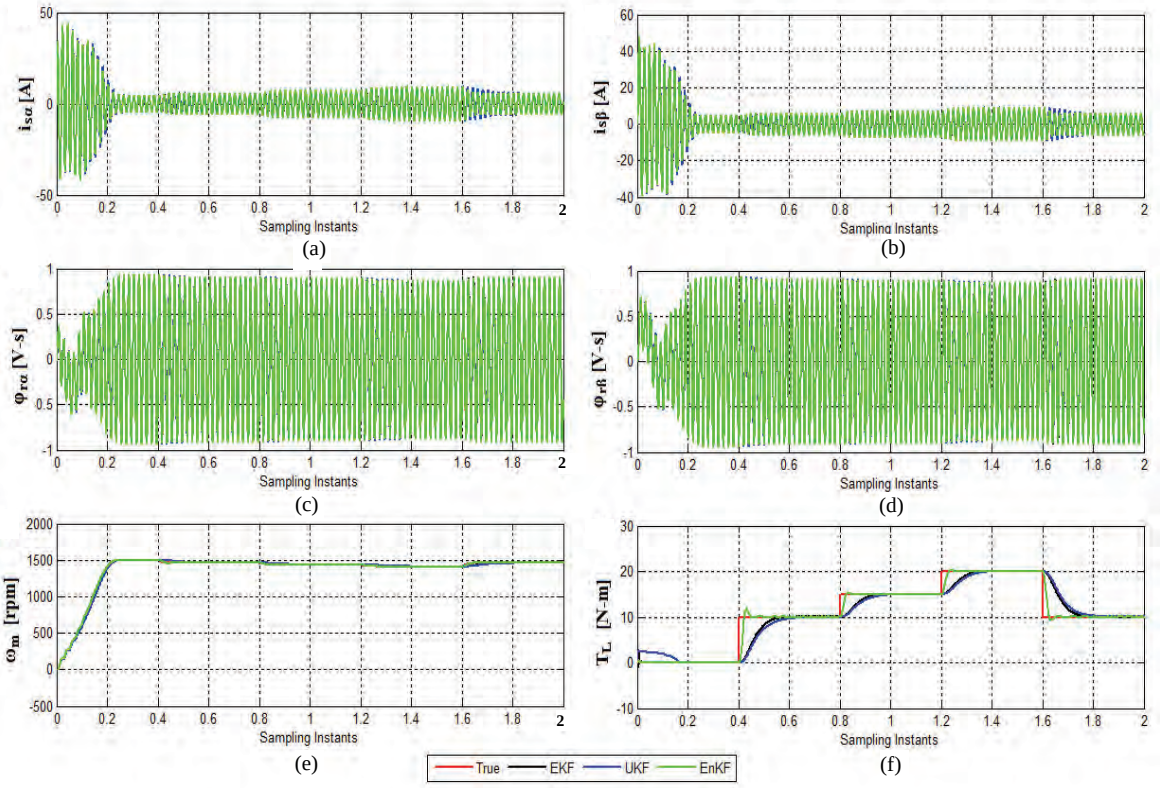

Figure 1. Evolution of true and estimated state variables for step changes in load torque.

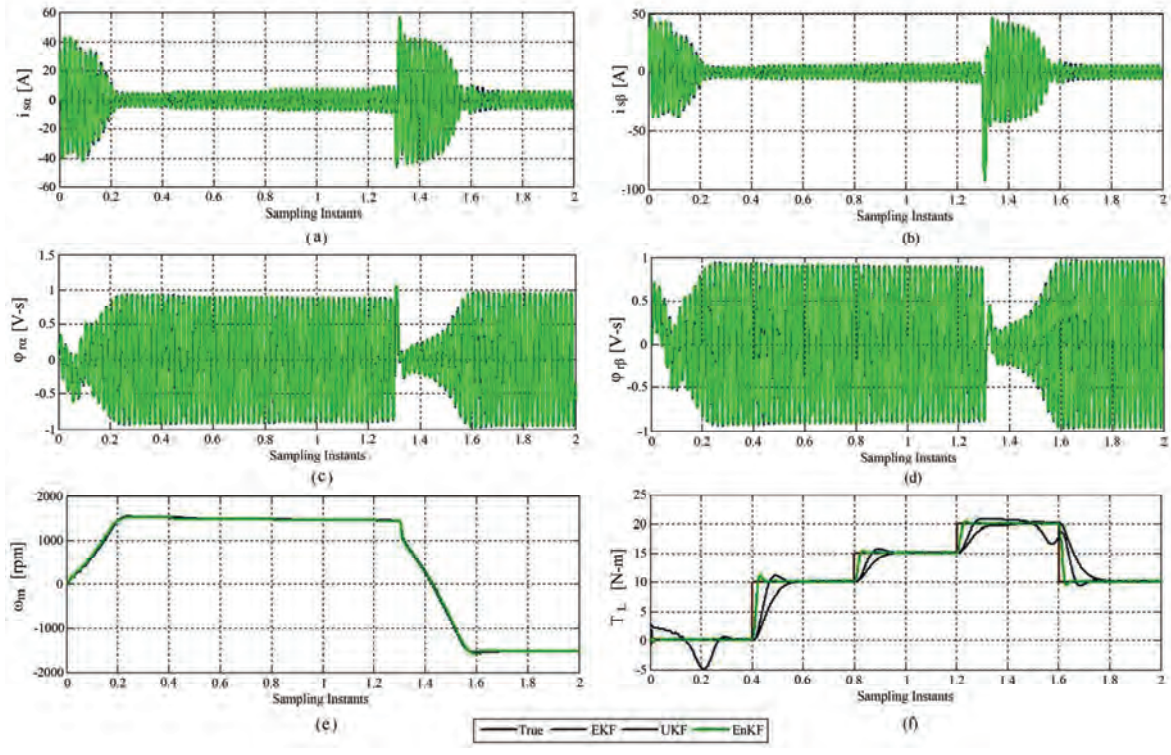

Figure 2. Emergence of true and estimated state variables for speed reversal.

4.1.3. Scenario-III: Low Speed Operation

One significant aspect being very well examined in the literature is the low speed operation, which was presumed as a serious challenge in the arena of IM drives. This is possible by constantly maintaining v/f ratio and the low speed operation results are very well displayed in **Figure 3**. A closer examination of the **Figure 3** discloses that the estimates of speed and rotor fluxes are found to be more precise. It should be noted that the Kalman filter and its variants have demonstrated an acceptable performance in the low speed operation. Regardless of its appreciable results of simulation at low speeds for EKF algorithm, the complexity, computational burden and accuracy issues practically outlaw the choice of EKF algorithm over a low-cost fixed processor.

a) $i_{s\alpha}$[A]-Stator stationary axis components of stator currents. b) $i_{s\beta}$[A]-Stator stationary axis components of stator currents. c) $\psi_{r\alpha}$[V-s]-Rotor stationary axis components of stator flux. d) $\psi_{r\beta}$[V-s]-Rotor stationary axis components of stator flux. e) ω_m[rad-s]-Angular velocity. f) T_L[N-m]-Load torque.

4.2. Performance Assessment

The performance of the three nonlinear estimators taken for comparative study must be assessed through simulation, because stochastic systems are involved in these studies. For each case that is being analyzed, a simulation run that consists of N_T (trials) with the length of each simulation trial being equal to L is conducted. In all the simulation trials, the sum of the squares of the estimation errors, which is truly the difference between the estimated value of the state variables and the true value of the state variables, that have been obtained. The mean of the estimation errors based on 25 Monte Carlo simulations for the EKF, UKF and ENKF are reported in **Tables 4, 5** and **6** respectively. A close view at the tables makes one to conclude that, the Minimum Mean Square Error [MMSE], which is often used as a performance index is found to be very low for EnKF in all the three different scenarios taken for comparative simulation study. It is apparent from the **Table 6** that, MMSE gets lessened by the use of more ensemble sizes. The computational time per sampling instant for an ensemble size of 25 for EnKF is compared with the EKF and UKF and presented in the form of histogram (see **Figure 4**). Despite the fact that the time-complexity is said to be large, these are well within the capabilities of contemporary signal processing devices, so that a real-time accomplishment is plausible.

5. Concluding Remarks

An attempt has been made in this paper to use the EnKF for the estimation of states of a three phase IM. Computer simulations have been performed meticulously to

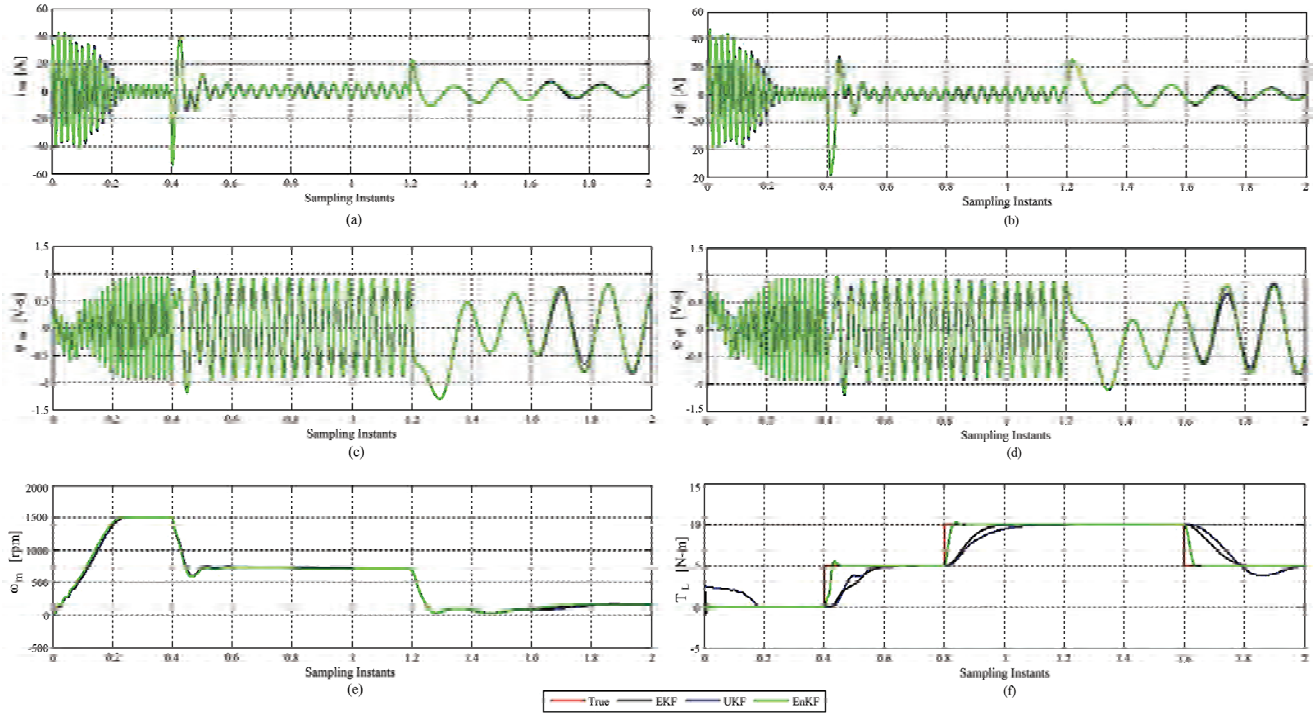

Figure 3. Emergence of true and estimated state variables for low speed operation.

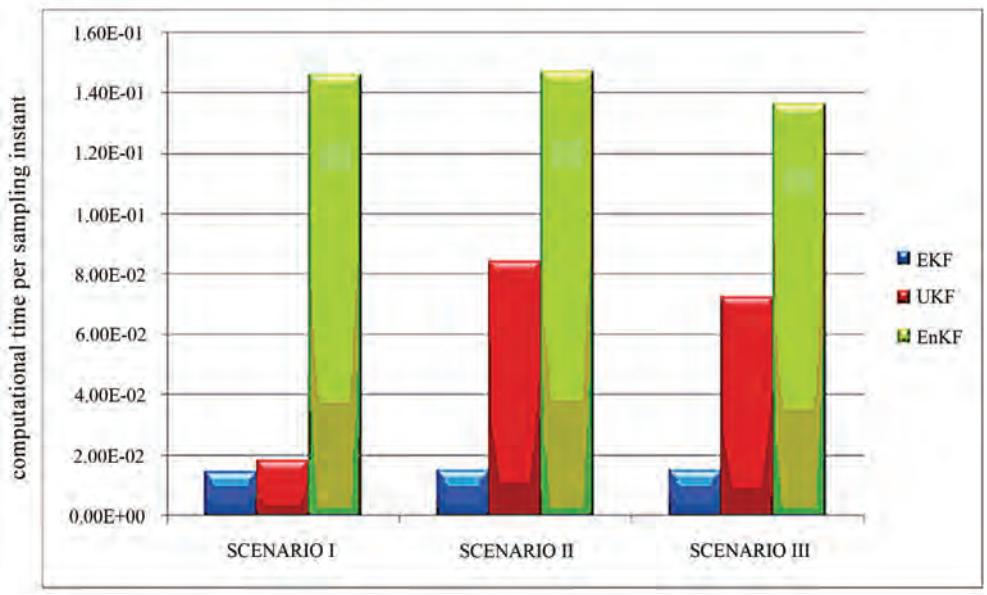

Figure 4. Comparision of execution time of EnKF for a particle size 25 against EKF and UKF.

Table 4. Minimum mean square error (MMSE) values of EKF.

STATE VARI-ABLES	SCENARIO – I	SCENARIO – II	SCENARIO – III
	MEAN	MEAN	MEAN
$i_{s\alpha}$	$6.9100e^{-2}$	$6.6720e^{-2}$	$1.8400e^{-2}$
$i_{s\beta}$	$6.9093e^{-2}$	$6.6723e^{-2}$	$1.8469e^{-2}$
$\psi_{r\alpha}$	$6.0288e^{-5}$	$5.8286e^{-5}$	$1.1682e^{-4}$
$\psi_{r\beta}$	$6.0290e^{-5}$	$5.8282e^{-5}$	$1.3016e^{-4}$
ω_m	$9.4296e^{-1}$	$9.7334e^{-1}$	$4.8508e^{-1}$
t_L	$5.5802e^{0}$	$5.5872e^{0}$	$2.0452e^{0}$

Table 5. Minimum mean square error (MMSE) values of UKF.

STATE VARI-ABLES	SCENARIO – I	SCENARIO – II	SCENARIO – III
	MEAN	MEAN	MEAN
$i_{s\alpha}$	$1.8604e^{-1}$	$2.6480e^{-1}$	$3.1616e^{-1}$
$i_{s\beta}$	$1.8611e^{-1}$	$2.6479e^{-1}$	$3.0686e^{-1}$
$\psi_{r\alpha}$	$1.0164e^{-4}$	$1.4123e^{-4}$	$1.8700e^{-3}$
$\psi_{r\beta}$	$1.0357e^{-4}$	$1.4314e^{-4}$	$2.2864e^{-3}$
ω_m	$1.1745e^{0}$	$2.1488e^{0}$	$2.3092e^{0}$
t_L	$4.6709e^{0}$	$4.7167e^{0}$	$2.6369e^{0}$

compare the behaviour of EnKF against the EKF and UKF. The main conclusion drawn from this work, is that the inherent flaw of the well-appreciated EKF *i.e.*, the exhaustive Jacobian computation, which is very well the cause of biasedness of its estimate and imposing severe computational cost in real-time implementation were overcome, thanks to the action of EnKF, which provides a derivative free approach for estimation of predicted covariances required in the update step. As evidenced by the results, the EnKF algorithm surpasses EKF and UKF in all the scenarios tested, and a noticeable enhancement in its performance is attained even by the use of 50 to 100 ensemble sizes. This can be claimed as a potential advantage over EKF.

Enlightened by the belief that UKF is a superior alternative of the EKF, though theoretically proven, it is fine tuned to obtain an estimate very nearer to EKF, but even then UKF did not exhibit its properties, and the results achieved are said to be implausible. Additive and Gaussian noise distribution sequence is usually made as an assumption in the state estimation of a three phase IM. However, there are schools of thought supporting the distribution of noise in IM drive system in real-time, as being primarily non-addditive and non-Gaussian in nature. Categorically, the drives research community has been left bewildered by such an apparent dissension and even under such circumstances, the EnKF algorithm will work satisfactorily, which has to be further explored carefully. Conversely, the well-acclaimed EKF can be strictly applied only for restricted class of noise distribution patterns. Because of its conspicuous performance, the EnKF algorithm has an edge over EKF in a wide diversity of applications. The only drawback is the time-complexity, but nevertheless a processor with high

Table 6. Minimum mean square Error (MMSE) values of EnKF for different ensemble sizes.

PARTICLE SIZE	STATE VARIABLES	SCENARIO I	SCENARIO II	SCENARIO III
25	$i_{s\alpha}$	$7.2293e^{-4}$	$5.5775e^{-4}$	$1.1594e^{-4}$
	$i_{s\beta}$	$7.2395e^{-4}$	$5.5142e^{-4}$	$1.8477e^{-4}$
	$\psi_{r\alpha}$	$2.3036e^{-5}$	$2.7246e^{-5}$	$2.7319e^{-5}$
	$\psi_{r\beta}$	$1.9797e^{-5}$	$2.0483e^{-5}$	$2.0248e^{-5}$
	ω_m	$3.2161e^{-2}$	$2.5811e^{-2}$	$1.9117e^{-2}$
	t_L	$1.4886e^{0}$	$1.3837e^{0}$	$5.0224e^{-1}$
50	$i_{s\alpha}$	$5.3629e^{-4}$	$4.3726e^{-4}$	$8.0065e^{-5}$
	$i_{s\beta}$	$5.4094e^{-4}$	$4.3459e^{-4}$	$1.5401e^{-4}$
	$\psi_{r\alpha}$	$1.3467e^{-5}$	$1.7553e^{-5}$	$1.7393e^{-5}$
	$\psi_{r\beta}$	$9.0231e^{-6}$	$8.8537e^{-6}$	$8.6287e^{-6}$
	ω_m	$2.8156e^{-2}$	$2.3189e^{-2}$	$1.7070e^{-2}$
	t_L	$1.4234e^{0}$	$1.3300e^{0}$	$4.8683e^{-1}$
75	$i_{s\alpha}$	$4.5133e^{-4}$	$3.8873e^{-4}$	$7.7783e^{-5}$
	$i_{s\beta}$	$4.5348e^{-4}$	$3.8735e^{-4}$	$1.4255e^{-4}$
	$\psi_{r\alpha}$	$1.2643e^{-5}$	$1.7070e^{-5}$	$1.7924e^{-5}$
	$\psi_{r\beta}$	$7.7786e^{-6}$	$7.4994e^{-6}$	$7.2875e^{-6}$
	ω_m	$2.6420e^{-2}$	$2.2476e^{-2}$	$1.5958e^{-2}$
	t_L	$1.3917e^{0}$	$1.3212e^{0}$	$4.7789e^{-1}$
100	$i_{s\alpha}$	$4.5836e^{-4}$	$3.8299e^{-4}$	$7.0702e^{-5}$
	$i_{s\beta}$	$4.5023e^{-4}$	$3.8734e^{-4}$	$1.3433e^{-4}$
	$\psi_{r\alpha}$	$9.6340e^{-6}$	$1.3041e^{-5}$	$1.6903e^{-5}$
	$\psi_{r\beta}$	$6.5697e^{-6}$	$6.3207e^{-6}$	$6.1035e^{-6}$
	ω_m	$2.6116e^{-2}$	$2.1808e^{-2}$	$1.5007e^{-2}$
	t_L	$1.4050e^{0}$	$1.3219e^{0}$	$4.8265e^{-1}$
150	$i_{s\alpha}$	$4.2953e^{-4}$	$3.5544e^{-4}$	$6.8404e^{-5}$
	$i_{s\beta}$	$4.4175e^{-4}$	$3.6098e^{-4}$	$1.2849e^{-4}$
	$\psi_{r\alpha}$	$1.1029e^{-6}$	$1.5337e^{-5}$	$1.5158e^{-5}$
	$\psi_{r\beta}$	$2.4206e^{-6}$	$2.0697e^{-6}$	$1.8484e^{-6}$
	ω_m	$2.5491e^{-2}$	$2.2614e^{-2}$	$1.4785e^{-2}$
	t_L	$1.3995e^{0}$	$1.3059e^{0}$	$4.7555e^{-1}$

calculation performance can accomplish these require ments. Since the digitized a.c. drives have reached the state-of-the-art of technology, any order of these challenging crossroads can be proven to be mediocre.

6. References

[1] P. Vas, "Sensorless Vector and Direct Torque Control," Oxford University Press, New York, 1998.

[2] M. Burat, S. Bogosyan and M. Gokasan, "Speed Sensorless Estimation for Induction Motors Using Extended Kalman Filters," *IEEE Transactions on Industrial Electronics*, Vol. 54, No. 1, February 2007, pp. 272-280.

[3] M. Burat, S. Bogosyan and M. Gokasan, "Braided Extended Kalman Filters for Sensorless Estimation in Induction Motors at High-low/Zero Speed," *IET Control Theory & Applications*, Vol. 1, No. 4, 2007, pp. 987-998.

[4] M. Burat, S. Bogosyan and M. Gokasan, "Speed Sensorless Direct Torque Control of IMs with Rotor Resistance Estimation," *Energy Conversion and Management*, Vol. 46, No. 3, 2005, pp. 335-349.

[5] M. Burat, S. Bogosyan and M. Gokasan, "An EKF Based Estimator for Speed Sensorless Vector Control of Induction Motors," *Electric Power Components and Systems*, Vol. 33, No. 7, 2005, pp. 727-744.

[6] J. Holtz, "Sensorless Control of Induction Machines with or without Signal Injection?" *IEEE Transactions on Industrial Electronics*, Vol. 53, No. 1, February 2006, pp. 7-30.

[7] J. W. Finch, D. J. Atkinson and P. P. Acarnley, "Full-Order Estimator for Induction Motor States and Parameters," *IEE Electric Power Applications*, Vol. 145, No. 3, May 1998, pp. 169-179.

[8] C. Lascu, I. Boldea and F. Blaabjerg, "Comparitive Study of Adaptive and Inherently Sensorless Observers for Variable Speed Induction Motor Drives," *IEEE Transactions on Industrial Electronics*, Vol. 53, No. 1, February 2006, pp. 57-65.

[9] G. G. Soto, E. Mendes and A. Razek, "Reduced-Order Observers for Rotor Flux, Rotor Resistance and Speed Estimation for Vector Controlled Induction Motor Drive Using the Extended Kalman Filter Technique," *IEE Proceedings Electric Power Applications*, Vol. 146, No. 3, May 1999.

[10] H.-W. Kim and S.-K. Sul, "A New Motor Speed Estimator Using Kalman Filter in Low-Speed Range," *IEEE Transactions on Industrial Electronics*, Vol. 43, No. 4, August 1996, pp. 498-504.

[11] D. J. Atkinson, J. W. Finch and P. P. Acarnley, "Estimation of Rotor Resistance in Induction Motors," *IEE Proceedings Electric Power Applications*, Vol. 146, No. 3, January 1996.

[12] K. L. Shi, T. F. Chan, Y. K. Wong and S. L. Ho, "Speed Sensorless Control of an Induction Motor Drive Using an Optimized Extended Kalman Filter," *IEEE Transactions on Industrial Electronics*, Vol. 49, No. 1, February 2002, pp. 124-133.

[13] Y.-R. Kim, S.-K. Sul and M.-H. Park, "Speed Sensorless Vector Control of Induction Motor Using Extended Kalman Filter," *IEEE Transactions on Industrial Electronics*, Vol. 30, No. 5, September/October 1994, pp. 1225-1233.

[14] S. Julier, J. K. Uhlmann and H. F. Durrant-Whyte, "A New Method for the Nonlinear Transformation of Means and Covariances in Filters and Estimators," *IEEE Transactions on Automatic Control*, Vol. 45, No. 3, March 2000, pp. 477-482.

[15] S. J. Julier and J. K. Uhlmann, "Unscented Filtering and Nonlinear Estimation," *Proceedings of the IEEE*, Vol. 92, No. 3, March 2004, pp. 401-422.

[16] K. Xiong, H. Y. Zhang and C. W. Chan, "Performance Evaluation of UKF-Based Nonlinear Filtering," *Automatica*, Vol. 42, 2006, pp. 261-270.

[17] B. Akin, U. Orguner and A. Ersak, "State Estimation Using Unscented Kalman Filter," *Proceedings of IEEE*, 2003, pp. 915-919.

[18] R. van der Merwe and E. A. Wan, "The Square-Root Unscented Kalman Filter for State and Parameter Estimation," *Proceedings of the International Conference on Acoustics, Speech and Signal Processing*, May 2001.

[19] J. Lie, Y. R. Zhong and H. P. Ren, "Speed Estimation of Induction Machines Using Square Root Unscented Kalman Filter," *Proceedings of the IEEE*, 2005, pp. 674-679.

[20] G. Evensen, "Ensemble Kalman Filter: Theoretical Formulation and Practical Implementation," *Ocean Dynamics*, Vol. 53, 2003, pp. 343-367.

[21] G. Burgers, P. J. Van Leeuwen and G. Evenson, "Analysis Scheme in Ensemble Kalman Filter," *American Meteorological Society*, Vol. 126, 1998, pp. 1719-1724.

[22] J. Prakash, S. C. Patwardhan and S. L. Shah, "Constrained State Estimation Using the Ensemble Kalman Filter," *Proceedings of the American Control Conference*, 2008, pp. 3542-3547.

[23] M. S. Arulampalam, S. Maskell, N. Gordon and T. Clapp, "A Tutorial on Particle Filters for Online Nonlinear/Non-Gaussian Bayesian Tracking," *IEEE Transactions on Signal Processing*, Vol. 50, No. 2, 2002, pp. 174-188.

[24] S. Gillijns, O. B. Mendoza, J. Chandrasekar, B. L. R. De Moor, D. S. Bernstein and A. Ridley, "What is the Ensemble Kalman Filter and How Well does it Work?" *Proceedings of the American Control Conference*, 2006, pp. 4448-4453.

[25] S. C. Patwardhan, J. Prakash and S. L. Shah, "Soft Sensing and State Estimation: Review and Recent Trends," *Proceedings of IFAC Conference on Cost Effective Automation*, Mexico, Vol. 1, Part 1, 2008.

Nomenclature

P_p	No. of pole pairs
$L_\sigma = \sigma L_s$	Stator transient inductance (H)
σ	Leakage or Coupling factor
L_s	Stator inductance (H)
R_s	Stator resistance (Ω)
L'_r	Rotor inductance referred to the stator side (Ω)
R'_r	Rotor resistance referred to the stator side (Ω)
$V_{s\alpha}, V_{s\beta}$	Stator stationary axis components of stator currents (V)
$\psi_{r\alpha}, \psi_{r\beta}$	Rotor stationary axis components of stator flux (V-s)
J_L	Total inertia of the IM ($Kg.m^2$)
ω_m	Angular velocity
x	True state variables
$\hat{x}(k \mid k)$	Updated state estimates
y(k)	Measured variables
u(k)	Input variables
P(k | k)	Updated error covariance matrix
W(k)	State noise vectors
F	Jacobian matrix
G	Non linear measurement function
$\hat{x}(k \mid k-1)$	Predicted state estimates
$P(k \mid k-1)$	Predicted error covariance matrix
$\hat{y}(k \mid k-1)$	Predicted measurement
$\Upsilon(k \mid k-1)$	Innovation matrix
K(k)	Kalman gain
V(k)	Covariance matrix of innovation
$\chi(k \mid k, i)$	A set of 2L+I sigma points
$\chi(k \mid k-1, i)$	Predicted set of sigma points
$P_{ee}(k)$	Covariance matrix of innovations
$P_{\varepsilon e}(k)$	Cross covariance matrix between the predicted state estimate errors and innovations
W(i)	Associated weights

Greek Symbols

Φ	State transition matrix
μ	Mean of estimation error

Appendix-A

EKF Algorithm

Owing to a wealth of literature exists on the EKF algorithm, here we merely present the filter equation in a succinct way. The basic idea of the EKF is to linearize f and g (Equations (3) and (4) listed in the Section 2) using a first order Taylor series expansion, and then apply the standard Kalman filter. We have assumed in this work that the initial state and the sequence $\{w(k)\}$ and $\{v(k)\}$ are white, Gaussian and independent of each other. The most acclaimed EKF is as follows:

The predicted state estimates are obtained as:

$$\hat{\mathbf{x}}(k \mid k-1) = \hat{\mathbf{x}}(k-1 \mid k-1) + \int_{(k-1)T}^{(k)T} F\left[\mathbf{x}(\tau), \mathbf{u}(k-1)\right] d\tau \quad (A.1)$$

The covariance matrix of estimation errors in the predicted estimates is obtained as

$$P(k \mid k-1) = \Phi(k) P(k-1 \mid k-1) \Phi(k)^T + Q \quad (A.2)$$

where

$$A(k) = \left[\frac{\partial F}{\partial x}\right]_{[\hat{x}(k-1|k-1), u(k-1)]}; C(k) = \left[\frac{\partial G}{\partial x}\right]_{[\hat{x}(k-1|k-1), u(k-1)]}$$

$$\Phi(k) = \exp\left[A(k) * T\right]$$

$\Phi(k)$ is nothing but Jacobian matrices of partial derivatives of $F[.]$ with respect to x and w and $C(k)$ is the Jacobian matrix of partial derivatives of $H[.]$ with respect to x. The measurement prediction, computation of innovation and covariance matrix of innovation are as follows:

$$\hat{y}(k \mid k-1) = H\left[\hat{x}(k \mid k-1)\right] \quad (A.3)$$

$$\Upsilon(k \mid k-1) = y(k) - \hat{y}(k \mid k-1) \quad (A.4)$$

$$V(k) = C(k) P(k \mid k-1) C(k)^T + R \quad (A.5)$$

The Kalman gain is computed using the following equation

$$K(k) = P(k \mid k-1) C(k)^T V^{-1}(k) \quad (A.6)$$

The updated state estimates are obtained using the following equation

$$\hat{x}(k \mid k) = \hat{x}(k \mid k-1) + K(k) \Upsilon(k \mid k-1) \quad (A.7)$$

The covariance matrix of estimation errors in the updated state estimates is obtained as

$$P(k \mid k) = \left[I - K(k) C(k)\right] P(k \mid k-1) \quad (A.8)$$

It should be noted that the calculation of the covariances and the gain of the EKF are the same as those of the linear Kalman filter. The EKF always approximates $p\left[x(k) \mid Y^k\right]$ to be Gaussian. However, the distribu-

tions of the various random variables are no longer normal after undergoing their respective nonlinear transformations. Moreover, EKF uses first order terms of the Taylor series expansion of the nonlinear functions, so, large errors will be introduced when the models are highly nonlinear.

Appendix-B

Unscented Kalman Filter Algorithm (Julier and Uhlmann, 2000)

The unscented transformation (UT) is a method for calculating the statistics of a random variable, which undergoes a nonlinear transformation. A set of 2L+1 sigma points $\chi(k|k,i)$ with the associated weights $W(i)$ are chosen symmetrically about $\hat{x}(k|k)$ as follows:

$$\chi(k|k,0) = \hat{x}(k|k) \qquad W_0 = \frac{\kappa}{L+\kappa}$$

$$\chi(k|k,i) = \hat{x}(k/k) + \left(\sqrt{(L+\kappa)P(k|k)}\right)_i$$

$$W(i) = \frac{1}{2(L+\kappa)} \qquad i = 1:L$$

$$\chi(k|k,i) = \hat{x}(k|k) - \left(\sqrt{(L+\kappa)P(k|k)}\right)_{i-L}$$

$$W(i) = \frac{1}{2(L+\kappa)};\ i = L+1.....2L$$

where κ is a tuning parameter and for Gaussian distribution the tuning parameter can be obtained from the following relation $\kappa = 3 - L$. The 2L+1 sigma points have been derived from the state ($\hat{x}(k|k)$) and covariance of the state vector ($P(k|k)$), where L is the dimension of the state.

In the prediction step, the sigma points are propagated through the nonlinear differential equations to obtain the predicted set of sigma points as

$$\chi(k|k-1,i) = \chi(k-1|k-1,i) + \int_{(k-1)T}^{kT} F\left[\chi(\tau,i), \mathbf{u}(k-1)\right] d\tau;\ i = 0:2L \tag{B.1}$$

The predicted state estimates ($\hat{x}(k|k-1)$) are obtained from the predicted sigma points as

$$\hat{x}(k|k-1) = \sum_{i=0}^{2L} W(i)\chi(k|k-1,i) \tag{B.2}$$

The error covariance matrix ($P(k|k-1)$) is obtained from the predicted sigma points as

$$P(k|k-1) = \sum_{i=0}^{2L} W(i)[\chi(k|k-1,i) - \hat{x}(k/k-1)] [\chi(k|k-1,i) - \hat{x}(k/k-1)]^T + Q \tag{B.3}$$

The predicted sigma points are propagated through the nonlinear measurement equation to obtain the predicted measurement as

$$\hat{y}(k|k-1) = \sum_{i=0}^{2L} W(i) * H\left[\chi(k|k-1,i)\right] \tag{B.4}$$

The covariance matrix of the innovations ($P_{ee}(k)$) and the cross covariance matrix between the predicted state estimate errors and innovations ($P_{\varepsilon e}(k)$) are computed as:

$$P_{ee}(k) = \sum_{i=0}^{2L} W(i)\{H[\chi(k|k-1,i)] - \hat{y}(k|k-1)\} * \{H[\chi(k|k-1,i)] - \hat{y}(k|k-1)\}^T \tag{B.5}$$

$$P_{\varepsilon e}(k) = \sum_{i=0}^{2L} W(i)[\chi(k|k-1,i) - \hat{x}(k/k-1)] * \{H[\chi(k|k-1,i)] - \hat{y}(k|k-1)\}^T \tag{B.6}$$

$$\Upsilon(k|k-1) = y(k) - \hat{y}(k|k-1) \tag{B.7}$$

The Kalman gain matrix ($K(k)$) can be determined as follows:

$$K(k) = P_{\varepsilon e}(k) P_{ee}^{-1}(k) \tag{B.8}$$

The updated state estimates ($\hat{x}(k|k)$) are obtained using the linear update equation as in the Kalman filter.

$$\hat{x}(k|k) = \hat{x}(k|k\text{-}1) + K(k)|(k|k\text{-}1) \tag{B.9}$$

The covariance matrix of error in the updated state estimates ($P(k|k)$) are computed using

$$P(k|k) = P(k|k\text{-}1) - K(k) * P_{ee}(k) K^T(k) \tag{B.10}$$

The UKF does not approximate the nonlinear functions of system and measurement models as required by the EKF. Instead, the nonlinear functions are applied to sigma points to yield transformed samples, and the propagated mean and covariance are calculated from the transformed samples.

Energy and Power Engineering, **2010, 2, 90-94**
doi:10.4236/epe.2010.22013 Published Online May 2010 (http://www.SciRP.org/journal/epe)

An Approach to Human Adaptability towards its Built Environment: A Review

Richa Tiwari[1]*, Mukesh Pandey[2], Anupama Sharma[3]
[1]*Architecture, SPA, Bhopal, India*
[2]*Deptartment of Mechanical Engineering, University Institute of Technology, Bhopal, India*
[3]*Architecture & Planning MANIT, Bhopal, India*
E-mail: *richa_tiwari@rediffmail.com, anukhurasia@yahoo.com*
Received December 11, 2009; *revised February* 1, 2010; *accepted March* 17, 2010

Abstract

This paper deals with the human adaptability to its built environment. The built environment as we know it rarely finds itself adapting to its surrounding context, whether it be on the level of interaction with humans or the climate. Humans and nature both are in a constant state of flux; moving, changing, sensing, and reacting to their context and information they gather and perceive. A barrier is formed between the built environment and humans and nature due to the fact that their inherent characteristics are utterly contrasting. It is commonly estimated that persons in urban areas spend at least 80% of their time indoors. This suggests that the quality of the indoor environment can have a significant impact on comfort, health, and overall sense of well being. The indoor environment of buildings should thus be designed and controlled, as to provide a comfortable and healthy space for occupants. In order to maintain the quality of the indoor environment, we mechanically condition our buildings to achieve constant, uniform and comfortable environments. The maintenance of thermal equilibrium between the human body and its environment is one of the primary requirements. History of thermal comfort and climate design shows a definite relation between them and research is needed to know "What are comfort conditions?" and "How buildings could adapt themselves to these conditions".

Keywords: Adaptability, Human Comfort, Thermal Comfort, Thermal Performance, Adaptive Behaviour

1. Introduction

The phrase built environment refers to the man-made surroundings that provide the setting for human activity, ranging in scale from personal shelter to neighborhoods to the large-scale civic surroundings. Humans and many other mammals have unusually efficient internal temperature regulating systems that automatically maintain stable core body temperatures in cold winters and warm summers. In addition, people have developed cultural patterns and technologies that help them adjust to extremes of temperature and humidity.

Thermal comfort is essentially a subjective response. Current comfort standards such as ASHRAE-55 (American Society of Heating, Refrigerating and Air-Conditioning) [1] define thermal comfort as "state of mind, which expresses satisfaction with the thermal environment". While it may be partially influenced by a variety of contextual and cultural factors, a person's sense of thermal is primarily a result of the body's heat exchange with the environment. This is influenced by four parameters that constitute the thermal environment (Air-temperature, Radiant temperature, Humidity and Air speed) two personal parameters (Clothing and Activity level, or Metabolic rate) [2].

2. Thermal Adaptation

Environment and behaviour research teaches that ones experience of a place is a multi-variation phenomena and a reflection of the degree to which the place contributes to a person's objectives and expectations. In the adaptive approach to modeling-thermal comfort, thermal perception is affected by circumstances beyond the physics of the body's heat-balance, such as climate setting, social conditioning, economic considerations and other contextual factors [3]. The adaptive hypothesis states that one's satisfaction is achieved by matching the actual thermal environmental conditions prevailing at that point in time and space, with one's thermal expectations of what the

indoor climate should be like. A variable temperature standard links indoor temperatures to the climatic context of the building and accounts for thermal experiences and current thermal expectations of their occupants. In short, satisfaction occurs through appropriate adaptation to the indoor climatic environment.

3. Adaptive Behaviour

An alternative to traditional comfort theory-termed the "adaptative" can broadly be interpreted as the gradual diminution of the organism's response to repeated environmental stimulation which building occupants undergo in order to improve the "fit" of the indoor climate to their personal requirements [3]. This is achieved either through the way they interact with the environment, or modify their own behaviour, or because contextual factors and past thermal history change their expectations and thermal preferences. It is possible to distinguish three modes of the adaptive behaviour as shown in **Figure 1**.

3.1. Behavioural Adjustment

"Behavioural thermoregulation is well developed in humans and becomes preponderant and tends to supplant other forms of thermoregulation". In this a person makes modifications consciously or unconsciously, which in turn will modify heat and mass fluxes governing the body's thermal balance. This modifications or adjustments can be defined in terms of three categories: Personal adjustments e.g. changing personal variables like clothing, activity etc. and adjusting to the surroundings. Technological adjustments e.g. modifying the surroundings themselves like turning on fans or opening or closing of windows etc. Cultural adjustments, which include scheduling activities or adapting, dress codes etc.

3.2. Physiological Adjustments

Physiological adjustments include changes in the physiological responses that result from exposure to thermal environmental factors leading to gradual diminution in the strain induced by such exposure. These adjustments can be sub categorized: Genetic adaptation, including alterations, which become part of the genetic heritage of an individual. Acclimatization includes changes in the settings of the physiological thermoregulation system over a period of time. Physiological acclimatization is mediated by the autonomic nervous system and directly affects the physiological thermoregulation set points.

3.3. Psychological Adjustments

Psychological adjustments refer to perceptual adaptation and encompass the effects of cognitive and cultural

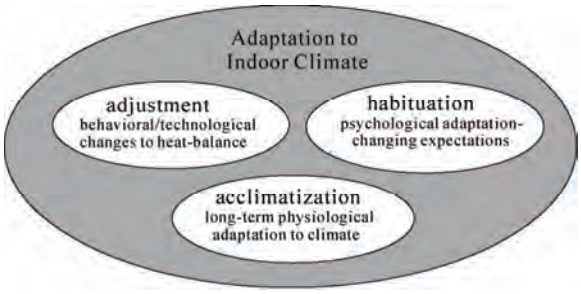

Figure 1. The three components of adaptation to indoor climate.

variables and describe the extent to which habituation and expectation alter one's perception of and reaction to sensory information due to past experiences and expectations [4].

The role of expectation in thermal comfort research was acknowledged in the earlier works of McIntyre, who stated that "a person's reaction to a temperature which is less than perfect will depend very much on his expectations, personality and what work he is doing at the time". Although the studies explain the differences in observed and predicted thermal sensations and acceptability, particularly of different environmental contexts such as the home vs office, or when comparing responses in air-conditioned vs naturally ventilated buildings. However evidences shows that building occupants become accustomed to levels of warmth prevailing within buildings on time scales of weeks or months. These scales translate into synoptic and seasonal processes operating in the outdoor atmospheric environment.

An important premise of the adaptive model is that the building occupant is no longer simply a passive recipient of the thermal environment as given, as in the case of a climate chamber experimental subject, but instead is an active agent interacting with all levels of the person-environment system via feedback loops. The adaptive hypothesis indicates that one's satisfaction with an indoor climate is achieved by a correct matching between the actual thermal environmental conditions prevailing at that point in time and space, and one's thermal expectations of what the indoor climate should be like. Thermal expectations result from a confluence of current and past thermal experiences, cultural and technical practices [3,5]. These relationships have been described in **Figure 2**, a schematic diagram developed by Auliciems [5] showing that a given set of indoor climatic conditions can elicit varying levels of comfort and satisfaction from building occupants, depending on culture or climatic and HVAC/architectural expectations.

4. Field Evidences for Human Adaptation

In recent years numbers of studies have been conducted on climate oriented building design to enhance

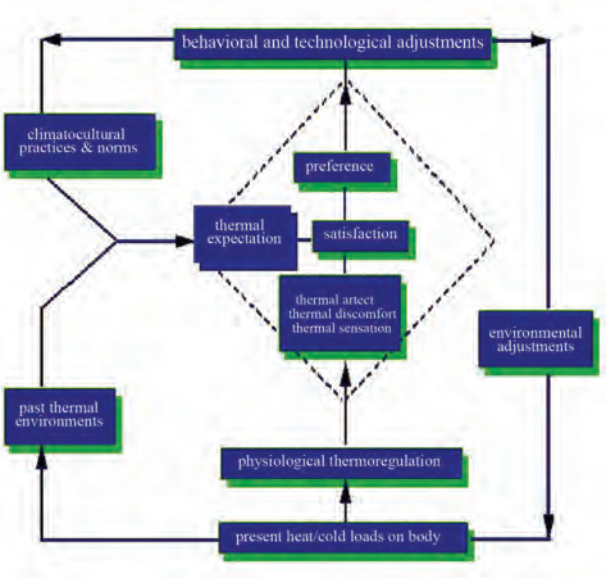

Figure 2. Schematic diagrams of thermal expectations.

thermal comfort conditions in living space and at the same time to reduce both the embodied and operational energy consumption. But results reported in these studies often deviate from the actual scenario. This discrepancy arises because most of the available thermal comfort standards are suited for air-conditioned buildings the situation leads to difficulty in estimating the thermal environments due to lack of adequate field experiments and long term data collection. In naturally ventilated buildings the occupants ability to modify the indoor environment is limited .An uncomfortable indoor environment might not be possible to control by passive means because of different socio-economic background and climatic condition. However, people living in naturally ventilated buildings are likely to be more tolerant.

Field studies were conducted for assessing the potential impacts of behavioural or psychological adaptations. Questionnaire based subjective measurements for this study was carried out. The respondents were asked to vote on ASHRAE 7 point thermal sensation scale followed by extensive interaction and filling up the questionnaire. This interaction helped us to record the common behavioural adaptations. Studies showed that, by utilizing behavioural adjustments such as wearing light clothing and restraining physical activities, local occupants were able to reach acceptable comfort in what-to immigrants from cold climates could be quite uncomfortable. The influence of clothing adjustments as a part of a study of office workers in naturally ventilated buildings in central India was also studied and it was found that the office occupants were comfortable across a wide range of seasonal temperatures, with neutralities varying between 15.7℃. in winter and 26.4℃ in summer. This concludes that at least two-thirds of the seasonal changes in comfort temperatures could be attributed to the flexibility in the traditional Indian clothing worn. While this supports the hypothesis that people use clothing adjustments to adapt themselves to a wide range of temperatures, it also suggests that there may be additional non-behavioural ways in which people adapt to the built environment.

ASHRAE Scale	Bedford scale
• *+3 Hot*	*7 Much too warm*
• *+2 Warm*	*6 Too warm*
• *+1 slightly warm*	*5 Comfortably warm*
• *0 Neutral*	*4 Comfortable*
• *-1 slightly cool*	*(neither cool nor warm)*
• *-2 Cool*	*3 Comfortably cool*
• -3 Cold	2 Too cool
	1 Much too cool

In addition to adjusting oneself to the environment, one can also manipulate the environment itself. The occupants always try to provide themselves the thermal environment customary to their own socio-cultural context and local climate during the residential building design. Occupants of the house have a propensity to adapt to the changes in thermal environment and try to be more comfortable. The temperatures corresponding to comfortable thermal environment are not fixed but are continuing response to changes in both indoor and outdoor environmental condition modified by climate and social custom. Sudden changes in the ambient temperature imposed on the occupants actually lead to discomfort. Hourly questionnaires were used to study whether the subjects had made adjustments to their clothing or to their furniture, doors, windows, shades, fans or any other part of the building to improve their comfort. Results indicated extensive occupant interaction to adjustments to controls or other environmental aspects of the room and less adjustments to clothing. Benton and Brager [6] also conducted a field study of thermal comfort, which addressed the availability, use, and effectiveness of both personal and environmental behavioural adaptation.

The role of personal control on expectation and thermal response has important implications in naturally ventilated vs centrally air-conditioned buildings. The adaptive hypothesis implies that if occupants in a centrally-controlled building have generally experienced fairy constant and uniform conditions, with limited opportunities for personal control, then they not unreasonably expect their building to automatically provide them with perfect comfort. And when it fails to meet those expectations, they will be more likely to judge that building harshly compared to a situation were they had control over those conditions. Studies by Paciuk [7] show evidence of this, he found that personal or environmental adjustments in air-conditioned buildings actu-

ally had a small effect on satisfaction. Studies were conducted in a mixed mode office building and it was found that, as temperatures rose above 24℃, people in centrally air- conditioned work areas began voting much higher on the thermal sensation scale than their colleagues in the naturally ventilated work areas, suggesting that they were less tolerant of higher temperatures and expected a higher standard in the thermal environment. Studies also show the adaptive actions commonly occurring in offices and the percentage of people who choose to employ them. The main adaptive behaviours discussed in the study were opening windows and switching on a fan. The environmental control of opening windows is highly preferred by occupants. When people have the freedom to modify the environment and make the necessary adjustment, they use these actions to compensate for the less comfortable thermal conditions.

Similar patterns were found in thermal comfort field studies of homes vs. office buildings, where a multitude of contextual factors, including perceived control, might influence expectation and thermal response. It was found that thermal neutralities and preferences were significantly lower in the home compared to the offices and the differences could not be accounted for by changes in clothing, activity, or air velocity. All these patterns support the notion that people grow to accept the thermal conditions to which they become accustomed to and that this acceptance might be influenced by factors such as personal control, energy bills, or concern for the environment. In short, when people have the possibility to control their environment (e.g. by being able to open a window), they are more easily thermally satisfied than when they perceive that they do not have control. Satisfaction occurs through appropriate adaptation to the indoor climate environment.

Field evidence for thermal adaptation shows a clear distinction between the thermal adaptation and responses of occupants in naturally ventilated buildings as opposed to air-conditioned buildings. The survey also showed that this difference could not entirely be accounted for by adjustments to clothing or activity. The most plausible explanation for these differences is the contextual influence of thermal history and its effects on expectations-past thermal experiences in a building create a benchmark for expectations of future thermal performance. In naturally ventilated buildings, indoor temperatures more closely match the diurnal and seasonal variations in outdoor temperatures. People recognize this, relax their expectations or individual "comfort criteria" and not only become more tolerant of the more varied, dynamic and non-uniform indoor conditions, but often prefer having a closer connection with weather and seasonal changes. Comfort ultimately depends on the degree to which the environment matches and contributes to our expectations and studies have consistently shown that this is strongly affected by our sense of whether or not conditions are under control. All these patterns support the notion that people grow to accept the thermal conditions to which they become accustomed to and that this acceptance might be influenced by factors such as personal control, energy bills, or concern for the environment. In short, when people have the possibility to control their environment (e.g. by being able to open a window), they are more easily thermally satisfied than when they perceive that they do not have control. Satisfaction occurs through appropriate adaptation to the indoor climate environment.

5. Thermal Performance of Buildings

The adaptive approach is based on statistical analysis of large number of thermal comfort field studies. Field studies have more immediate relevance to living conditions. The adaptive approach is a behavioural approach and rests on the observation that people are not passive in relation to their environments, but they express direct response to make themselves comfortable at the given time and opportunity. The adaptive opportunity may be provided for instance by switching fans or operable windows or ventilators in summer or by temperature controls in winter. Since clothing and activity levels are region specific and driven by socio-cultural set-up and climate, it is very difficult to find a single value for comfort temperature. Different respondents vote according to their own physiological, psychological and behavioural adaptations. Because of this fact, it has been found that at same temperature: different respondents have different thermal sensation or same thermal sensation at different temperatures. An increasingly wide range of temperature is permissible as the adaptive opportunities increased. Individual control is more effective in advancing comfort than group control.

6. Conclusions

Expectation plays a role for occupants of air-conditioned buildings as well, but in a different way. Here, thermal history comprises consistently cool, constant, uniform conditions, creating more stringent comfort criteria while biasing expectations towards constant HVAC set points rather than daily or seasonal fluctuations. Air-conditioned occupants were basing their evaluations on the benchmark of their own preconceptions of what air-conditioning should achieve, rather than on what it actually provided. In effect, this suggests that increasing levels of sophistication in environmental control systems and building services are on a treadmill of attempting to satisfy increasingly stringent occupant expectations.

The adaptive processes are operating on time scales ranging from seasonal, through synoptic to diurnal. Critics of the adaptive approach at various symposia or se-

minars have repeatedly asked the question: "how long must your people suffer in sub-optimal indoor climates before they become adapted?" The answer to this depends on which of the adaptive processes is being relied upon. While traditional research designs tend to look at responses at a given moment, experiments that intend to evaluate adaptive mechanisms need to take measurements over extended periods of time. Available evidence reviewed in this paper indicates that, in climate chamber experiments at least, the slower physiological adaptive process of acclimatization appears not to be relevant to this question of thermal neutrality and its fluctuations from day to day, week to week and season to season. As a result, the data analysis and model development will focus more heavily on the adaptive mechanisms of adjustment, and habituation/expectation.

One of the most important findings from our review of field evidence was the distinction between thermal comfort responses in air-conditioned vs. naturally ventilated buildings. Analysis suggested that behavioural adaptation incorporated in conventional heat balance models could only partially explain these differences and that comfort was significantly influenced by peoples expectations of the thermal environment. These contextual differences most likely resulted from a combination of past thermal history in buildings and differences in levels of perceived control. It is therefore essential that adaptive algorithms for comfort control utilize regressions from the architectural context for which they are intended. Regressions based on data from naturally ventilated buildings will probably be unsuitable as a control algorithm for air-conditioned buildings in which adaptive opportunities are severely constrained. There are numerous benefits to be gained from an improved understanding of the influence of adaptation on thermal comfort in the built environment. Enhanced levels of thermal comfort and acceptability among occupants reduced energy consumption and the encouragement of climatically responsive building design. These benefits can best be achieved through an ongoing, open dialogue and collaboration between the proponents of the "adaptive" vs. "heat balance" approach and I hope that my paper has provided a function for that to occur.

7. References

[1] Thermal Environmental Conditions for Human Occupancy, American Society of Heating, Refrigerating and Air-Conditioning Engineers Standard 55-1992, Ashrae, Atlanta, 1992.

[2] A. B. Lovins, "Air-Conditioning Comfort: Behavioural and Cultural Issues," E source, Colorado, 1992.

[3] F. Nicol, "Thermal Comfort—A handbook for Field Studies towards an Adaptive Model," University of East London, UK, 1993.

[4] M. A. Humphreys, "Field Studies and Climate Chamber Experiments in Thermal Comfort Research. Thermal Comfort: Past, Present and Future," BRE, UK, 1994.

[5] A. Auliciems, "Thermal Comfort," In: N. Ruck, Ed., *Building Design and Human Performance*, Van Nostrand, NY, 1989.

[6] G. Brager, "A Global Database of Thermal Comfort Field Experiments," *American Society of Heating, Refrigerating and Air-Conditioning Engineers Transactions*, 1998.

[7] M. Paciuk, "The Role of Personal Control of the Environment in Thermal Comfort and Satisfaction at the Workplace," Doctoral Dissertation, University of Wisconsin, Milwaukee, 1989.

Energy and Power Engineering, **2010, 2, 95-102**
doi:10.4236/epe.2010.22014 Published Online May 2010 (http://www.SciRP.org/journal/epe)

Co-liquefaction of Coal and Used Tire in Supercritical Water

Kwanruthai Onsri[1], Pattarapan Prasassarakich[1,2], Somkiat Ngamprasertsith[1,2*]
[1]*Fuels Research Center, Department of Chemical Technology, Faculty of Science, Chulalongkorn University, Bangkok, Thailand*
[2]*Center for Petroleum, Petrochemicals and Advance Materials, Chulalongkorn University, Bangkok, Thailand*
E-mail: *somkiat.n@chula.ac.th*
Received December 19, 2009; *revised January* 8, 2010; *accepted March* 3, 2010

Abstract

The co-liquefaction of lignite coal and used tire was performed in a 250-ml batch reactor, in supercritical water under a nitrogen atmosphere to investigate the effects of temperature (380-440℃), water/feedstock ratio (4/1-10/1 (wt./wt.)) and the % used tire content in the feedstock (0-100 wt.%) on the conversion efficiency, liquid yield and oil composition attained. The maximum conversion and oil yield were 67 and 50%, respectively, obtained at 400℃ at 1 min, with water/feedstock ratio of 10/1 and 80% used tire content. The distillation characteristics of the oil products, analyzed by simulated distillation gas chromatography, revealed that the oil composition depended significantly on the reaction temperature. The co-liquefaction of coal and used tire yielded a synergistically increased level of oil production. Moreover, the total conversion level obtained with co-liquefaction alone was almost equal to those obtained in the presence of either Fe_2O_3 or NiMo as catalysts, under the same conditions. Therefore, supercritical water is a good medium for the dissolution of the volatile matter from a coal and used tire matrix.

Keywords: Co-liquefaction, Coal, Used Tire, Supercritical Water

1. Introduction

In recent years, the growth in tire consumption has continued to expand concomitantly leading to the problem of the disposal of an ever increasing number of essentially non-biodegredable but flammable spent scrap tires without causing environmental pollution (including combustion). With in excess of 3.0 million tons per year of waste tires being produced in just the USA and Japan alone [1], this has become a major challenge. Indeed, currently perhaps only 60-70% of all used tires are recycled, and evens this requires the use of environmentally and economically costly processes including the use of solvents like n-hexane, toluene and tetralin [2,3]. Used tires are comprised of vulcanized natural and synthetic rubbers, zinc, sulfur and carbon black and, as such, contain polymeric aromatic structures that are somewhat similar to those in coal. Hence, the well-developed techniques used in coal utilization should theoretically be applicable to the pyrolytic destruction of waste tires and there has been an increasing amount of attention paid to the co-utilization of coal and waste tires. Indeed, given that coal liquefaction is enhanced by the addition of crude oil [4] which is a source of rubber constituents in tires, the co-liquefaction of coal and used tires is of obvious interest.

A number of different concepts for the degradation of spent tires in the presence of coal have hitherto contributed to the background knowledge. The processing of used tire and/or coal have been subjected to thermal pyrolysis and supercritical extraction using toluene, helium, nitrogen and water. Mastral *et al.* [5] investigated subbituminous coal-tire hydroprocessing and reported that oil formation and total solid conversion reached 45% and 70%, respectively, at a reaction temperature of 400℃, with a coal: tire ratio of 0.5 and 10 MPa initial hydrogen pressure. Moreover, the presence of rubber tire had a positive effect as an additive for coal hydropyrolysis and this was more relevant when tire feeds were coprocessed. In a similar vein, synergistic effects including increased total conversion levels and the yields of oil and asphaltene were attained during the simultaneous hydrogenolysis of coal and tire were reported [2-9]. Joung *et al.* [3]

studied the thermolysis of scrap tire using supercritical toluene (T > 318.6℃, P > 4.06 MPa) and cyclohexane under a nitrogen atmosphere and reported that the conversion level reached 100% for toluene once the critical state of toluene was reached (350℃). Indeed, temperature was far more important than other variables including pressure for the complete dissolution of tire materials. However, moving away from organic solvents as the hydrogen donor to the cheaper and environmentally friendlier water, the potential of supercritical water (SCW) was first evaluated by Funazukuri *et al.* [10] who reported that SCW was almost as effective as toluene for tire liquefaction, attaining around 57% of tire solids to oils. Finally, Park and Gloyna [11] reported that the liquefaction of used rubber tire by using SCW under a helium atmosphere attained a conversion and liquid yield level of 89% and 68%, respectively.

The type of solvent used is likely to play a key role as it acts as a medium to aid in the transport of hydrogen, as a heat transfer medium reactant (including hydrogen donor) and dissolution media to transport rubber and especially coal liquefaction products out of the matrix. However, previous research works have reported that SCW (T > 374℃, P > 22 MPa) is an alternative approach for the conversion of coal and tire into liquid products [10, 11]. The use of SCW as the reaction solvent can change the reaction rate, equilibrium, and principal reaction pathway, specifically around the critical point, because of the significant variation in water properties [12]. Thus SCW can dissolve hydrocarbons whose dielectric constant is widely variable. In addition, the use of SCW as opposed to organic solvents serves to both reduce the cost and avoid the problems associated with the removal of the solvent from the products. The separation of the liquid extracted from coal and organic solvents typically requires a tedious procedure to achieve any degree of completion and product purity, and is both economically and environmentally costly [13].

In this study, coal and used tire co-liquefaction were conducted in SCW under a N_2 atmosphere and the effects of the reaction temperature, the water/feedstock ratio, % used tire content in feedstock and the presence of catalysts on the co-liquefaction efficiency were investigated and are discussed with reference to the product composition.

2. Experiment Apparatus and Procedure

2.1. Material and Chemicals

The lignite coal used in this study was obtained from the Mae Moh lignite mine in Lampang province, northern Thailand. The used tire was obtained from Union Pattanakij Ltd. They were grounded, sieved (particle size is in range of 250-850 micron), dried at 110℃ overnight and then kept in the desiccator. The proximate and ultimate analysis of lignite and used tire are presented in **Table 1**.

Table 1. Proximate and ultimate analysis of coal and used tire.

	Coal	Used tire
Proximate analysis (wt.% db[1])		
Ash	21.6	3.5
Fixed carbon	59.4	67.8
Volatile matter	19.1	28.7
Moisture (original sample, %)	17.7	1.1
Ultimate analysis (wt.% daf[2])		
Carbon	66.4	85.8
Hydrogen	5.1	8.0
Nitrogen	2.6	0.5
Sulfur	4.6	1.5
Oxygen (by difference)	21.3	4.3
H/C atomic ratio	0.9	1.1
Heating value (MJ/kg)	21.3	33.6

[1] db = dry basis, [2] daf = dry ash-free basis

Other chemicals were: Tetrahydrofuran (THF) (+ 99.99%) purchased from Fisher Chemicals, Dichloromethane (CH_2Cl_2) and Anhydrous sodium sulfate purchased from CARLO ERBA and Carbon disulfide (CS_2) (99%) purchased from Merck.

2.2. Procedure

The experimental scheme for co-liquefaction of coal and used tire constituent is summarized in **Figure 1** and schematic of apparatus is shown in **Figure 2**. The co-liquefaction reactions were carried out in a 250-ml reactor (Parr reactor model 4843). The reactor filled with water under nitrogen atmosphere. The water-filling content (percentage water volume to reactor volume) was 15-17% which this amount of water caused the pressure approaching 24-25 MPa at the desired temperature (380 -440℃). The calculated amounts of coal and used tire were loaded in the reactor at the specific ratio.

The reactor was heated to the desired temperature, above the water critical temperature at a heating rate of 5℃/min, and held at this temperature for 1 min. The reactor was then cooled to room temperature and the products transferred by washing into, and extracted with THF, in an ultrasonic bath. After the THF extraction, the product mixture was filtered to separate solid from liquid, and the solid residue was dried for 4 h in an oven at 110℃ to remove the residual solvent. The liquid products were separated into both oil and aqueous phases by CH_2Cl_2 using a separation funnel. Anhydrous sodium sulfate was added to the isolated oil phase to remove the trace

amounts of residual water remaining in the oil phase and then evaporated in a vacuum rotary evaporator at 60℃ and 400 mmHg to remove the CH_2Cl_2 and THF solvent residues. The evaporated liquid (oil) was weighed to calculate the liquid yield. The total conversion, liquid and gas yields and solid residue levels were calculated by the following expressions:

% Conversion = 100[(Wdaf – WRT)/Wdaf]

% Liquid yield = 100[Wliq/Wdaf]

% Solid residue = 100[WRT/Wdaf]

% Gas yield = 100 - % Liquid yield - % Solid residue

where: Wdaf = wt. of dry-ash free coal and used tire mixture, WRT = wt. of dry-ash free residue remaining after THF solvent wash and dry, Wliq = wt. of liquid. All experiments were conducted in duplicate.

2.3. Product Analysis

In this study, the raw coal and used tire was analyzed for proximate analysis, total sulfur and determined the heating value by ASTM D2492, D3177 and D2015, respectively. The carbon, hydrogen and oxygen were performed using a CHN analyzer (Leco CHN-2000).

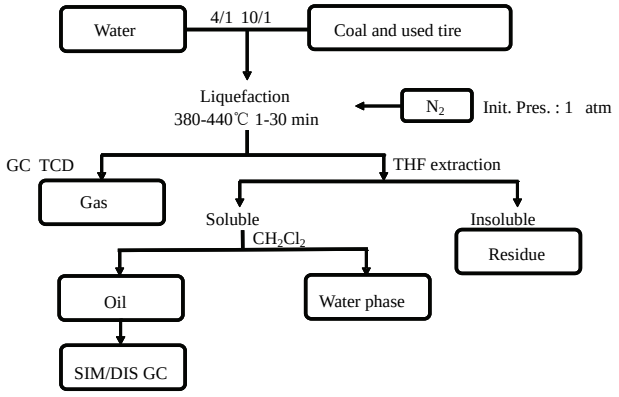

Figure 1. Experimental scheme.

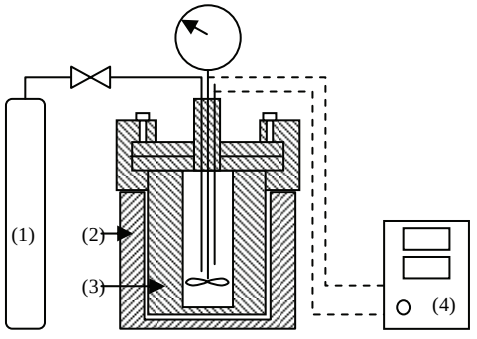

Figure 2. Schematic diagram of the apparatus. (1) N_2 gas cylinder. Parr reactor model 4843 consisted of; (2) Heater; (3) 250-ml high temperature and pressure reactor; (4) Temperature and pressure controller.

The liquid product was analyzed by Simulated Distillation Gas Chromatography (SIM/DIS GC, Varian Model CP-3800) according to ASTM D2887. Star Simulated Distillation version 5.5 software was used for data collection and processing. The liquid was dissolved in 1% (v/v) CS_2 and a 15 m × 0.25 mm Cp-SIL5CB column was used for separation. The oven temperature was raised from 30 to 370℃ at a constant heating rate of 20℃/min. The distillation curve was evaluated to fractions as follows: IBP-200℃, gasoline; 200-250℃, kerosene; 250-350℃, light gas oil; 350-370℃, gas oil; and 370℃-FBP, long residue.

The gaseous product was analyzed by Gas Chromatograph with a Thermal Conductivity Detector (GC-TCD, Shimadzu GC-2014). The GC-TCD conditions were as follows: 90℃ injection temperature; He carrier gas; Porapak Q column and 50℃ column temperature.

3. Results and Discussion

3.1. Preliminary Study

In the initial stage of study co-liquefaction of coal and used tire, the factorial design was used to analyze the significant process variables. Three variables such as temperature, water/feedstock ratio (wt./wt.) and used tire content in feedstock (wt.%) were chosen. Each of the variables was coded at two levels: -1 and +1 as shown in **Table 2** and the average 2^3 (= 8) experimental results including % conversion and % liquid yield of 2 replications were showed in **Table 3**.

The analysis using the 2-level factorial design method was based on an evaluation of variance ratios. Such comparison helped to determine whether or not significant difference existed among the means of several groups of observation. It was assumed that each group followed a normal distribution and its trend of the response between ranges of studied variables is linear. The F-test (95% confidence limits) method was used. The calculated results were showed in **Table 4**. These results showed that only temperature had effect on % conversion, while all three variables (temperature, Water/feedstock (wt./wt.) ratio and % used tire in feedstock) had effect on % liquid yield.

However, the effect of reaction time on the product distribution of the co-liquefaction was not studied, be-

Table 2. Factorial design of experiments.

Factor	Level	
	-1	+1
Temperature (℃), A	380	440
Water/feedstock ratio (wt./wt.), B	4/1	10/1
% Used tire content in feedstock (wt.%), C	20	80

Table 3. Experimental results obtained from factorial design for co-liquefaction experiments.

Factorial Design*	Factor			% Conversion	% Liquid yield
	Temperature (℃), A	Water/feedstock Ratio (wt./wt.), B	% Used tire content in feedstock (wt.%), C		
(1)	380	4/1	20	53.9	15.0
a	440	4/1	20	62.6	24.9
b	380	10/1	20	56.3	25.5
ab	440	10/1	20	63.4	28.6
c	380	4/1	80	53.2	26.6
ac	440	4/1	80	62.4	36.0
bc	380	10/1	80	60.0	40.2
abc	440	10/1	80	68.2	41.6

* Reaction conditions are denoted according to statistical nomenclature;
e.g. ab represents high levels of factors A and B and low levels of C and D (see **Table 2**)

Table 4. Analysis of variance for co-liquefaction experiments. (a) for % conversion; (b) for % liquid yield.

Source of Variation	Sum of Square	Degrees of Freedom	Mean Square	F_0
A	137.74	1	137.74	37.21*
B	30.69	1	30.69	8.29
AB**	0.90	1	0.90	0.24
C	7.29	1	7.29	1.97
Error	11.10	3	3.70	
Total	187.73	7		

(a)

Source of Variation	Sum of Square	Degrees of Freedom	Mean Square	F_0
A	70.92	1	70.92	9.13*
B	138.83	1	138.83	17.87*
C	315.63	1	315.63	40.63*
Error	31.07	4	7.77	
Total	556.45	7		

(b)

* Significant in F-test with 95% confidence limits, $F_{0.05,1,3} = 10.13$ ($F_0 > F_{0.05,1,3}$)
* Significant in F-test with 95% confidence limits, $F_{0.05,1,4} = 7.71$ ($F_0 > F_{0.05,1,4}$)
** Two-factor interaction effects of factors A and B (see **Table 2**)

cause the results from initial experiments of liquefaction of the used tire, as shown in **Figure 3**, showed that the reaction time (elapsed time after the temperature reached the desired temperature) did not affect the product distribution. Moreover, the previous studies [14-16] reported that the coal and some polymers including rubber

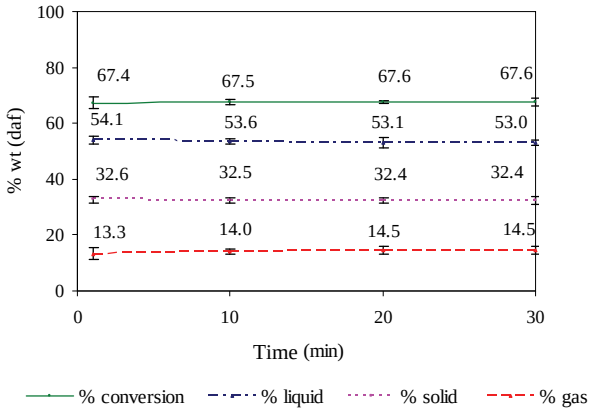

Figure 3. The effect of temperature on the distribution of products for used tire liquefaction. (Temperature 420℃; water/feedstock ratio of 10/1).

and plastics can be decomposed and give the highest oil yield within 1 min. Thus, we used the reaction time of 1 min for all of co-liquefaction experiments.

3.2. The Effect of Temperature

Thermal cracking is the principal reaction in SCW and the effect of temperature on thermal cracking is important. Thermogravimetric analysis curves revealed the weight loss of used tire when pyrolyzed at a constant heating rate of 10℃/min within a temperature range of 25-900℃ under a nitrogen atmosphere (**Figure 4**). The decomposition of used tire begins in earnest near 380℃ and is essentially completely decomposed at 480℃. Therefore, the chosen temperature range for all subsequent co-liquefaction experiments was 380-440℃. **Figure 5** summarizes the variation in product yield with reaction temperature at a reaction time of 1 min, a water/feed stock ratio of 10/1 and a substrate composition

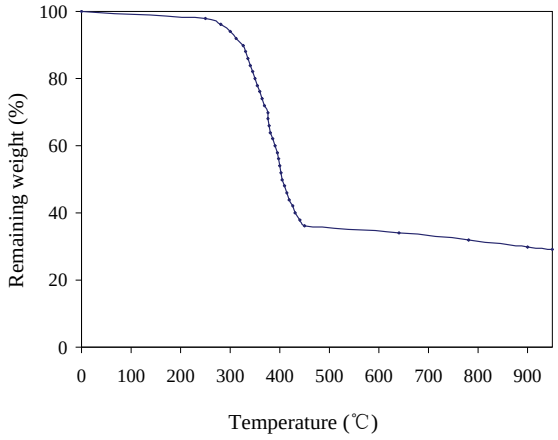

Figure 4. Thermogravimetric analysis curve of used tire.

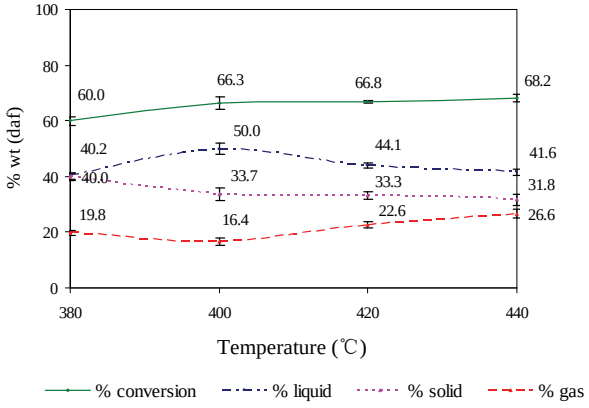

Figure 5. The effect of temperature on the distribution of products for co-liquefaction. (Reaction time 1 min; water/feedstock ratio of 10/1; 80% used tire content in feedstock).

of 80% used tire. The yield of liquid product increased from that obtained at 380℃ to a maximum level at 400℃ and thereafter decreased with further temperature increases. At lower temperature, the liquid could be extracted from coal, the used tire was decomposed and then yielded the heavy liquid products. However, with increasing reaction temperatures, the residue yield decreased because of the further thermal decomposition of heavy liquid product and solid residue could be took place and resulted in decreased liquid and residue yields at temperatures above 400℃ and a concomitant increase in gas yields.

The total conversion level, which increased with temperature rises from 380 to 400℃, did not significantly change with further temperature increases from 400 to 440℃, whilst the liquid yield was decreased, presumably via the decomposition of long chained hydrocarbons into gaseous products. Moreover, the total conversion attained at 400℃ was almost equal to that attained at 440℃ some 8 min later. Therefore, it can be concluded that the optimum temperature and reaction time was 400℃ and 1 min.

3.3. The Effect of Water/Feedstock Ratio

The effect of varying the water/feedstock ratio on the yield of products attained at 400℃ with a reaction time of 1 min and 80% used tire content is summarized in **Figure 6**. Whilst the yield of gas remained stable, the liquid oil yield was slightly increased with increasing water content and reached 50% at the maximum water/feedstock ratio of 10/1 whilst the levels of residual solids were concomitantly decreased. The mechanism of coal pyrolysis starts with SCW diffusing into the coal matrix and acting as a medium for the dissolution of coal fragments. At the supercritical state, the static dielectric constant of water decreases dramatically, leading to the miscibility of nonpolar organic compound with SCW [15, 17,18]. The products from coal pyrolysis can dissolve and disperse in the SCW and, as a result, the conversion of coal is enhanced in the presence of water.

Moreover, the water gas shift reaction ($CO + H_2O \rightarrow CO_2 + H_2$) occurs as a side reaction during coal and used tire conversion in SCW. The CO produced from partial-oxidation of oxygen-contained functional groups of coal and then reacts with water in SCW to produce carbon dioxide and hydrogen. The appearance of carbon dioxide in the gas product was shown in **Figure 7**. Increasing the water/feedstock ratio in partial-oxidation of coal in SCW causes the equilibrium to favor carbon dioxide and hydrogen production leading to higher rates and levels of reactive intermediate hydrogen production, which is the actual hydrogenation agent [12]. The generated hydrogen reacts with free radicals produced from the thermal cracking of coal and used tires, and so liquid products are increased.

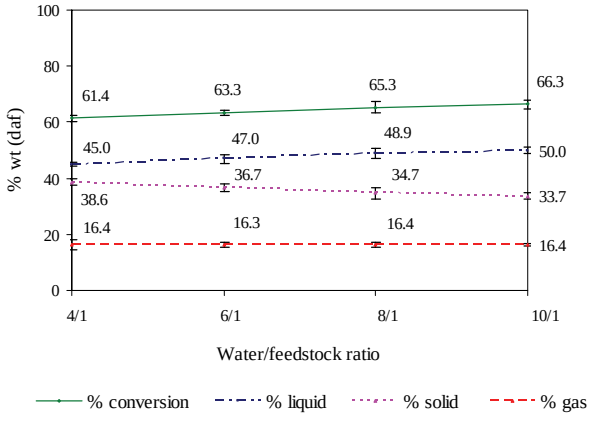

Figure 6. The effect of the water/feedstock ratio on the distribution of products from co-liquefaction of coal and used tire. (Reaction time 1 min; temperature 400℃; 80% used tire content in feedstock).

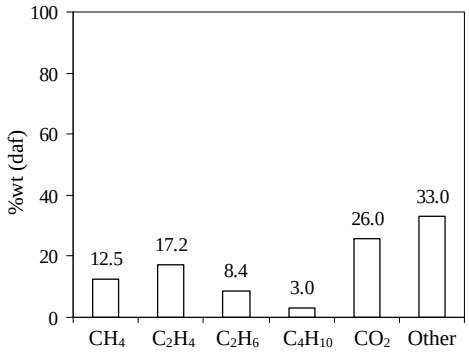

Figure 7. The effect of % used tire content in feedstock on the distribution of gas products obtained from their co-liquefaction. (Reaction time 1 min; temperature 400℃; water/feedstock ratio of 10/1).

3.4. The Effect of the % Used Tire Content in Feedstock

The effect of varying the amount of used tire content in feedstock on the product composition attained at 400℃ with a water/feedstock ratio of 10/1 and a reaction time of 1 min are summarized in **Figure 8**. The liquid yield attained was increased from 39.1 to 50.0% as the used tire content in feedstock was increased from 20 to 80 wt.%. Because the depolymerization of used tires occurs easier than that for coal, likely due to the simpler structure of the tires, the thermal cracking of tire to form free radicals and water-gas shift reaction are stabilized by those produced during coal cracking. This results in a more efficient co-liquefaction process with coal and used tire relative to the liquefaction seen with only coal under the same conditions.

Moreover, these results show that adding used tire to the coal liquefaction process increases the total conversion of coal and the oil yield obtained. For example, the total conversion and oil yield obtained from using 80% used tire content in feedstock were both synergistically higher than with only coal or tires alone under the same conditions.

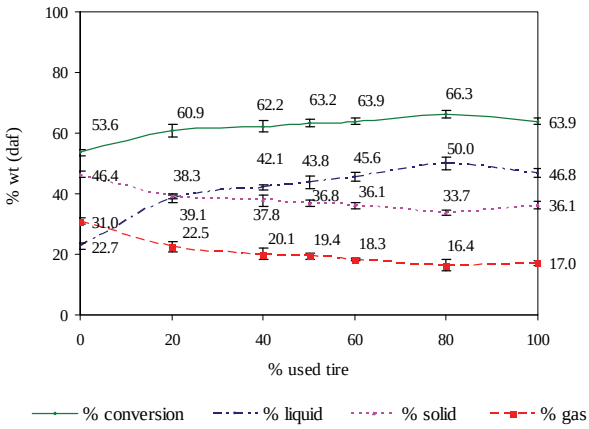

Figure 8. The effect of the % used tire content in feedstock on the distribution of products obtained from their co-liquefaction. (Reaction time 1 min; temperature 400℃; water/feedstock ratio of 10/1).

3.5. Analysis of the Liquid Products Obtained

The liquid products obtained from the co-liquefaction were divided into gasoline, kerosene, light gas oil, gas oil and long residue by using Simulated Distillation Gas Chromatography (SIM/DIS GC). The effect of varying the reaction temperature, water/feedstock ratio and % used tire content in feedstock on the oil product composition are summarized in **Figure 9**. The temperature and % used tire content in feedstock have a detectable effect upon the oil composition with the content of gasoline and kerosene being increased whilst long residues were decreased with both increasing temperature and % used tire content in feedstock. In contrast, the water/feedstock ratio had no discernable effect on the oil composition. The more severe thermolysis and depolymerization of the coal and used tire seen with increasing temperature and % used tire content in feedstock thus resulted in an increased yield of lighter and intermediate compounds at the expense of the higher MW compounds.

3.6. The Effect of Catalysts

The effect of using two established coal liquefaction catalysts, 2.5% (w/w) Fe_2O_3 and NiMo (Ni: 0.2 wt% db coal, Mo: 0.6 wt% db coal) particles, on the co-liquefaction of coal and tires was evaluated. Catalyst loading of the coal was prepared by an in situ impregnation method [19,20]. The co-liquefaction in SCW with or without catalysts was performed at 400℃ for 1 min, with a water/feedstock ratio of 10/1, and 80% used tire content in feedstock.

The total conversion obtained in the presence of either of the two catalysts was almost equal to that obtained in their absence (**Figure 10**). However, the gas yield was increased significantly in the presence of either catalyst, with a concomitant reduction in oil yield. Thus, the catalysts perform further thermal cracking to give lighter liquid products. However, considering the absence in changes in total conversion, for solid to oil conversion (*i.e.* % oil yield), it can be concluded that the process does not require either catalyst or additive.

4. Conclusions

In this work, the total conversion and liquid yield obtained from the co-liquefaction of coal and waste tire attained were 66 and 50%, respectively, at the optimum reaction condition of 400℃ for 1 min, with wa-

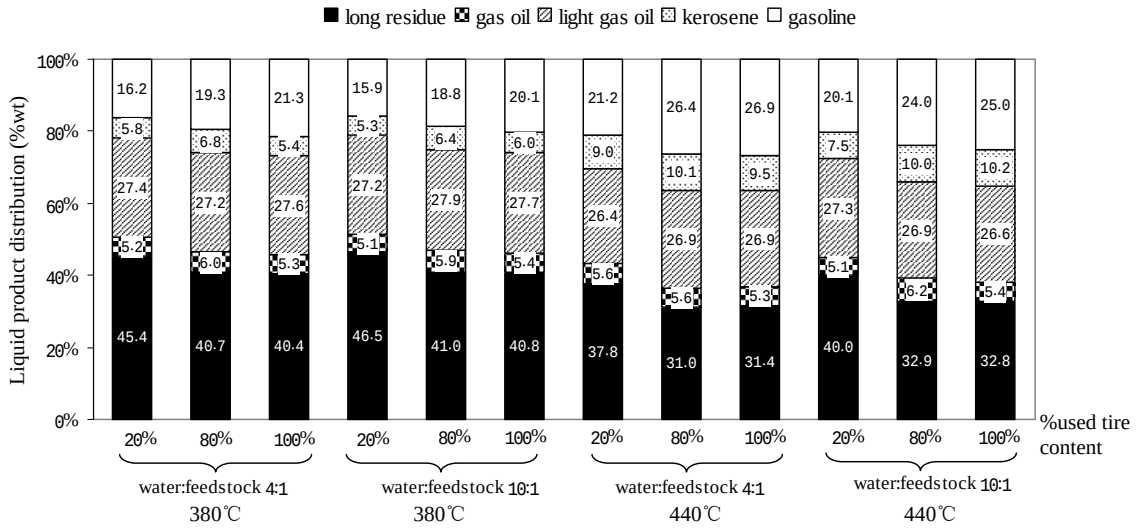

Figure 9. The effect of temperature, water/feedstock ratio, and % used tire content in feedstock upon the composition of liquid products obtained from co-liquefaction.

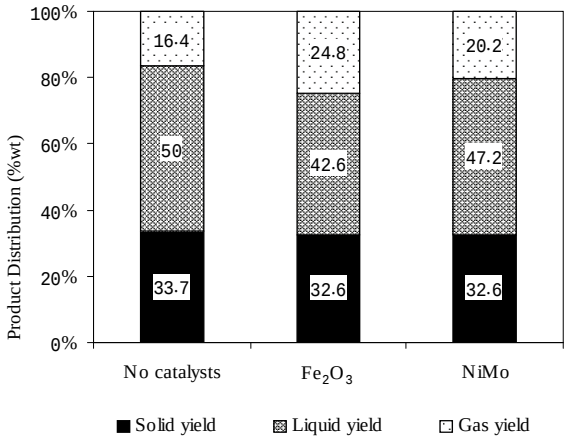

Figure 10. The effect of catalyst upon the distribution of products obtained from co-liquefaction of coal and used tire. The calculated total conversion (%) is in parenthesis above each bar. (400°C for 1 min, water/feedstock ratio of 10/1, 80% used tire content in feedstock).

ter/feedstock ratio of 10/1 and 80% used tire content. The total conversion increased with increasing temperature whilst liquid yields obtained increased with increasing temperature, water/feedstock ratio and % used tire content in feedstock. Moreover, as reported in other systems, the addition of used tire to the coal co-liquefaction had a synergistic effect, whilst the key factor affecting the liquid product composition was temperature. SCW is a suitable medium to extract the volatile matter from waste tire, as a tire-coal matrix, without the need to use catalysts, long reaction times or organic solvents. Therefore, the co-liquefaction of coal and used tire in SCW is an attractive way for reducing waste tires by means of giving a moderate oil yield without the need for environmentally and economically costly long reaction times and chemical solvents, but rather provides rapid and easy separation of the oil product from all the other residual components.

5. Acknowledgements

This work was supported by Center for Petroleum, Petrochemicals and Advanced Materials and Graduate School, Chulalongkorn University.

6. References

[1] P. T. Williams and R. P. Bottrill, "Sulfur-Polycyclic Aromatic Hydrocarbons in Tyre Pyrolysis Oil," *Fuel*, Vol. 74, No. 5, 1995, pp. 736-742.

[2] G. C. Hwang, J. H. Choi, S. Y. Bae and K. Kumazawa, "Degradation of Polystyrene in Supercritical Hexane," *Korean Journal of Chemical Engineering*, Vol. 18, No. 6, 2001, pp. 854-861.

[3] S. N. Joung, S. W. Park, S. Y. Kim, K. P. You and S. Y. Bae, "Thermolysis of Scrap Tire Using Supercritical Toluene," *Korean Journal of Chemical Engineering*, Vol. 16, No. 5, 1999, pp. 602-607.

[4] A. V. Cugini, R. G. Lett and I. Wender, "Coal/Oil Coprocessing Mechanism Studies," *Energy and Fuels*, Vol. 3, No. 2, 1989, pp. 120-126.

[5] A. M. Mastral, R. Murillo, M. J. Perez-Surio and M. Callen, "Coal Hydrocoprocessing with Tires and Tire Components," *Energy Fuels*, Vol. 10, No. 4, 1996, pp. 941-947.

[6] Z. Liu, J. W. Zondolo and D. B. Dadyburjor, "Tire Liquefaction and its Effect on Coal Liquefaction," *Energy*

Fuels, Vol. 8, No. 3, 1994, pp. 607-612.

[7] A. M. Mastral, R. Murillo, M. S. Callen and T. Garcia, "Evidence of Coal and Tire Interactions in Coal-Tire Coprocessing for Short Residence Times," *Fuel Processing Technology*, Vol. 69, 2000, pp. 127-140.

[8] M. Sugano, D. Onda and K. Mashimo, "Additive Effect of Waste Tire on the Hydrogenolysis Reaction of Coal Liquefaction Residue," *Energy Fuels*, Vol. 20, No. 6, 2006, pp. 2713-2716.

[9] Y. Tang and C. W. Curtis, "Thermal and Catalytic Coprocessing of Waste Tires with Coal," *Fuel Processing Technology*, Vol. 46, No. 3, 1995, pp. 195-215.

[10] T. Funazukuri, T. Takanashi and N. Wakoa, "Supercritical Extraction of Used Automotive Tire with Water," *Journal of Chemical Engineering of Japan*, Vol. 20, 1987, pp. 23-27.

[11] S. Park and E. F. Gloyna, "Statistical Study of the Liquefaction of Used Rubber Tyre in Supercritical Water," *Fuel*, Vol. 76, No. 11, 1997, pp. 999-1003.

[12] N. Akiya and P. E. Savage, "Roles of Water for Chemical Reactions in High-Temperature Water," *Chemical Reviews*, Vol. 102, No. 8, 2002, pp. 2725-2750.

[13] S. Sangon, S. Ratanavaraha, S. Ngamprasertsith and P. Prasassarakich, "Coal Liquefaction Using Supercritical Toluene-Tetralin Mixture in a Semi-Continuous Reactor," *Fuel Processing Technology*, Vol. 87, No. 3, 2006, pp. 201-207.

[14] X. Su, Y. Zhao, R. Zhang and J. Bi, "Investigation on Degradation of Polyethylene to Oils in Supercritical Water," *Fuel Processing Technology*, Vol. 85, No. 8-10, 2004, pp. 1249-1258.

[15] L. Cheng, R. Zhang and J. Bi, "Pyrolysis of a Low-Rank Coal in Sub- and Supercritical Water," *Fuel Processing Technology*, Vol. 85, No. 8-10, 2004, pp. 921-932.

[16] S. Sunphorka, P. Prasassarakich and S. Ngamprasertsith, "Co-liquefaction of Coal and Plastic Mixture in Supercritical Water," *Journal of Scientific Research Chulalongkorn University*, Vol. 32, No. 2, 2007, pp. 101-109.

[17] H. Hu, S. Guo and K. Hedden, "Xtraction of Lignin with Water in Sub- and Supercritical States," *Fuel Processing Technology*, Vol. 53, 1997, pp. 267-277.

[18] M. Watanabe, H. Hirakoso, S. Sawamoto, T. Adschiri and K. Arai, "Poly Ethylene Conversion in Supercritical Water," *Journal of Supercritical Fluids*, Vol. 13, No. 1-3, 1998, pp. 247-252.

[19] Y. Artanto, W. R. Jackson, P. J. Redlich and M. Marshall, "Liquefaction Studies of Some Indonesian Low Rank Coals," *Fuel*, Vol. 79, No. 11, 2000, pp. 1333-1340.

[20] Z. Liu, J. Yang, J. W. Zondlo, A. H. Stiller and D. B. Dadybujor, "*In situ* Impregnated Iron-Based Catalysts for Direct Coal Liquefaction," *Fuel*, Vol. 75, No. 1, 1996, pp. 51-57.

Energy and Power Engineering, **2010, 2, 103-110**
doi:10.4236/epe.2010.22015 Published Online May 2010 (http://www.SciRP.org/journal/epe)

An Improved Design of a Fully Automated Multiple Output Micropotentiometer

Hala Mohamed Abdel Mageed[1], Ahmed Faheem Zobaa[2], Mohamed Helmy Abdel Raouf[1], Abla Hosni Abd El-Rahman[1], Mohamed Mamdouh Abdel Aziz[3]
[1]*National Institute for Standards, Giza, Egypt*
[2]*University of Exeter, Exeter, UK*
[3]*Cairo University, Giza, Egypt*
E-mail: *halaabdelmegeed@yahoo.com*
Received December 1, 2009; *revised January* 7, 2010; *accepted March* 21, 2010

Abstract

This paper describes in details a new design of a fully automated multiple output micropotentiometer (μpot). A prototype has been built at the National Institute for Standards (NIS), Egypt to establish this highly improved AC voltage source in the millivolt range. The new device offers three different outputs covering a wide frequency range from only one outlet. This valuably supports the precise sourcing ranges of low AC voltage at NIS. The design and the operation theory of this prototype have been discussed in details. An automatic calibration technique has been introduced through specially designed software using the LabVIEW program to enhance the calibration technique and to reduce the uncertainty contributions. Relative small AC-DC differences of our prototype in the three output ranges are fairly verified. The expanded uncertainties of the calibration results for the three output ranges have been faithfully estimated. However, further work is needed to achieve the optimum performance of this new device.

Keywords: Multiple Output μpot, AC-DC Transfer Standard, Single Junction Thermal Converter, Calibration, Uncertainty

1. Introduction

In recent years new types of AC instruments and high precision AC-DC voltage transfer devices for low voltages and high frequencies have been widely adopted in metrological and industrial laboratories. Therefore, new activities for developing systems operating at these levels have been undertaken [1,2].

The measurement of AC voltages and currents may involve several methods [3]. However, thermal converters are mostly used in national measurement institutes and other laboratories as the basis for deriving AC quantities (voltage, current, and power) referring to known DC quantities [4]. Normally, the measurement of AC quantities with thermal converters implies the transformation of the electrical energy into thermal energy by means of the Joule heat dissipated in the thermal converter heater resistor [5,6]. Evidently, these thermal converters are the most accurate AC-DC transfer standards for the transfer of alternating voltage and current to the equivalent DC quantities [7,8]. Commonly, there are two types of thermal converters: single-junction thermal converter (SJTC) and multi-junction thermal converter (MJTC) [6]. Although MJTCs in planar technique are used for voltages down to 100 mV [9], SJTC are mainly used as thermal current converters because they are simpler and easily available [8].

In national metrology institutes, the accurate AC instruments are mostly calibrated using micropotentiometers (μpots), which are basically voltage sources [10,11]. The μpots are developed for the generation of accurate low AC voltages at wide range of frequencies. In actual fact the SJTC μpots are still highly admitted specially those designed with thin-film radial resistors, because radial resistors so far ensure optimum frequency response [12].

As accurate calibration of low AC voltages presents several challenges, we implemented the design of a new simple versatile accurate multiple output μpot in order to enhance the capabilities of NIS by extending its precise output sourcing ranges of low AC voltage.

The traceability for the precision sourcing of AC voltages in the ranges of 10 mV, 25 mV, 50 mV, 100 mV, 200 mV, and 500 mV at frequencies from 10 Hz to 20

KHz had been derived at NIS from a set of SJTC μpots which had been previously fabricated and calibrated [13]. Nevertheless, each μpot of that set produces only one output AC voltage range.

In this work we aimed to build a fully automated prototype of a multiple range μpot offering three different output millivolt ranges from only one outlet through two disc resistors. These three output ranges are 300 mV, 400 mV, and the parallel resistances combination equivalent value (171.4 mV) at frequencies from 10 Hz to 10 KHz. Furthermore, the automatic calibrations of the new device, the AC-DC differences (δ), and the expanded uncertainties for the results had been fully investigated in this work.

2. Construction of the New Developed Multiple Output μPot

Figure 1 demonstrates the block diagram of the multiple output μpot which consists of a N type male coaxial input connector, an ultra high frequency (UHF) type SJTC with nominal rated current of 5 mA, and a microcontroller (AT89C2051). The microcontroller is used to control two mechanical relays through four-push button switches. The first switch actuates the PC to automatically control all the circuit, while the other three can be manually activated to change between two radial resistors with nominal values of 60Ω, and 80Ω. Each one of the two resistors consists of ten parallel equal resistors and is securely soldered into the output female N-type coaxial connector for producing the output voltage.

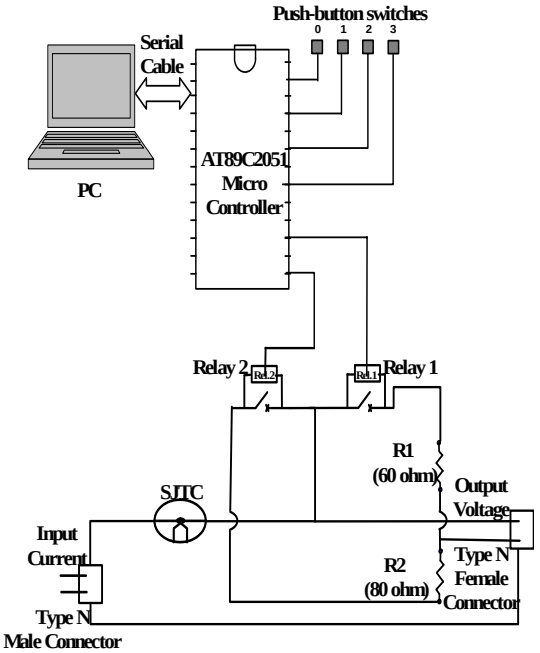

Figure 1. Block diagram of the multiple output μpot.

In this technique, each one of the two resistors can be easily chosen when the corresponding push button switch is pressed while; the third button introduces their parallel combination (34.29Ω) by activating the two relays at the same time.

The AT89C2051 microcontroller is a low voltage, high performance and powerful microcomputer which provides a highly flexible and cost effective solution to many embedded control applications. In addition, the AT89C205 microcontroller is designed with static logic (binary code) which is stored in the microcontroller ROM through a C-language program [14].

The μpot is normally designed to provide a precisely determined voltage at its output terminal when it is excited with an external source. The input current flows through the heater of the SJTC to the radial resistor and the voltage drop across the radial resistor induces a low-impedance source of AC voltage. The output voltage is nominally the product of the heater current and the resistance of the radial resistor [15].

The measurement principle of the SJTC is based on converting the electrical signal to a heat power [16]. In such a converter, energy dissipated by an AC current flowing through a heater resistor, raises its temperature above the ambient. It is then compared to an equal energy dissipated by a DC current flowing through the same heater. The increase in the temperature of the heater resistor by the rms of the AC signal and the equivalent DC signal is proportional to the dissipated energy and it is then measured using the thermocouple. A relative difference between the response of the converter to AC and DC inputs, called AC-DC transfer difference, is determined from these two measurements [17]. The AC-DC transfer difference is the main objective of the metrological characterization of each AC-DC standard [18].

In our adopted design, the normal radial resistors are replaced by two radial resistors producing three output values as explained before which gaining benefit of getting three output voltages of 300 mV, 400 mV, and 171.4 mV by a very simple circuit. In this design, more advanced variable resistors were used instead of the resistors used in the single range μpot. This type of resistors are called multi-turn presets resistor. It is mostly used where very precise adjustments must be made through its screw. Its screw is turned to give very fine adjustment control of the resistor required value. The multi-turn presets resistors are miniature versions of the standard variable resistor. They are designed to be mounted directly onto the circuit board and adjusted only when the circuit is built.

Moreover a new software using LabVIEW program is prepared to measure δ of the μpot and calculate the uncertainties of the results.

3. Setup of the Whole Automated System

In metrological and industrial laboratories, programmable instruments are now widely employed and increasingly included in measurement systems, because they can perform automatically the time consuming operations required in the calibration activity. Accordingly, there is an effective request for software able to calibrate such instruments [19]. However, building automatic systems for calibration is not straightforward, especially for application in metrological laboratories that operate at high level of accuracy. For this reason, a special programmable measurement system has been built.

As shown in **Figure 2** the automated calibration system of the multiple output μpot consists of a highly accurate (FLUKE 5720), programmable calibrator, used as a precise source for both alternating and direct currents, SJTC multiple output μpot with three output ranges, highly sensitive digital multimeter (DMM) with a very high input resistance (10 GΩ) and 10 nV DC resolution (HP 3458A) to measure the output emf of the multiple output μpot at each range of the three ranges. Moreover, the (HP 3458A) DMM implements a reasonable digital method for the measurement of DC and AC voltages [20]. Finally, a personal computer (PC) is used to drive the calibrator and to record the DMM readings by using the specially designed LabVIEW program.

All the necessary precautions were accomplished in order to attain the optimum performance of the measuring circuit. Technical considerations were also given to fulfill correct grounding connections in this type of measurement and to avoid any interference from high field strength [15,16].

4. Experimental Work

Throughout the experimental work, the DC and AC currents had been applied to the μpot. The DMM then precisely recorded the output emf of the μpot through a specific LabVIEW command. The software was controlled to send the gathering results to the computer to be saved in a prepared excel worksheet. Indeed, the selected current combined with the appropriate frequency for each range was software processed.

Figure 2. Automated system of the multiple output μpot.

The nominal current (5 mA) was applied to each range of the multiple output μpot in the sequence (AC, DC^+, DC^-, AC) at approximately equal time intervals to readily eliminate the DC reversal error [21].

Sufficient time had been allowed after each current change for the SJTC to reach its final emf value [22]. After completing these four steps, the AC-DC difference (δ) was evaluated at each frequency from the following relation [15]:

$$\delta = \frac{E_{AC} - E_{DC}}{n \cdot E_{DC}} \quad (1)$$

where, E_{AC} is the average output emf due to the AC current. While, E_{DC} is the mean emf value due to the forward (DC^+) and the reverse (DC^-) currents and n is a dimensionless characteristics [21]. In fact, n is a necessary factor in the equation due to the square law response of the thermal converters. It approximately equals "2" (≈ 1.6 to 2) at rated heater current [22].

At the beginning of the test the value of n must firstly be determined. It was measured using the change in the output emf, ΔE, when the nominal input current is varied by ΔI according to the following relation [23]:

$$n = \frac{\Delta E / E}{\Delta I / I} \quad (2)$$

where,

I, is the nominal rated DC current (5 mA).

E, is the output emf corresponding to the nominal rated DC current.

ΔE, is the change in the output emf due to small changes in the applied current, ΔI.

Noting that, ΔI, had been programmed to be ± 0.5 percent of the nominal rated current, and the final AC-DC difference resulted at each frequency was the average of 30 determinations of AC-DC difference under the same measurement conditions.

The determined values of δ at different frequencies were then added to the calibrated value of the applied DC current with 5 mA nominal value to calculate the actual values of the input AC current by using the following equation:

$$I_{ac} = I_{dc}(1+\delta) \quad (3)$$

Afterwards, by applying the actual values of the AC current the actual values of the AC output voltage of each range of the multiple output μpot at each frequency could be obtained.

Furthermore, to get convincing evidence that the multiple output μpot performs as expected, the uncertainty budget was thoroughly estimated. The uncertainty is defined as the range of error of a measurement within which the true value of the measurand is estimated to lie within a stated level of confidence [16]. Type A and Type B evaluations are the two approaches to estimate

the uncertainty sources.

For AC-DC measurements, the Type B uncertainties are generally dominating [23]. Type A evaluations of standard uncertainty components are founded on normal distributions, while type B evaluations are founded on a suitable chosen distributions.

The combined standard uncertainty equals to the Root Sum Square (RSS), of all the uncertainty contributions [16,24]. All components of the combined standard uncertainty (Type A, Type B) were taken into consideration. The expanded uncertainties of the multiple output µpot were calculated with confidence level of 95% (coverage factor K = 2).

5. Results and Discussion

The results obtained at the rated current for *n* of each voltage range were 1.69, 1.72, and 1.73 for the 300 mV, the 400 mV and the 171.4 mV output AC voltage respectively. Also, the AC-DC differences for the three ranges of the µpot had been fully investigated. They are presented in **Table 1** and **Figure 3**. The plots illustrate the AC-DC differences of the 300 mV, 400 mV, and 171.4 mV ranges at frequencies from 10 Hz to 10 KHz in part per million (ppm).

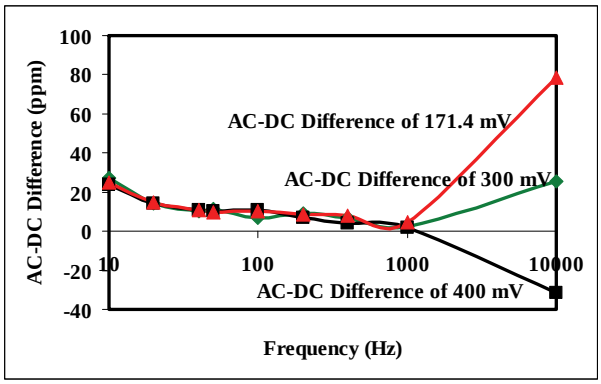

Figure 3. AC-DC difference of the 300 mV, 400 mV, 171.4 mV ranges (ppm).

It is cleared that, the AC-DC differences for the three output ranges of the multiple output µpot are fairly small at frequencies from 10 Hz to 10 KHz, as it is known that µpots can be used to generate AC voltage signals in millivolt ranges from 10 Hz to 1 MHz with AC-DC differences ranging from 20 ppm to 1000 ppm [25].

The gained results show that from 20 Hz to 1 KHz the multiple output µpot has a very stable output where the AC-DC differences are much smaller than the lower limit of the admitted AC-DC differences range.

Although, at 10 Hz and 10 KHz the AC-DC differences are relatively high, they are still very near to the lower limit. However, rather different but not highly effective behavior appeared at the 10 KHz for the 400 mV output where it shows a negative sign with its δ. This is most probably due to some dielectric losses inherent in the resistors.

Also, the δ of the 171.4 mV output at 10 KHz is relatively high due to factors contribute to frequency and voltage dependant errors. In fact this needs more careful investigation to reach the optimum design performance.

Nevertheless, the AC-DC differences of our developed multiple output µpot faithfully prove to be highly successful.

Tables 2-4 illustrate all the components of the uncertainty budget for the multiple output µpot three ranges respectively.

The AC input currents, and AC output voltages for the three voltage ranges at 10 Hz to 10 KHz combined with the corresponding expanded uncertainties are listed in **Tables 5-7**.

It is clearly shown from the tables that, the expanded uncertainties of the multiple output µpot proved to be less than 5 ppm for all values. This presents that the output voltages of the multiple output µpot are very satisfactory.

6. Conclusions

It is fairly demonstrated that our new design provides a

Table 1. Results of the AC-DC differences of the 300 mV, 400 mV, and 171.4 mV ranges at different frequencies.

Frequency (Hz)	δ (300 mV Range) (ppm)	δ (400 mV Range) (ppm)	δ (171.4 mV Range) (ppm)
10	27	24	25
20	14.2	14	14.6
40	10.2	11	11
50	11.3	10	9.7
100	6.6	11	10
200	9.3	7	8.8
400	6.8	4	7.8
1000	2.2	2	4.4
10000	25.6	–31.5	78.7

Table 2. Uncertainty budget of the 300 mV range calibration in (ppm).

Sources of Uncertainty	Type of Uncertainty	Uncertainty Value (ppm)	
Repeatability of o/p DC current	(Type A)	0.2	
U-Calibrator calibration certificate	(Type B)	1.3	
U-DMM calibration certificate	(Type B)	3.0	
U-Cables thermal emf	(Type B)	2.9	
Repeatability of δ	(Type A)	Freq. (Hz)	Value (ppm)
		10	0.4
		20	0.5
		40	0.5
		50	0.6
		100	0.6
		200	0.6
		400	0.6
		1000	0.6
		10000	0.5
Repeatability of AC Output Voltage	(Type A)	Freq. (Hz)	Value (ppm)
		10	2
		20	2.2
		40	1.2
		50	1.4
		100	1.3
		200	1.1
		400	1.2
		1000	1.4
		10000	0.8

Table 3. Uncertainty budget of the 400 mV range calibration in (ppm).

Sources of Uncertainty	Type of Uncertainty	Uncertainty Value (ppm)	
Repeatability of o/p DC current	(Type A)	0.2	
U-Calibrator calibration certificate	(Type B)	1.3	
U-DMM calibration certificate	(Type B)	3.0	
U-Cables thermal emf	(Type B)	2.9	
Repeatability of δ	(Type A)	Freq. (Hz)	Value (ppm)
		10	0.8
		20	0.4
		40	0.4
		50	0.5
		100	0.4
		200	0.3
		400	0.4
		1000	0.6
		10000	0.5
Repeatability of AC Output Voltage	(Type A)	Freq. (Hz)	Value (ppm)
		10	1.7
		20	1.4
		40	1.2
		50	1.6
		100	1.1
		200	0.6
		400	1.3
		1000	1.6
		10000	0.9

Table 4. Uncertainty budget of the 171.4 mV range calibration in (ppm).

Sources of Uncertainty	Type of Uncertainty	Uncertainty Value (ppm)	
Repeatability of o/p DC current	(Type A)	0.2	
U-Calibrator calibration certificate	(Type B)	1.3	
U-DMM calibration certificate	(Type B)	3.0	
U-Cables thermal emf	(Type B)	2.9	
		Freq. (Hz)	Value (ppm)
Repeatability of δ	(Type A)	10	0.8
		20	0.4
		40	0.4
		50	0.4
		100	0.4
		200	0.3
		400	0.4
		1000	0.4
		10000	0.7
		Freq. (Hz)	Value (ppm)
Repeatability of AC Output Voltage	(Type A)	10	0.9
		20	0.6
		40	0.6
		50	2.1
		100	0.6
		200	0.8
		400	0.9
		1000	0.5
		10000	0.4

Table 5. AC input currents and AC output voltages combined with the expanded uncertainties of the 300 mV μpot.

Freq. (Hz)	I_{AC} (mA)	V_{AC} (mV)	± Expanded Uncertainty (ppm)
10	5.0006822	299.85727	4.8
20	5.0003622	299.64441	4.9
40	5.0002622	299.85719	4.6
50	5.0002897	299.82553	4.6
100	5.0001722	299.85764	4.6
200	5.0002397	299.82329	4.5
400	5.0001772	299.81784	4.6
1000	5.0000622	299.81959	4.6
10000	5.0006472	299.87278	4.5

Table 6. AC input currents and AC output voltages combined with the expanded uncertainties of the 400 mV μpot.

Freq. (Hz)	I_{AC} (mA)	V_{AC} (mV)	± Expanded Uncertainty (ppm)
10	5.0006072	399.63049	4.8
20	5.0003572	399.79723	4.6
40	5.0002822	399.78593	4.6
50	5.0002572	399.78323	4.7
100	5.0002822	399.82343	4.5
200	5.0001822	399.78184	4.4
400	5.0001072	399.78409	4.6
1000	5.0000572	399.63214	4.7
10000	4.9992197	399.53989	4.5

Table 7. AC input currents and AC output voltages combined with the expanded uncertainties of the 171.4 mV μpot.

Freq. (Hz)	I_{AC} (mA)	V_{AC} (mV)	± Expanded Uncertainty (ppm)
10	5.0006322	171.38202	4.8
20	5.0003722	171.51913	4.6
40	5.0002822	171.58246	4.6
50	5.0002497	171.56305	4.7
100	5.0002572	171.58934	4.5
200	5.0002272	171.59201	4.4
400	5.0002022	171.56805	4.6
1000	5.0001172	171.56316	4.7
10000	5.0019747	171.61028	4.5

significantly stable AC voltage source in millivolt ranges. The combination of the microcontroller and the radial resistors with the SJTC offers three highly stable output AC voltages, 300 mV, 400 mV, and their parallel combination, 171.4 mV, from the same outlet. Experiments with the prototype indicate that its AC-DC differences for the three output AC voltage ranges are faithfully small.

In actual fact, it is expected that the adopted circuit will be a very good supplement or even may replace other commercial standards AC voltage sources due to its extreme simplicity, its very low cost and its excellent portability besides its admirable accuracy. In addition, this device is readily suitable for many other applications. However, further improvement can be achieved in the final product in the near future.

7. References

[1] U. Pogliano, G. C. Bosco and M. Lanzillotti, "Precision Measurement of AC Voltages in the Millivolt Ranges," *Proceedings of XVII IMEKO World Congress*, 22-27 June 2003, Dubrovnik, pp. 625-629.

[2] J. Zinkernagel, "A Low-Voltage and High-Frequency ac-dc Transfer System Using Inductive Dividers," *IEEE Transactions on Instrumentation and Measurement*, Vol. 43, No. 4, August 1994, pp. 544-548.

[3] U. Pogliano, B. Trinchera and F. Francone, "Reconfigurable Unit for Precise RMS Measurements," *IEEE Transactions on Instrumentation and Measurement*, Vol. 58, No. 4, April 2009, pp. 827-831.

[4] I. Budovsky and B. D. Inglis, "High-Frequency AC-DC Differences of NML Single-Junction Thermal Voltage Converters," *Institute of Measurement, IEEE Transactions on Instrumentation and Measurement*, Vol. 50, No 1, February 2001, pp. 101-105.

[5] H. Laiz and M. Klonz, "A Simulation Tool for the AC-DC Transfer Difference of Thermal Converters at Low Frequencies," *IEEE Transactions on Instrumentation and Measurement*, Vol. 48, No. 6, December 1999, pp. 1155-1160.

[6] H. Fujiki, "New Thin-Film Multijunction Thermal Converter Design for Improved High-Frequency Performance," *IEEE Transactions on Instrumentation and Measurement*, Vol. 7, No. 9, September 2007, pp. 1243-1247.

[7] M. Klonz, Laiz and E. Kessler, "Development of Thin-Film Multijunction Thermal Converters at PTB/IPHT," *IEEE Transactions on Instrumentation and Measurement*, Vol. 50, No. 6, December 2001, pp. 1490-1498.

[8] M. Klonz, H. Laiz, T. Spiegel and P. Bittel, "AC-DC Current Transfer Step-Up and Step-Down Calibration and Uncertainty Calculation," *IEEE Transactions on Instrumentation and Measurement*, Vol. 51, No. 5, October 2002, pp. 1027-1034.

[9] H. Dintners, M. Klonz, A. Lerm, F. VBlklein and T. Weimann, "AC-DC-mV-Transfer with Highly Sensitive Thin-Film Multijunction Thermal Converters," *IEEE Transactions on Instrumentation and Measurement*, Vol. IM-42, April 1993, pp. 612-614.

[10] I. Budovsky, "A Micropotentiometer-Based System for Low-Voltage Calibration of Alternating Voltage Measurement Standards," *IEEE Transactions on Instrumentation and Measurement*, Vol. 46, No. 2, April 1997, pp. 356-360.

[11] T. Funck, M. Stojanovi´c and M. Klonz, "Improved High-Input-Impedance mV-Amplifiers with Gain Factors from 10 to 900," *IEEE Transactions on Instrumentation and Measurement*, Vol. 58, No. 4, April 2009, pp. 859-862.

[12] J. R. Kinard, D. X. Huang and D. B. Novotny, "Integrated Thin-Film Micropotentiometers," *IEEE Transactions on Instrumentation and Measurement*, Vol. IM-44, April 1995, pp. 374-376.

[13] H. A. Mageed, M. Halawa, A. F. Zobaa and M. M. Abdel Aziz, "Establishment and Characterization of a Traceable AC Voltage Source at NIS, Egypt," *Universities Power Engineering Conference*, Padova, September 2008.

[14] www.atmel.com/atmel/acrobat/doc0368.pdf

[15] D. X. Huang, G. Rebuldela and J. D. Harper, "RF-DC Differences of Micropotentiometers," *IEEE Transactions on Instrumentation and Measurement*, Vol. 46, No. 2, April 1997, pp. 337-341.

[16] Fluke Corporation, "Calibration: Philosophy in Practice,"

2nd Edition, Legal Department, Everett, WA 98206-9090, May 1994.

[17] P. S. Filipski and M. Boecker, "AC-DC Current Transfer Standards and Calibrations at NRC," *Symposium of Metrology*, Mexico, October 2006.

[18] U. Pogliano and G. C. Bosco, "Determination of the Frequency Dependence of the AC-DC Voltage Standard at IEN," *IEEE Transactions on Instrumentation and Measurement*, Vol. 46, No. 2, April 1997, pp. 373-376.

[19] U. Pogliano, G. C. Bosco and M. Lanzillotti, "Generalized Automatic System for AC/DC Transfer, AC Voltage, and AC Current Measurements," *IEEE Transactions on Instrumentation and Measurement*, Vol. 55, No. 5, October 2006, pp. 1747-1751.

[20] C. D. Capua, D. Grillo and E. Romeo, "The Implementation of an Automatic Measurement Station for the Determination of the Calibration Intervals for a DMM," *IEEE International Conference on Virtual Environments, Human Computer Interfaces and Measurement Systems*, La Coruna-Spain, 10-12 July 2006, pp. 58-62.

[21] B. Stojanovic, M. Klonz, H. Laiz and S. Kraicanic, "AC-DC Voltage Transfer Module with Thin-Film Multijunction Thermal Converter," *IEEE Transactions on Instrumentation and Measurement*, Vol. 52, No. 2, April 2003, pp. 355-358.

[22] T. E. Lipe, "Operation and Reference Manual for the NIST Automated AC-DC Calibration Systems and Software," NIST Special Publication, May 2004.

[23] "The Expression of Uncertainty and Confidence in Measurement," United Kingdom Accreditation Service, NAMAS, M 3003, 1st Edition, January 2007.

[24] "Guide to the Expression of Uncertainty in Measurement," Saudi Arabian Standards Organization, 2006.

[25] D. X. Huang, J. Harper and D. Mcadoo, "Measurement Assurance of RF-DC Differences of Thermal Standards," *NCSL Workshop & Symposium*, 1996.

Energy and Power Engineering, **2010, 2, 111-121**
doi:10.4236/epe.2010.22016 Published Online May 2010 (http://www. SciRP.org/journal/epe)

Sequential Approach with Matrix Framework for Various Types of Economic Thermal Power Dispatch Problems

Subramanian Srikrishna, Ganesan Sivarajan
Department of Electrical Engineering, FEAT, Annamalai University, Annamalainagar, India
E-mail: *dr_smani@yahoo.co.in, ganeshshriraj@gmail.com*
Received January 22, 2010; *revised February* 25, 2010; *accepted March* 24, 2010

Abstract

This paper presents a sequential approach with matrix framework for solving various kinds of economic dispatch problems. The objective of the economic dispatch problems of electrical power generation is to schedule the committed generating units output so as to meet the required load demand while satisfying the system equality and inequality constraints. This is a maiden approach developed to obtain the optimal dispatches of generating units for all possible load demands of power system in a single execution. The feasibility of the proposed method is demonstrated by solving economic load dispatch problem, combined economic and emission dispatch problem, multiarea economic dispatch problem and economic dispatch problem with multiple fuel options. The proposed methodology is tested with different scale of power systems. The generating unit operational constraints are also considered. The simulation results obtained by proposed methodology for various economic dispatch problems are compared with previous literatures in terms of solution quality. Numerical simulation results indicate an improvement in total cost saving and hence the superiority of the proposed method is also revealed for economic dispatch problems.

Keywords: Combined Economic and Emission Dispatch, Composite Cost Function, Economic Dispatch, Multiarea Economic Dispatch, Multiple Fuel Options, Prohibited Operating Zone, Ramp Rate Limits, Sequential Approach, Transmission Loss

1. Introduction

The primary objective of the economic dispatch problem is to schedule the generations of thermal units so as to meet the required load demand at minimum operating cost while satisfying the individual and system operating constraints. Traditionally, the cost function for generating units has been approximated as a quadratic function. A variety of optimization techniques has been used for solving economic dispatch problems. The conventional methods include traditional lambda-iteration method, the base point and participation factors method, and the gradient methods are suggested to solve economic dispatch problems [1,2]. The applications of classical methods, such as linear or quadratic programming are also applied for solving economic dispatch problems [3,4].

The methods based on operational research and artificial intelligence concepts such as genetic algorithm, evolutionary algorithms, fuzzy and artificial neural networks have been given attention for solving economic dispatch problems because of their ability to find the solution near global optimal. Simulated Annealing technique (SA) and Genetic Algorithm (GA) have been applied to determine the optimal generation schedule for economic dispatch problem in a power system [5,6]. Artificial neural network based models are developed for the solution of economic power dispatch problem [7,8]. Particle Swarm Optimization method (PSO) has been applied for solving economic dispatch problems with various operating constraints like prohibited operating zones and ramp rate limits [9,10]. Evolutionary strategy based algorithm is suggested for solving economic dispatch problem [11]. A partition approach based solution for economic dispatch problems considering the physical limitations of the system is presented [12]. An enhanced Hopfield neural network model is developed to solve economic dispatch problems [13]. The heuristic search techniques such as Differential Evolution (DE), Chaotic and ant swarm optimization algorithm and Direct Search GA (DSGA) have been applied to solve economic dispatch problems [14-17]. Hybrid approaches including SA-PSO and Bacterial foraging-Nelder Mead method have also been developed to obtain the dispatches of generating units [18,19].

Due to environmental concerns, Combined Economic and Emission Dispatch (CEED) problem has been formulated to determine the optimal amount of generated power for the generating units in the system by minimizing the fuel cost and emission level simultaneously subject to various system constraints. The passage of clean air act amendments in 1990 has forced utilities to reduce their SO_2 and NOx emissions since both are the primary power plant emissions [20]. A general formulation based on the Lagrange relaxation method is presented for solving environmental constrained economic dispatch problem [21]. Lamount and Qbesses detailed various emission dispatching strategies and solution procedure based on emission shadow prices [22]. Srikrishna and Palanichamy suggested price penalty factor to convert bi objective function into a single objective function [23]. Fuzzy logic and neural network models are developed for solving this multiobjective optimization problem [24-28]. The heuristic search methods are applied to solve this problem [29,30]. Quadratic Programming (QP) method based solution for this multi objective problem is presented [31].

Dynamic programming recursive approach is developed for solving emission constrained economic dispatch problem [32]. L. Wang and C. Singh investigated to solve this problem by applying a fuzzified multi objective particle swarm optimization algorithm [33]. An approach based on constrained pattern search method is presented to solve this problem [34]. Simplified recursive approach is presented for the solution of this multiobjective optimization problem [35]. The authors developed a generalized equation to find the optimal generations of units. Palanichamy and Sundar Babu developed direct method for solving this type of problems based on mathematical modeling [36]. Artificial neural network (ANN), Fuzzy logic based models and heuristic search techniques are used for solving this multiobjective problem [37-40].

The economic dispatch problem of a power system is extended to take into consideration of additional necessary constraints such as transmission capacity limits to ensure security of the system. Direct Search Method (DSM) and ANN models have been suggested for solving the multi area economic dispatch problem [41,42].

In certain fossil fired generating units use different fuels hence the cost function are represented as a segmented piecewise quadratic function. This problem faces with the problem of identification of the most economical fuel of each unit. Lin and Viviani reported Hierarchical Method [HM] to solve the economic dispatch problem with piecewise quadratic functions [43]. Artificial neural network models and heuristic search techniques are used for solve this problem [44-48].

In this article, simplified methodology is presented for solving economic dispatch problems namely, large scale economic dispatch, economic dispatch with operational constraints, combined economic and emission dispatch, multi area economic dispatch and economic dispatch with multiple fuel options. The proposed approach is demonstrated with suitable test systems.

2. Problem Formulation

The problem formulation for economic dispatch, combined economic and emission dispatch, multiarea economic dispatch and economic dispatch with multiple fuel options are described as follows.

2.1. Economic Dispatch (ED) Problem with Generator Operating Constraints

The objective of economic dispatch is to simultaneously minimize the generation cost rate and to meet the load demand of a power system over some appropriate period while satisfying various operating constraints. The objective function of an economic dispatch problem can be formulated as,

$$min\, F_T = \sum_{i=1}^{n} F_i(P_i) = \sum_{i=1}^{n} a_i P_i^2 + b_i P_i + c_i \qquad (1)$$

Constraints

1) *Power balance constraint*

$$\sum_{i=1}^{n} P_i = P_G = P_D + P_L \qquad (2)$$

The transmission loss can be expressed as,

$$P_L = \sum_{i=1}^{n}\sum_{j=1}^{n} P_i B_{ij} P_j + \sum_{i=1}^{n} B_{0i} P_i + B_{00} \qquad (3)$$

or approximately

$$P_L = \sum_{i=1}^{n}\sum_{j=1}^{n} P_i B_{ij} P_j \qquad (4)$$

2) *Generator operational constraints*

a. Generator capacity constraint

$$P_{i,min} \le P_i \le P_{i,max} \qquad (5)$$

b. Ramp rate limits

The inequality constraints due to ramp rate limits for unit generation changes are given

1) as generation increases

$$P_i - P_i^0 \le UR_i \qquad (6)$$

2) as generation decreases

$$P_i - P_i^0 \le DR_i \qquad (7)$$

The generator operation constraint after including ramp rate limit of generators can be described as,

$$max(P_{i,min}, P_i^0 - DR_i) \le P_i \le min(P_{i,max}, P_i^0 + UR_i) \qquad (8)$$

c. Prohibited operating zone constraint

The feasible operating zones of unit *i* can be described as follows,

$$P_{i,min} \le P_i \le P_{i,1}^l$$

$$P_{i,j-1}^u \le P_i \le P_{i,j}^l, \quad j = 2,3,....,n_i \tag{9}$$

$$P_{i,n_i}^u \le P_i \le P_{i,max}$$

2.2. Combined Economic and Emission Dispatch (CEED) Problem

This problem is formulated by including the reduction of emission as an objective. Like the fuel cost function given in (1), the total emission of generation E_T (kg/h) can be expressed by a quadratic function of generation as,

$$E_T = \sum_{i=1}^{n} (d_i P_i^2 + e_i P_i + f_i) \tag{10}$$

A multi-objective optimization problem is converted in to a single objective optimization problem by introducing price penalty factor h as follows,

$$F_T = \sum_{i=1}^{n} (a_i P_i^2 + b_i P_i + c_i) + h_i (d_i P_i^2 + e_i P_i + f_i) \tag{11}$$

and this objective function has to satisfy the power balance constraint and the generation capacity constraints. The price penalty factor that coordinates the emission with the normal fuel cost.

2.3. Multi Area Economic Dispatch (MAED) Problem

The objective of multi area economic dispatch is to determine the generation levels and the interchange power between areas that minimize the system operation cost while satisfying a set of constraints as,

$$min \sum_{m=1}^{M} F_m = min \sum_{m=1}^{M} \sum_{n=1}^{N_m} (a_{mn} P_{mn}^2 + b_{mn} P_{mn} + c_{mn}) \tag{12}$$

Subject to

1) Area power balance constraint

$$\sum_{m=1}^{N_m} P_{mn} + \sum_{j \in \beta_m} t_{kj} - \sum_{j \in \beta_m} t_{jk} - P_{DM} = 0 \tag{13}$$

2) Generation limits constraint

$$P_{mn,min} \le P_{mn} \le P_{mn,max} \tag{14}$$

3) Tie line limits constraint

$$t_{jk,min} \le t_{jk} \le t_{jk,max} \tag{15}$$

2.4. Economic Dispatch Problem with Multiple Fuel Options (EDMFO)

In economic dispatch problem, the fuel cost of each generator is represented by a single quadratic cost function. Owing to multiple fuel options, the cost function may become piecewise quadratic. Hence, the economic dispatch problem with piecewise quadratic function is defined as,

$$min \sum_{j=1}^{N} F_j (P_j) \tag{16}$$

where,

$$F_j (P_j) = \begin{cases} a_{j1} P_j^2 + b_{j1} P_j + c_{j1}, fuel\,1, P_{j,min} \le P_j \le P_{j1} \\ a_{j2} P_j^2 + b_{j2} P_j + c_{j2}, fuel\,2, P_{j1} \le P_j \le P_{j2} \\ . \\ a_{jm} P_j^2 + b_{jm} P_j + c_{jm}, fuel\,m, P_{j,m-1} \le P_j \le P_{j,max} \end{cases} \tag{17}$$

This objective function is minimized subject to power balance constraint.

3. Solution Methodology

3.1. Demonstration of Sequential Approach with Matrix Framework

Sequential approach with matrix framework is proposed for solving economic dispatch problems. This is the first method developed to obtain the optimal dispatches for all possible load demands in a system. The demonstration of the solution methodology is presented in this section.

The electric power production in a power plant is allowed to vary from minimum technical limit (P_{min}) to maximum technical limit (P_{max}). Initially the $P_{i,min}$ of all generating units in a power plant are considered as initial state input values and is represented by a single dimensional matrix as,

$$s = [P_{1,min} \;\; P_{2,min} \;\; P_{3,min} \;\; ,....., \;\; P_{n,min}] \tag{18}$$

Based on the above single dimensional matrix, a square matrix (I) is developed to identify the economic schedule of generation. The formation of the square matrix is as follows. The process starts with a step increment in generation by Δ MW in $P_{1,min}$ by keeping the remaining units at its input value. This will form first row of the square matrix.

$$I_1 = [P_{1,min} + \Delta \;\; P_{2,min} \;\; P_{3,min} \;\; ,....., \;\; P_{n,min}] \tag{19}$$

The increment in generation is made in the second element by keeping the other elements at its input value that leads to the development of second row of the square matrix.

$$I_2 = [\,P_{1,min} \;\; P_{2,min} + \Delta \;\; P_{3,min} \,, \ldots\ldots, \, P_{n,min}\,] \qquad (20)$$

In the same logic, an increment is made for remaining units one at a time and a square matrix with a dimension equal to the number of units has been developed. For every step increment in the operating range of the plant the unit one at a time is allowed to experience the change in generation thus leads to the formation of the square matrix.

$$I = \begin{bmatrix} I_1 \\ I_2 \\ . \\ I_n \end{bmatrix} = \begin{bmatrix} P_{1,min} + \Delta & P_{2,min} & \ldots & P_{n,min} \\ P_{1,min} & P_{2,min} + \Delta & \ldots & P_{n,min} \\ . & . & . & . \\ P_{1,min} & P_{2,min} & \ldots & P_{n,min} + \Delta \end{bmatrix} \qquad (21)$$

Each element in the square matrix represents the generation of a unit corresponding to the column that should satisfy the unit capacity constraints. In addition, the operational constraints such as ramp rate limits and prohibited operating zones are also enforced. The operating regions of the unit after including ramp rate limits are identified as mentioned in Equation (8). The operating regions of the units having prohibited operating zones are separated into isolated sub regions and it is identified using Equation (9). The operating regions of the units having prohibited operating zones and ramp rate constraints are obtained as mentioned earlier. The units are allowed to operate in the one of the operating zones. If the generation of a unit falls in a prohibited operating zone, the feasible optimal level would most likely to be located in any one of the adjacent feasible operating regions, that is, the operating region above or below the prohibited operating zone.

In the square matrix the unit generations of each row that satisfy the constraints are identified and total fuel cost of generation is evaluated. The desired economic schedule of generation is identified by analyzing fitness of each row. The fitness function of each row is calculated as,

$$fit(j) = \frac{F_T(j)}{(pd + \Delta)} \quad j = 1,2,\ldots n \qquad (22)$$

where, pd is the total of input values.

The schedule with the minimum fitness is chosen as the successive state input values. This process is repeated till all the generating units reach their maximum generation capacity. The feasible solutions for every increment from P_{min} to P_{max} are obtained and hence the best solution for any load demand falls in the operating boundary can be easily sited.

In practical applications, the total generation must be equal to the power demand and transmission loss. In such cases, the power balance constraint is exactly met by calculating the diagonal unit generation as follows.

$$P_{i,i} = (pd + \Delta) + P_L - \sum_{\substack{j=1 \\ j \neq i}}^{n} P_{i,j} \qquad i = 1,2,\ldots,n \qquad (23)$$

The detailed computational flow of the proposed method is presented in **Figure 1**. The proposed methodology in the form of matrix framework to support the demonstration is as follows.

Initial Stage

$$\left.\begin{bmatrix} P_{1,min} + \Delta & P_{2,min} & . & P_{n,min} \\ P_{1,min} & P_{2,min} + \Delta & . & P_{n,min} \\ . & . & . & . \\ P_{1,min} & P_{2,min} & . & P_{n,min} + \Delta \end{bmatrix} \begin{matrix} \Rightarrow fit(1) \\ \Rightarrow fit(2) \\ \\ \Rightarrow fit(n) \end{matrix} \right\} \begin{matrix} Choose \\ min\,(fit) \end{matrix}$$

$$\Downarrow$$

Final Stage

$$\left.\begin{bmatrix} P_{1,max} - \Delta & P_{2,max} & . & P_{n,max} \\ P_{1,max} & P_{2,max} - \Delta & . & P_{n,max} \\ . & . & . & . \\ P_{1,max} & P_{2,max} & . & P_{n,max} - \Delta \end{bmatrix} \begin{matrix} \Rightarrow fit(1) \\ \Rightarrow fit(2) \\ \\ \Rightarrow fit(n) \end{matrix} \right\} \begin{matrix} Choose \\ min\,(fit) \end{matrix}$$

4. Simulations Results and Discussions

A simplified methodology based on sequential approach with matrix framework is developed for solving different kinds of economic dispatch problems. The effectiveness of this approach is tested for solving various kinds of economic dispatch problems including combined economic and emission dispatch problem, multi area economic dispatch problem and economic dispatch with multiple fuel options.

The algorithm for solving the examples were implemented in Matlab 7.0 platform and executed with Pentium IV, 2.8 GHz personal computer. The proposed methodology provides the optimal schedule of generations for all possible load demands which is varied from minimum technical limit by a small increment to maximum technical limit of the system. The selection of increment is also an important factor. Too large increment may end up with unfeasible solution and too small increment may take long execution time. Based on experience, the desired increment is chosen as 1 MW.

4.1. Case A: Economic Dispatch (ED) Problem with Generator Operating Constraints

The objective is the minimization of total fuel cost subject to power balance and generator operational constraints. The effectiveness and efficiency of the developed approach is tested with large scale economic dis-

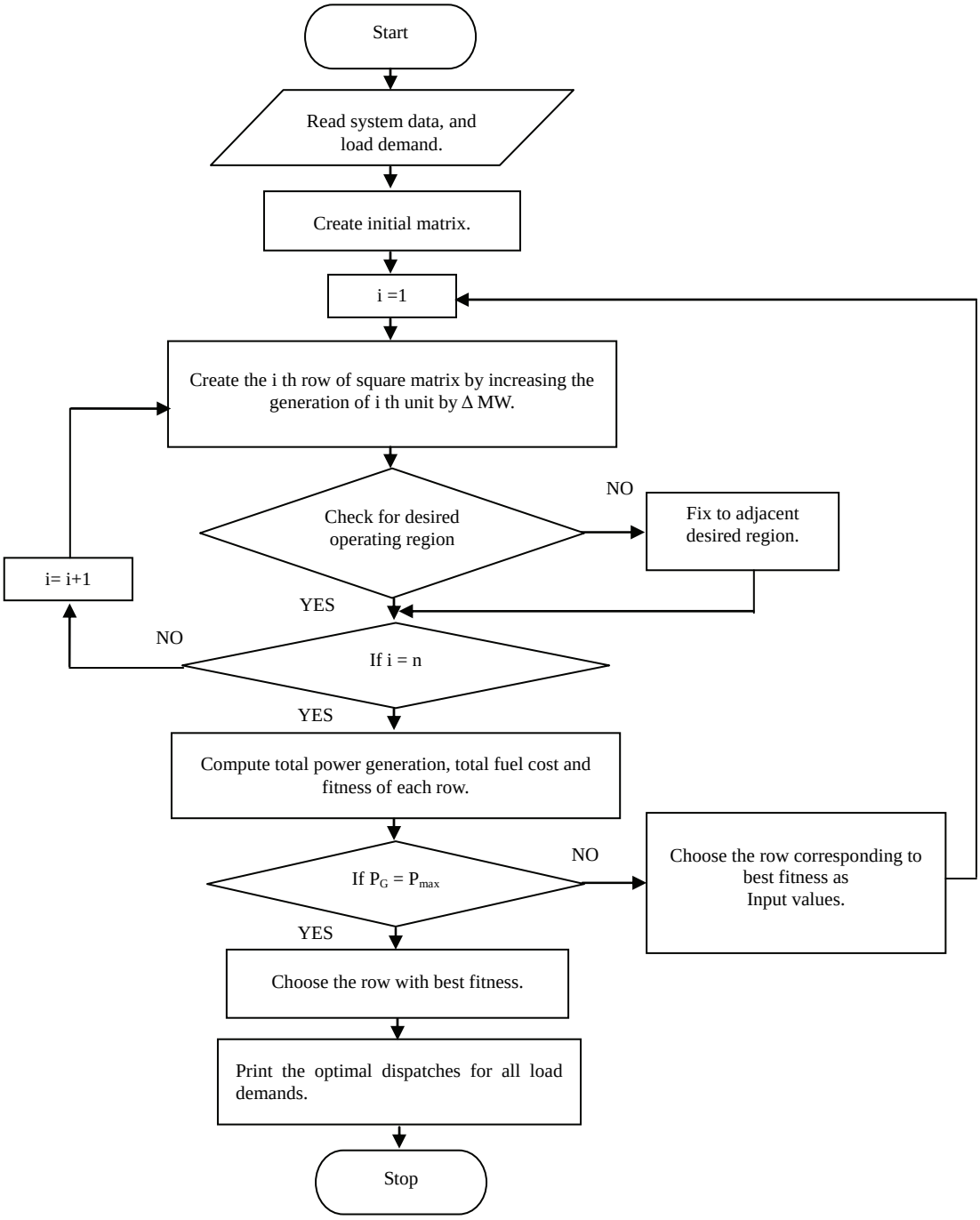

Figure 1. Computational flow of proposed method.

patch problem and economic dispatch problem with generator operational constraints. The 40 unit and 15 unit sample systems are considered for the case studies.

The first sample system consists of forty units in the realistic Taipower system that is a large scale and mixed -generating system where coal-fired, oil-fired, gas-fired, diesel and combined cycle are present. The cost coefficients and maximum and minimum generation limits of the sample system are available in literature [15]. The simulation results for load demands of 9000 MW, 9500 MW and 10500 MW are compared with Simulated Annealing (SA) [15], Genetic Algorithm (GA) [15], Hybrid Differential Evolution (HDE) [15], Variable Scaling Hybrid Differential Evolution (VSHDE) [15] and Direct Search Genetic Algorithm (DSGA) [17] and the comparison of results are presented in **Table 1**. As seen from comparison, the proposed method provides the minimum generation cost for above mentioned load demands. It

Table 1. Total fuel cost ($/h) comparison of 40 unit system.

Method	Load demand		
	9000 MW	9500 MW	10500 MW
Proposed method	121039.18	128219.31	143721.71
VSHDE [15]	121253.01	---	143943.90
HDE [15]	121266.40	---	143955.83
GA [15]	121839.72	---	144486.02
SA [15]	135229.69	---	164069.36
DSGA [17]	---	128424.26	---

also clears that the proposed methodology is efficient to solve large scale economic dispatch problems.

The cost coefficients, maximum and minimum generation limits, ramp rate limits and prohibited operating zones and the transmission loss coefficients with a base capacity of 100 MVA of the fifteen unit sample system are reported in the literature [9]. The minimum and maximum technical limits of the system are 915 MW and 3542 MW respectively. The operating regions of the unit are identified after incorporating ramp rate limits and prohibited operating zone constraints. The transmission loss is calculated using transmission loss matrix or B coefficients. The power balance is exactly met by evaluating the generation using Equation (23). The generations of the units neglecting transmission loss are treated as input values for the successive state. The optimum generations of individual thermal units and total fuel cost for the load demand of 2630 MW are presented in **Table 2**. The simulation result is compared with GA [9], PSO [9], Modified PSO (MPSO) [18] and Adaptive Bacterial Foraging-Nelder Mead method (ABFNM) [19] and the comparison of results are presented in **Table 3**. It is clear from the comparison of results that the proposed method provides better schedule of generations to meet the load demand with existing techniques.

4.2. Case B: Combined Economic and Emission Dispatch (CEED) Problem

The objective of this multi objective optimization problem is to determine the optimal generations of thermal units by minimizing the total fuel cost and emission simultaneously subject to various system operating constraints. The price penalty factor multiobjective optimization problem can be converted into a single objective optimization problem. Various price penalty factors [23, 31,35] are suggested and among these maximum price penalty factor is chosen for combining cost of fuel plus the implied cost of emission as it offers a very good solution for emission restricted less cost condition [35]. In this article the maximum price penalty factor is considered. The maximum price penalty factor of each generator is the ratio between the fuel cost and emission at its maximum power output.

Table 2. Economic dispatch results for 15 unit system.

Unit	Output (MW)	Unit	Output (MW)	Unit	Output (MW)
1	**455.00**	6	**460.00**	11	**80.00**
2	**380.00**	7	**430.00**	12	**80.00**
3	**130.00**	8	**60.00**	13	**25.00**
4	**130.00**	9	**70.9033**	14	**15.00**
5	**170.00**	10	**159.00**	15	**15.00**
Load demand (MW)					**2630**
Transmission loss (MW)					**29.9033**
Total fuel cost ($/h)					**32696.81**

Table 3. Simulation results comparison for 15 unit system.

Method	Load demand 2630 W	
	Transmission loss (MW)	Total fuel cost ($/h)
Proposed method	**29.9033**	**32696.81**
ABFNM [19]	28.9470	32784.5024
MPSO [18]	30.908	32708
PSO [9]	32.431	32858
GA [9]	38.278	33113

$$h_{i,max} = \frac{(a_i P_{i,max}^2 + b_i P_{i,max} + c_i)}{(d_i P_{i,max}^2 + e_i P_{i,max} + f_i)} \quad (24)$$

The effectiveness of the proposed approach has been analyzed with 6 unit test system. The system details including cost coefficients, emission coefficients, minimum and maximum generation limits and transmission loss coefficients are given in [40]. The optimal dispatches are obtained for load demands vary from 345 MW to 1350 MW. The simulation results are compared with λ-iteration method [39], Quadratic Programming (QP) [31], Artificial Immune System (AIS) [39] and NSGA II-MADM [40] for a load demand of 700 MW. The comparison of total fuel cost, total emission and transmission loss is tabulated in **Table 4**. The comparison clearly indicates the significant reduction in fuel cost and transmission losses over earlier reports and the solution obtained by the proposed approach is close agreement with λ-iteration method.

For most of the load demands, the proposed method yields better results and they are in good agreement with the existing methods. The economic and environmental dispatch is conflicting multiobjective problem when the fuel cost increases the emission level decreases and hence in vice versa. As per the above statement, for some load conditions, there is a slight deviation in cost and emission with respect to the other existing methods.

4.3. Case C: Multi Area Economic Dispatch (MAED) Problem

The economic dispatch problem is extended to take into

Table 4. Simulation results comparison of six-generator system.

Method	Load demand 700 MW		
	Total fuel cost ($/h)	Total emission (kg/h)	Transmission loss (MW)
λ-iteration [39]	37781	442	21.17
QP [31]	37488	439.7	17.054
AIS [39]	37344	438.1	16.91
NSGA II-MADM [40]	38331.647	443.138	14.645
Proposed method	**37166.73**	**453.44**	**17.64**

considerations of transmission capacity limits to ensure the security of the system. A two area system with four thermal generating units is considered to illustrate the effectiveness of the proposed approach. The system data are available in the literature [41]. The total load demand in area 1 and area 2 are 70% and 30% of total load demand respectively and these two areas are interconnected through transmission lines. Each area consists of two generating units and for the sake of comparison with earlier reports transmission losses are not considered. The line flow limits of 90 MW, 120 MW and 200 MW are considered for the analysis. The optimum generations of individual units of each area for load demand of 1200 MW including transmission line limits are tabulated in **Table 5**.

The total generation of area 2 is greater than the total generation of area 1 that can export as much economical excess as power to area 1 to satisfy the requirement in area 1 without violating transmission line flow limits. The results obtained by this proposed methodology are

Table 5. Optimal generation results of two area system including transmission capacity constraints.

Load 1120 MW		Flow limit (MW)		
		90 MW	90 MW	90 MW
Optimal generation in area-1	P1 (MW)	**528**	**506**	**445**
	P2 (MW)	**166**	**158**	**139**
Optimal generation in area-2	P1 (MW)	**159**	**173**	**212**
	P2 (MW)	**267**	**283**	**324**
Total fuel cost ($/h)		**10700.80**	**10669.09**	**10604.68**

Table 6. Comparison of total fuel cost for MAED.

Load (MW)	Flow limit (MW)	Total generation cost ($/h)		
		EDSM [43]	NN [44]	Proposed method
800	90	7812.2	7812.2	**7811.94**
	120	7791.5	7791.5	**7791.25**
	200	7754.8	7754.8	**7754.70**
1030	90	9874.7	9874.7	**9874.20**
	120	9846.4	9846.4	**9846.01**
	200	9789.7	9789.7	**9789.42**
1120	90	10701	10701	**10700.80**
	120	10670	10670	**10669.09**
	200	10605	10605	**10604.68**

compared with Economic Dispatch Direct Search Method (EDSM) [41] and Neural Network (NN) [42] and the comparison of results are presented in **Table 6**.

4.4. Case D: Economic Dispatch Problem with Multiple Fuel Options (EDMFO)

The economic dispatch problem with multiple fuel options has been solved in two phases. In first phase, the most economic fuel of each generating unit is identified. The economic dispatch of generating units is determined by a sequential approach with the selected fuels in second phase. The implementation procedure of the proposed methodology has been detailed as follows.

The primary search process calculates the composite cost function of each generating unit and the detailed derivation of composite cost coefficients are presented in Appendix. Then sequential approach with matrix framework is performed to identify the most economic fuel of each unit. The composite function and capacity of the units are using for the above process. This phase provides the generation dispatches and the fuel corresponding to the dispatches is known as the most economic fuel. The generation limits corresponding to the selected fuel is the desired operating region of the unit. At the end of first phase, the most economic fuel and the desired operating region of each unit are obtained. In second phase, the generation dispatches of the units are refined within the desired operating regions. The cost functions of the selected fuels are considered and sequential approach with matrix framework is performed again to obtain the optimal dispatches of generating units.

The effectiveness of this proposed approach for solving this problem is tested with a sample system consists of ten generating units, each unit with two or three fuel options. The details of fuel options, cost coefficients and maximum and minimum generations of each fuel in each generating unit are available in the literature [43]. The simulation result for load demand of 2700 MW is de-

tailed in **Table 7**. The total fuel cost for load demands of 2500 MW, 2600 MW and 2700 MW obtained by this methodology, Hierarchical Method (HM) [43], Hopfield Neural Network (HNN) [44], Adaptive Hopfield Neural Network (AHNN) [45], Hybrid Genetic Algorithm (HGA) [46], Classical Evolutionary Programming (CEP) [47], Fast Evolutionary Programming (FEP) [47], Improved Fast Evolutionary Programming (IFEP) [47] and Particle Swarm Optimization [48] are compared and the comparison of results are detailed in **Table 8**. From the comparison of results, it is clear that the proposed approach provides comparable result for economic dispatch problem with piecewise quadratic function.

The computational time for the above case studies by the proposed approach is presented in **Table 9**.

The proposed methodology has following merits.

Table 7. Economic dispatch results of 10 unit system with multiple fuel options (Load=2700 MW).

Unit	Fuel type	Generation (MW)	Unit	Fuel type	Generation (MW)
1	**2**	**218**	6	**3**	**240**
2	**1**	**212**	7	**1**	**288**
3	**1**	**281**	8	**3**	**240**
4	**3**	**240**	9	**3**	**428**
5	**1**	**278**	10	**1**	**275**
Total cost ($/h)					**623.81**

Table 8. Comparison of total fuel cost for 10 unit system with multiple fuel options.

Method	Total fuel cost ($/h)		
	2500 MW	2600 MW	2700 MW
HM [43]	526.70	574.03	625.18
HNN [44]	526.13	574.26	626.12
AHNN [45]	526.23	574.37	626.24
HGA [46]	526.24	574.38	623.81
IFEP [47]	526.25	---	---
FEP [47]	526.26	---	---
CEP [47]	526.25	---	---
PSO [48]	---	---	623.88
Proposed method	**526.24**	**574.38**	**623.81**

Table 9. Total execution time for various case studies.

Case study	Test system	Execution time (s)
ED	40 Unit	1.5337
	15 Unit	0.6642
CEED	6 Unit	0.2613
MAED	Two area system	0.2534
EDMFO	10 Unit	0.2700

- From these studies, this approach has the competence to solve various types of economic dispatch problem.
- It is a first method that provides the optimal solution for all possible load demands of system in a single run.
- It provides the schedule with minimum total cost in all cases hence global optimal solution.
- The performance of the proposed approach is independent of the number of generating units in the system and hence it is suitable for system of any size.
- The computational procedure is minimal.
- It offers the solution for all load demands of a system hence it takes a reasonable execution time.

5. Conclusions

This article presents sequential approach with matrix framework for solving various kinds of economic dispatch problems. The proposed methodology is validated by solving the different economic load dispatch problem such as large scale economic dispatch, economic dispatch with generator operating constraints, combined economic and emission dispatch, multiarea economic dispatch and economic dispatch with multiple fuel options. The different scale of power systems are considered in each case. The practical operational constraints of generators like ramp rate limits and prohibited operating zones are also taken into account for the solution of economic dispatch problems. The price penalty factor approach is used to convert the multi objective optimization problem into single objective optimization problem and maximum price penalty factor is considered as it offers very good solution for emission constrained less cost condition. The proposed approach is extended for solving economic dispatch problems with line flow constraints. Further, simple methodology for solving economic dispatch problem with multiple fuel options is presented. The most economic fuel of generating unit is identified by using the composite cost function and sequential approach with matrix frame work. These decentralized approaches provide simple solution methodology for economic dispatch problem with multiple fuel options. The simulation results of different case studies are compared with recent reports. The comparison of results concludes that the proposed methodology provides the minimum total fuel cost hence global optimal solution for various types of economic dispatch problems.

6. Acknowledgements

The authors gratefully acknowledge the management the support and facilities provided by the authorities of Annamalai University, Annamalainagar, India to carry out this research work.

7. References

[1] A. J. Woods and B. F. Wollenberg, "Power Generation, Operation and Control," John Wiley & Sons, New York, 1996.

[2] O. I. Elgerd, "Electric Energy Systems Theory, An introduction," 2nd Edition, McGraw Hill Book Company, New York, 1982.

[3] R. B. Adler and R. Fischal, "Security Constrained Economic Dispatch with Participation Factors Based on Worst Case Bus Load Violations," *IEEE Transactions on Power Apparatus and Systems*, Vol. 96, 1977, pp. 347-356.

[4] R. T. Bui and S. Ghaderpanah, "Real Rescheduling and Security Assessment," *IEEE Transactions on Power Apparatus and Systems*, Vol. PAS-101, No. 8, 1982, pp. 2906-2915.

[5] K. P. Wong and C. C. Wang, "Simulated Annealing Based Economic Dispatch Algorithm," *IEE Proceedings in Generation, Transmission and Distribution*, Vol. 140, No. 6, 1993, pp. 509-515.

[6] S. O. Orero and M. R. Erving, "Economic Dispatch of Generators with Prohibited Operating Zones: A Genetic Algorithm Approach," *IEE Proceedings in Generation, Transmission and Distribution*, Vol. 143, No. 6, 1996, pp. 529-534.

[7] M. Djukanovic, M. Calovic, B. Milosevic and D. J. Sobejic, "Neural-Net Based Real Time Economic Dispatch for Thermal Power Plants," *IEEE Transactions on Energy Conversion*, Vol. 11**,** No. 4, 1996, pp. 755-761.

[8] R. Naresh, J. Dubey and J. Sharma, "Two-Phase Neural Network Based Modelling Framework of Constrained Economic Load Dispatch," *IEE Proceedings in Generation, Transmission and Distribution*, Vol. 151, No. 3, 2004, pp. 373-378.

[9] Z. L. Gaing, "Particle Swarm Optimization to Solving the Economic Dispatch Considering the Generator Constraints," *IEEE Transactions on Power Systems*, Vol. 18, No. 3, 2003, pp. 1187-1195.

[10] J.-B. Park, K.-S. Lee, J.-R. Shin and K. Y. Lee, "A Particle Swarm Optimization for Economic Dispatch with Non-Smooth Cost Function," *IEEE Transactions on Power Systems*, Vol. 20, No. 1, 2005, pp. 34-42.

[11] A. P. Neto, C. Unsihuay and O. R. Saveedra, "Efficient Evolutionary Strategy Optimization Procedure to Solve the Non-Convex Economic Dispatch Problem with Generator Constraints," *IEE Proceedings on Generation Transmission and Distribution*, Vol. 152, No. 5, 2005, pp. 653-660.

[12] W.-M. Lin, H.-J. Gow and M.-T. Tsay, "A Partition Approach Algorithm for Non-Convex Economic Dispatch," *Electric Power and Energy Systems*, Vol. 29, No. 5, 2007, pp. 432-438.

[13] A. Y. Abdelaziz, S. F. Mekhamer, M. A. L. Badr and M. Z. Kamz, "Economic Dispatch Using an Enhanced Hopfield Neural Network," *Electric Power Components and Systems*, Vol. 36, No. 7, 2008, pp. 719-732.

[14] N. Noman and H. Iba, "Differential Evolution for Economic Dispatch Problems," *Electric Power Systems Research*, Vol. 78, No. 8, 2008, pp. 1322-1331.

[15] J.-P. Chiou, "Variable Scaling Hybrid Differential Evolution for Large Scale Economic Dispatch Problems," *Electric Power Systems Research*, Vol. 77, No. 3-4, 2007, pp. 212-218.

[16] J. Cai, X. Ma, L. Li, Y. Yang, H. Peng and X. Wang, "Chaotic Ant Swarm Optimization to Economic Dispatch," *Electric Power Systems Research*, Vol. 77, No. 10, 2007, pp. 1373-1380.

[17] A. Theerthamalai and S. Maheswarapu, "Directional Search Genetic Algorithm Applications to Economic Dispatch of Thermal Units," *International Journal of Computational Methods in Engineering Science and Mechanics*, Vol. 9, No. 4, 2008, pp. 211-216.

[18] C. C. Kuo, "A Novel Coding Scheme for Practical Economic Dispatch by Modified Particle Swarm Approach," *IEEE Transactions on Power Systems*, Vol. 23, No. 4, 2008, pp. 1825-1835.

[19] B. K. Panigrahi and V. R. Pandi, "Bacterial Foraging Optimization: Nelder-Mead Hybrid Algorithm for Economic Load Dispatch," *IET Generation, Transmission and Distribution*, Vol. 2, No. 4, 2008, pp. 556-565.

[20] "Potential Impacts of Clean Air Regulations on System Operations," *IEEE Current Operating Problems Working Group*, Vol. 10, 1998, pp. 647-653.

[21] A. A. El-keib, H. Ma and J. L. Hart, "Environmentally Constrained Economic Dispatch Using a Lagrangian Relaxation Method," *IEEE Transactions on Power Systems*, Vol. 9, No. 4, 1994, pp. 1723-1729.

[22] M. W. Lamont and E. V. Qbessis, "Emission Dispatch Models and Algorithms for the 1990's," *IEEE Transactions on Power Systems*, Vol. 10, No. 2, 1995, pp. 941-947.

[23] K. Srikrishna and C. Palanichamy, "Economic Thermal Power Dispatch with Emission Constraint," *Journal of Institution of Engineers* (*India*), Vol. 72, 1991, pp. 11-18.

[24] Y. H. Song, G. S. Wang, P. Y. Wang and A. T. Johns, "Environmental/Economic Dispatch Using Fuzzy Logic Controlled Genetic Algorithms," *IEE Proceedings on Generation, Transmission and Distribution*, Vol. 144, No. 4, 1997, pp. 377-382.

[25] G. Singh, S. C. Srivastava, P. K. Kalra and D. M. Vinoth Kumar, "Fast Approach to Artificial Neural Network Training and its Application to Economic Load Dispatch," *Electrical Machines and Power Systems*, Vol. 23, No. 1, 1995, pp. 13-24.

[26] C. T. Su and G. J. Chiou, "A Fast Computation Hopfield Method to Economic Load Dispatch of Power Systems," *IEEE Transactions on Power Systems*, Vol. 12, No. 4, 1997, pp. 1759-1764.

[27] C. M. Haung, H. T. Yang and C. L. Huang, "Bi-objective Power Dispatch Using Fuzzy Satisfaction-Maximizing Decision Approach," *IEEE Transactions on Power Systems*, Vol. 12, No. 4, 1997, pp. 1715-1721.

[28] P. K. Hota, R. Chakrabarti and P. K. Chattopadhyay,

"Economic Emission Load Dispatch through an Interactive Fuzzy Satisfying Method," *Electric Power Systems Research*, Vol. 54, No. 3, 2000, pp. 151-157.

[29] K. P. Wong and J. Yuryevich, "Evolutionary Programming Based Algorithm for Environmentally Constrained Economic Dispatch," *IEEE Transactions on Power Systems*, Vol. 13, No. 2, 1998, pp. 301-309.

[30] P. Venkatesh, R. Gnanadass and N. P. Padhy, "Comparison and Application of Evolutionary Programming Techniques to Combined Economic Emission Dispatch with Line Flow Constraints," *IEEE Transactions on Power Systems*, Vol. 18, No. 2, 2003, pp. 688-697.

[31] R. M. S. Danaraj and F. Gajendran, "Quadratic Programming Solution to Emission and Economic Dispatch Problems," *Journal of Institution of Engineers* (*India*), Vol. 86, 2005, pp. 129-132.

[32] S. Muralidharan, K. Srikrishna and S. Subramanian, "Emission Constrained Economic Dispatch—A New Recursive Approach," *Electric Power Components and Systems*, Vol. 34, No. 3, 2006, pp. 343-353.

[33] L. F. Wang and C. Singh, "Environmental/Economic Power Dispatch Using a Fuzzified Multi-Objective Particle Swarm Optimization Algorithm," *Electric Power Systems Research*, Vol. 77, No. 12, 2007, pp. 1654-1664.

[34] J. S. AL-Sumait, J. K. Sykulski and A. K. L-Othman, "Solution of Different Types of Economic Dispatch Problems Using Pattern Search Method," *Electric Power Components and Systems*, Vol. 36, No. 3, 2008, pp. 250-265.

[35] R. Balamurugan and S. Subramanian, "A Simplified Recursive Approach to Combined Economic Emission Dispatch," *Electric Power Components and Systems*, Vol. 36, No. 1, 2008, pp. 17-27.

[36] C. Palanichamy and N. S. Babu, "Analytical Solution for Combined Economic and Emissions Dispatch," *Electric Power Systems Research*, Vol. 78, No. 7, 2008, pp. 1129-1137.

[37] K. T. Chaturvedi, M. Pandit and L. Srivstava, "Modified Neo-Fuzzy Neuron Based Approach for Economic and Environmental Optimal Power Dispatch," *Applied Soft Computing*, Vol. 8, No. 4, 2008, pp. 1428-1438.

[38] S. Agrawal, B. K. Panigrahi and M. K. Tiwari, "Multi-Objective Particle Swarm Algorithm with Fuzzy Clustering for Electrical Power Dispatch," *IEEE Transactions on Evolutionary Computation*, Vol. 12, No. 15, 2008, pp. 529-541.

[39] R. Geetha, R. Bhuvaneswari and S. Subramanian, "Artificial Immune System Based Combined Economic and Emission Dispatch," *Proceedings of IEEE TENCON*, IEEE Region 10 conference, Hyderabad, 2008.

[40] X. B. Li, "Study of Multi-Objective Optimization and Multi-Attribute Decision-Making for Economic and Environmental Power Dispatch," *Electric Power Systems Research*, Vol. 79, No. 5, 2009, pp. 789-795.

[41] C. L. Chen and N. Chen, "Direct Search Method for Solving Economic Dispatch Problem Considering Transmission Capacity Constraints," *IEEE Transactions on Power Systems*, Vol. 16, No. 4, 2001, pp. 764-769.

[42] T. Yalcinoz and M. J. Short, "Neural Networks Approach for Solving Economic Dispatch Problem with Transmission Capacity Constraints," *IEEE Transactions on Power Systems*, Vol. 13, No. 2, 1998, pp. 307-313.

[43] C. E. Lin and G. L. Viviani, "Hierarchical Economic Dispatch for Piecewise Quadratic Cost Functions," *IEEE Transactions on Power Apparatus and Systems*, Vol. PAS -103, No. 6, 1984, pp. 1170-1175.

[44] J. H. Park, Y. S. Kim, I. K. Eom and K. Y. Lee, "Economic Load Dispatch for Piecewise Quadratic Cost Function using Hopfield Neural Network," *IEEE Transactions on Power Systems*, Vol. 8, No. 3, 1993, pp. 1030-1038.

[45] K. Y. Lee, A. S. Yome and J. H. Park, "Adaptive Hopfield Neural Networks for Economic Load Dispatch," *IEEE Transactions on Power Systems*, Vol. 13, No. 2, 1998, pp. 519-526.

[46] S. Baskar, P. Subbaraj and M. V. C. Rao, "Hybrid Genetic Algorithm Solution to Economic Dispatch Problem with Multiple Fuel Options," *Journal of Institution of Engineers* (*India*), Vol. 82, 2001, pp. 177-183.

[47] T. Jayabarathi, K. Jayaprakash, D. N. Jayakumar and T. Raghunathan, "Evolutionary Programming Techniques for Different Kinds of Economic Dispatch Problems," *Electric Power Systems Research*, Vol. 73, No. 2, 2005, pp. 169-176.

[48] D. N. Jeyakumar, T. Jayabharathi and T. Raghunathan, "Particle Swarm Optimization for Various Types of Economic Dispatch Problems," *Electric Power and Energy Systems*, Vol. 28, No. 1, 2006, pp. 36-42.

Nomenclature

a_i, b_i, c_i Cost coefficients of generating unit i
d_i, e_i, f_i Emission coefficients of generating unit i
B_{ij}, B_{0i}, B_{00} Transmission loss coefficients or B coefficients
E_T Total emission of generators in (kg/h)
F_T Total operating cost or total fuel cost of generation in ($/h)
n Number of generating units
n_i Number of prohibited operating zones
P_i Real power generation of generating unit i in MW
$P_{i,min}$ Minimum value of real power allowed at generator i in MW
$P_{i,max}$ Maximum value of real power allowed at generator i in MW
P_D Total load demand of the system in MW
P_L Total transmission losses in MW
P_i^0 Output power of generator i before dispatched hour in MW
$P_{i,j}^l$ Lower bound of generation of unit i in prohibited operating zone j in MW
$P_{i,j}^u$ Upper bound of generation of unit i in prohibited operating zone j in MW
UR_i Up ramp limit of i th generator in (MW/h)
DR_i Down ramp limit of i th generator in (MW/h)
h Price penalty factor in ($/kg)
$h_{i,max}$ Maximum price penalty factor of unit i in ($/kg)
M Number of areas in an interconnected system
N_m Number of on-line units for the area m in an M area system
a_{mn}, b_{mn}, c_{mn} Cost coefficients of generating unit n in area m
P_{mn} Power output of generator n in area m in MW
P_{Dm} Load demand for area m in MW
t_{jk} Economic tie transfer from area j to k in MW
$t_{jk,min}, t_{jk,max}$ Tie line minimum and maximum capacity limits in MW
β_m Set of tie lines in area m
s One dimensional matrix consists of input values
I Square matrix consists of real power generations of units
fit Fitness of the solution in ($/MWh)
P_{min} Minimum technical limit in MW
P_{max} Maximum technical limit in MW

Appendix

The incremental production cost of a plant is a prior requirement for coordination among plants. The incremental production cost of the plant can be derived by a simple realignment of the fuel cost coefficients of the units. Consider an "n" unit system and the cost equation of n th unit is,

$$F_n = a_n P_n^2 + b_n P_n + c_n \tag{A.1}$$

and the composite cost function of the plant can be written as,

$$F_T = AP_G^2 + BP_G + C \tag{A.2}$$

The composite cost coefficients are derived as follows. The total fuel cost ($/h) of the "n" unit system can be written as,

$$F_T = F_1 + F_2 + F_3 + ... + F_n \tag{A.3}$$

For most economical generation,

$$\begin{aligned} &2a_1P_1 + b_1 = \lambda \quad ; \quad P_1 = (\lambda - b_1)/2a_1 \\ &. \\ &2a_nP_n + b_n = \lambda \quad ; \quad P_n = (\lambda - b_n)/2a_n \\ &---------- \\ &2AP_G + B = \lambda \quad ; \quad P_G = (\lambda - B)/2A \end{aligned} \tag{A.4}$$

where, λ is the incremental production cost of the plant in MW.

The total generation of the plant can be written as,

$$P_G = P_1 + P_2 + P_3 + ... + P_n$$

$$\begin{aligned} P_G = &\left[(\lambda/2)(1/a_1 + 1/a_2 + 1/a_3 + ... + 1/a_n)\right] \\ &-\left[(1/2)(b_1/a_1 + b_2/a_2 + b_3/a_3 + ... + b_n/a_n)\right] \end{aligned}$$

$$\begin{aligned} \lambda = &2\left[1/(1/a_1 + 1/a_2 + 1/a_3 + ... + 1/a_n)\right]P_G \\ &+ (b_1/a_1 + b_2/a_2 + b_3/a_3 + ... + b_n/a_n) \\ &\left[1/(1/a_1 + 1/a_2 + 1/a_3 + ... + 1/a_n)\right] \end{aligned} \tag{A.5}$$

By comparing (A.4) and (A.5),

$$A = 1/(1/a_1 + 1/a_2 + 1/a_3 + ... + 1/a_n) \tag{A.6}$$

$$B = (b_1/a_1 + b_2/a_2 + b_3/a_3 + ... + b_n/a_n)A \tag{A.7}$$

The fuel cost can be rewritten as,

$$\begin{aligned} F_n &= \lambda^2/4a_n - b_n^2/4a_n + c_n; \\ F_T &= \lambda^2/4A - B^2/4A + C; \end{aligned} \tag{A.8}$$

From (A.8),

$$\begin{aligned} C = &(c_1 + c_2 + c_3 + ... + c_n) \\ &(b_1^2/4a_1 + b_2^2/4a_2 + b_3^2/4a_3 + ... + b_n^2/4a_n) \\ &+ B^2/4A \end{aligned} \tag{A.9}$$

Energy and Power Engineering, **2010, 2, 122-126**
doi:10.4236/epe.2010.22017 Published Online May 2010 (http://www. SciRP.org/journal/epe)

Anisotropic Scattering for a Magnetized Cold Plasma Sphere

Yingle Li[1], Mingjun Wang[1], Qunfeng Dong[2], Gaofeng Tang[1]
[1]*Institute of Radio Wave Propagation & Scattering, Xianyang Normal University, Xian Yang, China*
[2]*Northwestern Polytechnical University, Xi'an, China*
E-mail: *liyinglexidian@yahoo.com.cn*
Received December 10, 2009; *revised February* 6, 2010; *accepted March* 9, 2010

Abstract

The transformation of parameter tensors for anisotropic medium in different coordinate systems is derived. The electric field for a magnetized cold plasma sphere and the general expression of scattering field from anisotropic target are obtained. The functional relations of differential scattering cross section and the RCS for the magnetized plasma sphere are presented. Simulation results are in agree with that in the literatures, which shows the method used and results obtained are correct and the results provide a theoretical base for anisotropic target identification etc.

Keywords: Anisotropy, Scattering, Plasma

1. Introduction

Plasma is an anisotropic medium in the outside magnetic field. It has widely applied fields such as modern Radar system, antenna system and target concealing and thus has been of increasing interest [1-4]. In [5], the E.M. scattering features for a conductor sphere coated with plasma are researched by expanding the electromagnetic field into a series of vector spherical functions. The propagation and absorbability of a circular polarizing E.M. wave in asymmetric plasma are also studied [6,7], some results are tested with experiments. The interaction of an E.M. wave and an inhomogeneous plasma slab with electron distribution in the form of partially linear and sinusoidal profiles [8] is researched in which it has been found that inhomogeneous plasma slab can be used as a broad band radar absorbing layer. The scattering characteristics of target coated with plasma are researched [9] by using physical optical and input impedance methods. Other targets coated with plasma are studied [10] based on the medium laminar modeling and the effect induced by the plasma parameters on scattering features is analyzed. In recent years, the interaction of anisotropic targets with light, electromagnetic wave also has been of great interest [11,12]. The research techniques of scattering wave from anisotropic medium and plasma can be divided into three, namely, analytical method, approximation method and numeration. The later two are based on the first. In some literatures, the changes of elements of dielectric tensor and permeability tensor with coordinate systems are ignored, the orthonormalities of spherical vector wave functions based on the Helmholtz equation derived in the isotropic medium are also ignored and being directly used them to the anisotropic medium. So some errors are inevitable in those obtained results. On the other hand the expression of scattering field from a magnetized cold plasma target is not much published. In the present paper, the expression of the electric field inside & outside a magnetized cold plasma spherical target is presented in detail based on the scale transformation theory of the electromagnetic field by transforming the dielectric tensor in the right angle coordinate system into the spherical system. A formula of computing the scattering field from a general anisotropic target is then developed. Based on the formulae, the Rayleigh scattering features of a magnetized plasma sphere are researched. The effects induced on the feature by the factors of electric density, incident angle and outside magnetic field etc. are demonstrated. The time-harmonic factor $e^{-j\omega t}$ is used in this paper.

2. Research of Rayleigh Scattering from a Magnetized Plasma Sphere

2.1. Expressions of Electric Fields inside and outside a Magnetized Cold Plasma Sphere

Assume a magnetized cold plasma sphere to have radius R_0 and its centre to be located at the origin of the primary

coordinate system Σ. The outside magnetic field B_0 is in z-axis. The dielectric constant tensor of this plasma sphere is given as [5]

$$\varepsilon = \varepsilon_r \varepsilon_0 = \varepsilon_0 \begin{bmatrix} \varepsilon & -j\varepsilon_p & 0 \\ j\varepsilon_p & \varepsilon & 0 \\ 0 & 0 & \varepsilon_1 \end{bmatrix} \tag{1}$$

By utilizing the relation between $\boldsymbol{D}$ and $\boldsymbol{E}$ and the relation between the vectors in right angle system and spherical system, we can obtain the expression of the dielectric constant tensor in spherical coordinate system as

$$\boldsymbol{\varepsilon} = \varepsilon_0 \begin{bmatrix} \varepsilon_{11} & \varepsilon_{12} & \varepsilon_{13} \\ \varepsilon_{21} & \varepsilon_{22} & \varepsilon_{23} \\ \varepsilon_{31} & \varepsilon_{32} & \varepsilon_{33} \end{bmatrix} \tag{2}$$

where

$$\begin{aligned} \varepsilon_{11} &= \varepsilon + (\varepsilon_1 - \varepsilon)\cos^2\theta \\ \varepsilon_{12} &= -(\varepsilon_1 - \varepsilon)\cos\theta\sin\theta \\ \varepsilon_{13} &= -j\varepsilon_p \sin\theta \\ \varepsilon_{22} &= \varepsilon_1 - (\varepsilon_1 - \varepsilon)\cos^2\theta \\ \varepsilon_{23} &= -j\varepsilon_p \cos\theta, \varepsilon_{33} = \varepsilon \\ \varepsilon_{12} &= \varepsilon_{21}, \varepsilon_{13} = -\varepsilon_{31}, \varepsilon_{32} = -\varepsilon_{23} \end{aligned}$$

$$\varepsilon_p = \frac{\frac{ne^3 B_0}{m^2\omega^3\varepsilon_0}}{1-\frac{e^2B_0^2}{m^2\omega^2}}, \quad \varepsilon_1 = 1-\frac{ne^2}{m\omega^2\varepsilon_0}, \varepsilon = 1-\frac{\frac{ne^2}{m\omega^2\varepsilon_0}}{1-\frac{e^2B_0^2}{m^2\omega^2}}$$

n, m are the electron density and electron mass respectively, ω the angle frequency of incident wave. Expression (2) indicates that the dielectric tensor is relative to the observing point. When the frequency is low, the condition $\lambda >> R_0$ is satisfied, it is so approximately considered that the magnetized cold plasma sphere locates in the electrostatic field [13,14]. The plasma has not electric charge in whole, according to the formulae $\nabla \cdot \mathbf{D} = 0$, $\mathbf{E} = -\nabla u$ and considering that the differential of potential u is not relative to the order for x and y, the differential equation of u is obtained as in the primary coordinate system

$$\varepsilon \frac{\partial^2 u}{\partial x^2} + \varepsilon \frac{\partial^2 u}{\partial y^2} + \varepsilon_1 \frac{\partial^2 u}{\partial z^2} = 0 \tag{3}$$

Now, a scale coordinate system Σ" is introduced as a new coordinate system. The coordinates of this system are indicated with x', y' and z'. The relation of coordinates between the two systems is written as

$$x' = \frac{x}{\sqrt{\varepsilon}}, y' = \frac{y}{\sqrt{\varepsilon}}, z' = \frac{z}{\sqrt{\varepsilon_1}}$$

The differential equation of the potential in the scale coordinate system is derived by substituting the above expressions into Equation (3) and using the condition $u = u'$ [14] at any spatial point, and it is expressed as

$$\frac{\partial^2 u'}{\partial x'^2} + \frac{\partial^2 u'}{\partial y'^2} + \frac{\partial^2 u'}{\partial z'^2} = 0 \tag{4}$$

The condition $u = u'$ is understandable, for the potential is defined as the work done by the electric field to move a unit charge from one point to the reference point, namely W/q, so both the numerator and the denominator are scale invariants. Equation (4) shows that a magnetized cold plasma sphere in the primary coordinate system is transformed into an isotropic sphere in the scale coordinate system from the view point electric potential equation. This manipulation can greatly simplify the electromagnetic scattering problems. It is well known that the solution of Equation (4) can be obtained by using the method of separation of variables as follows:

$$\begin{aligned} u'(R', \theta', \phi') = &\sum_{m,n} a_{m,n} R'^n P_n^m(\cos\theta')\cos m\phi' \\ &+ \sum_{m,n} c_{m,n} R'^n P_n^m(\cos\theta')\sin m\phi' \end{aligned} \tag{5}$$

Expression (5) is a general solution in the scale coordinate system. The parameters in the two coordinate systems can be found in literature [10]. The electric potential outside the sphere is expressed as

$$\begin{aligned} u_1(R, \theta, \phi) = &\sum_{m,n} \left(e_{m,n} R^n + \frac{f_{m,n}}{R^{n+1}} \right) P_n^m(\cos\theta)\cos m\phi \\ &+ \sum_{m,n} \left(g_{m,n} R^n + \frac{h_{m,n}}{R^{n+1}} \right) P_n^m(\cos\theta)\sin m\phi \end{aligned} \tag{6}$$

On the surface of the sphere, the electric potential inside the sphere is equal to that outside the sphere and the electric displacement $\boldsymbol{D}$ is continuous in the normal direction, namely

$$\begin{aligned} u\big|_{R=R_0} &= u_1\big|_{R=R_0} \\ \varepsilon_0 \left(\varepsilon_{11} \frac{\partial u}{\partial R} + \varepsilon_{12} \frac{1}{R} \frac{\partial u}{\partial \theta} + \varepsilon_{13} \frac{1}{R\sin\theta} \frac{\partial u}{\partial \phi} \right)\Bigg|_{R=R_0} &= \varepsilon_0 \frac{\partial u_1}{\partial R}\Bigg|_{R=R_0} \end{aligned} \tag{7}$$

Inserting Expressions (5), (6) and (7) into the above conditions yields the solution of electric potential inside and outside a magnetized cold plasma sphere as

$$\begin{aligned} u(R, \theta, \phi) = &\frac{3A}{2+\varepsilon_1} R\cos\theta + \frac{3(2B + B\varepsilon + jC\varepsilon_p)}{\varepsilon^2 + 4\varepsilon - \varepsilon_p^2 + 4} R\cos\phi\sin\theta \\ &+ \frac{3(2C + C\varepsilon - jB\varepsilon_p)}{\varepsilon^2 + 4\varepsilon - \varepsilon_p^2 + 4} R\sin\phi\sin\theta \end{aligned} \tag{8}$$

$$\begin{aligned} u_1(R,\theta,\phi) &= AR\cos\theta \\ &+ BR\sin\theta\cos\phi \\ &+ CR\sin\theta\sin\phi \\ &+ \frac{AR_0^3}{R^2}\frac{1-\varepsilon_1}{2+\varepsilon_1}\cos\theta \\ &- \frac{R_0^3\left(B\varepsilon^2+B\varepsilon-2B-B\varepsilon_p^2-3jC\varepsilon_p\right)}{\varepsilon^2+4\varepsilon-\varepsilon_p^2+4}\sin\theta\cos\phi \\ &- \frac{R_0^3\left(C\varepsilon^2+C\varepsilon-2C-C\varepsilon_p^2+3jB\varepsilon_p\right)}{\varepsilon^2+4\varepsilon-\varepsilon_p^2+4}\sin\theta\sin\phi \end{aligned} \tag{9}$$

where

$A=-E_0\cos\theta_0, B=-E_0\sin\theta_0\cos\phi_0, C=-E_0\sin\theta_0\sin\phi_0$.

From Expression (8), the electric field is obtained as

$$\begin{aligned} \mathbf{E} &= -\frac{3\left(2C+C\varepsilon-jB\varepsilon_p\right)}{\varepsilon^2+4\varepsilon-\varepsilon_p^2+4}\hat{y} - \frac{3\left(2B+B\varepsilon+jC\varepsilon_p\right)}{\varepsilon^2+4\varepsilon-\varepsilon_p^2+4}\hat{x} \\ &\quad - \frac{3A}{2+\varepsilon_1}\hat{z} \\ &= E_x\hat{x}+E_y\hat{y}+E_z\hat{z} \end{aligned} \tag{10}$$

The above result is obviously in agree with those in the reference [10] when the dielectric tensor is a uniform medium, which tests the correctness of Expression (10).

2.2. The Scattering Feature of a Magnetized Cold Plasma Sphere

The scattering field from an anisotropic target is derived as following by using the researching method in the literature [13]

$$E_s = f\left(\hat{i},\hat{r}\right)\frac{e^{jkr}}{r} \tag{11}$$

where

$$f\left(\hat{i},\hat{r}\right) = \frac{k^2}{4\pi}\int_v\left\{-\hat{r}\times\left[\hat{r}\times\left(\boldsymbol{D}-\boldsymbol{E}\right)\right]\right\}e^{-j\mathbf{k}r'\cdot\hat{\mathbf{r}}}dv' \tag{12}$$

is the amplitude of scattering field and $\boldsymbol{E}$ $\boldsymbol{D}$ are respectively electric field & the 'electric displacement' inside the plasma sphere, in which $\boldsymbol{D}=\varepsilon_r\cdot\boldsymbol{E}$, has the same unit with $\boldsymbol{E}$. Expression of $\boldsymbol{D}$-$\boldsymbol{E}$ written as

$$\boldsymbol{D}-\boldsymbol{E}=\left(\left(\varepsilon-1\right)E_x-j\varepsilon_pE_y\right)\hat{x}+\left(\left(\varepsilon-1\right)E_y+j\varepsilon_pE_x\right)\hat{y}+\left(\varepsilon_1-1\right)E_z\hat{z}$$

Inserting the above into Expression (12) and considering that $kr'=\frac{2\pi}{\lambda}r'<<1$, the amplitude is derived as following

$$f\left(\hat{i},\hat{r}\right)=\frac{k^2\mathrm{V}}{4\pi}\begin{bmatrix}\left(\left(\varepsilon-1\right)E_x-j\varepsilon_pE_y\right)\hat{x}+\left(\left(\varepsilon-1\right)E_y+j\varepsilon_pE_x\right)\hat{y}\\+\left(\varepsilon_1-1\right)E_z\hat{z}\\-\hat{r}\begin{pmatrix}\left(\left(\varepsilon-1\right)E_x-j\varepsilon_pE_y\right)r_x\\+\left(\left(\varepsilon-1\right)E_y+j\varepsilon_pE_x\right)r_y+\left(\varepsilon_1-1\right)E_zr_z\end{pmatrix}\end{bmatrix} \tag{13}$$

The symbol V is the sphere's volume and vectors $\hat{r},\hat{i}$ are respectively the vectors in scattering direction and incident direction.

$\hat{r}=\sin\theta\cos\phi\hat{x}+\sin\theta\sin\phi\hat{y}+\cos\theta\hat{z}=r_x\hat{x}+r_y\hat{y}+r_z\hat{z}$. In our knowledge, Expression (13) is a novel one. The projections of amplitude in the right coordinate system are

$$\mathrm{f}_x\left(\hat{\mathrm{i}},\hat{\mathrm{r}}\right)=\frac{\mathrm{k}^2\mathrm{V}}{4\pi}\begin{bmatrix}\left(\left(\varepsilon-1\right)\mathrm{E}_x-\mathrm{j}\varepsilon_\mathrm{p}\mathrm{E}_y\right)-\left(\left(\varepsilon-1\right)E_x-j\varepsilon_pE_y\right)r_x^2\\-\left(\left(\varepsilon-1\right)E_y+j\varepsilon_pE_x\right)r_xr_y-\left(\varepsilon_1-1\right)E_zr_xr_z\end{bmatrix}$$

$$\mathrm{f}_y\left(\hat{\mathrm{i}},\hat{\mathrm{r}}\right)=\frac{\mathrm{k}^2\mathrm{V}}{4\pi}\begin{bmatrix}\left(\left(\varepsilon-1\right)\mathrm{E}_y+\mathrm{j}\varepsilon_\mathrm{p}\mathrm{E}_x\right)-\left(\left(\varepsilon-1\right)E_y+j\varepsilon_pE_x\right)r_y^2\\-\left(\left(\varepsilon-1\right)E_x-j\varepsilon_pE_y\right)r_xr_y-\left(\varepsilon_1-1\right)E_zr_yr_z\end{bmatrix}$$

$$\mathrm{f}_z\left(\hat{\mathrm{i}},\hat{\mathrm{r}}\right)=\frac{\mathrm{k}^2\mathrm{V}}{4\pi}\begin{bmatrix}\left(\varepsilon_1-1\right)E_z-\left(\left(\varepsilon_1-1\right)E_z\right)r_z^2\\-\left(\left(\varepsilon-1\right)E_y+j\varepsilon_pE_x\right)r_zr_y-\left(\left(\varepsilon-1\right)E_x-j\varepsilon_pE_y\right)r_xr_z\end{bmatrix}$$

The differential scattering cross section is presented as

$$\sigma_\mathrm{d}=\left|\mathrm{f}\left(\hat{i},\hat{r}\right)\right|^2=\mathrm{f}_x\mathrm{f}_x^*+\mathrm{f}_y\mathrm{f}_y^*+\mathrm{f}_z\mathrm{f}_z^* \tag{14}$$

Since the inner electric field is dependent on the direction of the incident wave. So it can be seen from (13) that there are two parts in the differential scattering cross section, the first part is relative to the incident direction, the second is relative to both incident direction and the observing azimuth angle. After considering the orthonormalities of trigonometric functions, the scattering cross section is obtained

$$\sigma=\frac{6\mathrm{k}^4\mathrm{V}^2}{5\pi}\begin{bmatrix}\left|\left(\varepsilon-1\right)\mathrm{E}_x-\mathrm{j}\varepsilon_\mathrm{p}\mathrm{E}_y\right|^2+\left|\left(\varepsilon-1\right)\mathrm{E}_y+\mathrm{j}\varepsilon_\mathrm{p}\mathrm{E}_x\right|^2\\+\left|\left(\varepsilon_1-1\right)\mathrm{E}_z\right|^2\end{bmatrix} \tag{15}$$

Expression (14) is an analytical one and a novel result in our knowledge.

2.3. Discussion

In order to test the rightness of expression (14), we assume that the incident electric field $\boldsymbol{E}_0$ is in the x-direction and now obtain $B = C = 0$, $A = -E_0$. If the medium is an isotropic one and now assume $\varepsilon_1=\varepsilon,\varepsilon_\mathrm{p}=0$ is reasonable.

$$f_x\left(\hat{i},\hat{r}\right)=\frac{k^2V}{4\pi}\frac{3E_0\left(\varepsilon-1\right)}{2+\varepsilon}\left(1-r_x^2\right)$$

$$f_y\left(\hat{i},\hat{r}\right)=\frac{k^2V}{4\pi}\frac{3E_0\left(\varepsilon-1\right)}{2+\varepsilon}r_x r_y$$

$$f_z\left(\hat{i},\hat{r}\right)=\frac{k^2V}{4\pi}\frac{3E_0\left(\varepsilon-1\right)}{2+\varepsilon}r_x r_z$$

The differential scattering cross section is presented as

$$\sigma_d=\left|f\left(\hat{i},\hat{r}\right)\right|^2=\frac{k^4V^2}{\left(4\pi\right)^2}\left|\frac{3E_0\left(\varepsilon-1\right)}{2+\varepsilon}\right|^2\left(1-\left(\hat{r}\cdot\hat{x}\right)^2\right)$$

This is in agreement with what in references [13,14]. These parameters frequency f = 20 GHz, R_0 = 3 mm, and so $kR_0 << 1$ are used in the simulations:

The influence of outside magnetic field on the RCS and the parameters used are all demonstrated in **Figure 1**. It indicates that the RCS decreases when the outside magnetic field increases and magnitude of electric density is given. The reason is that the anisotropy of plasmais enhanced as the outside magnetic field increase. This change in **Figure 1** is in agreement with that in the literature [15,16]. **Figure 2** shows that the angle θ_0 between electric field and B_0 has an effect on RCS and φ_0 has no impact. We know that the anisotropy has a good symmetry in the plane, x-y plane, after the isotropic plasma sphere being magnetized. Thus the plasma is isotropic medium in the plane of x-y and the RCS is not impacted by angle φ_0. The scattering characteristic change with frequency is presented in **Figure 3**. It is well known that the Rayleigh scattering field is radiated by the electromagnetic sources inside the plasma. Those radiating sources have the same phase and so the radiations are mainly electric dipole radiations. These kinds of radiations are proportional to ω^4. It is seen from **Figure 4** that RCS will decreases as the electric density increasing, which is in agree to that in the reference [17]. This is caused by the fact that the plasma's absorbability to E.M.

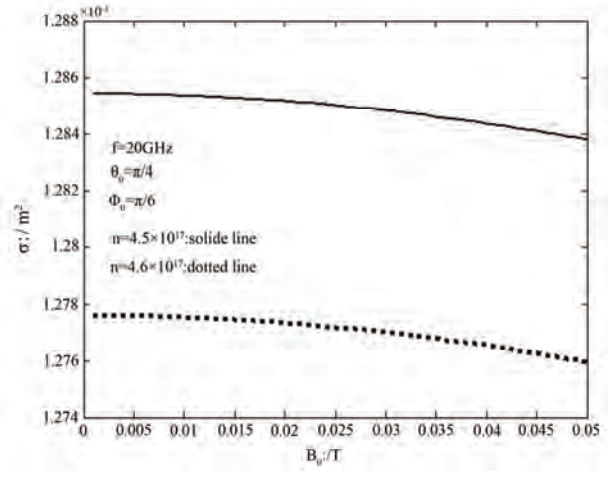

Figure 1. Change of σ versus outside field B_0.

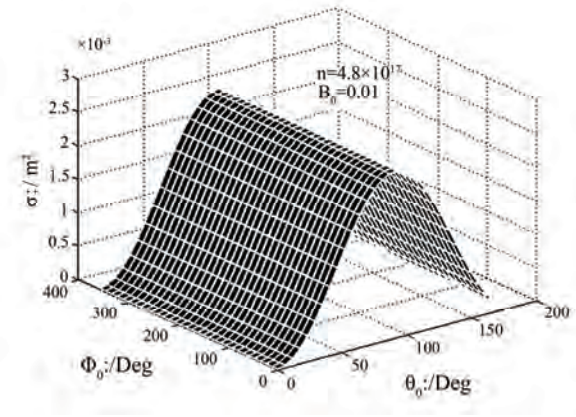

Figure 2. Change of σ versus polarization.

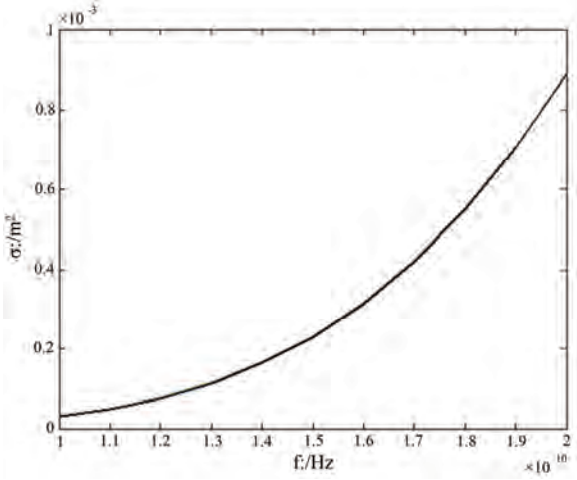

Figure 3. Change of σ versus frequency.

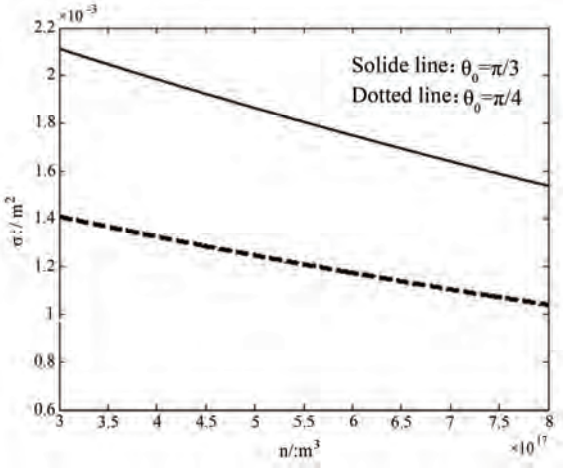

Figure 4. Change of σ versus electric density.

wave is enhanced as the electric density being increased.

3. Conclusions

In this paper, the electric fields inside and outside a magnetized cold plasma sphere are investigated. We use the scale transformation theory of the electromagnetic field to reconstruct the Laplace equation and then obtain two analytical expressions of the electric potentials inside and outside the magnetized cold plasma sphere in detail. Its correctness is tested with literature. The dielectric tensor in different coordinate systems and a general formula to compute the scattering field from anisotropic target are presented. We take the magnetized cold plasma sphere as an example, its analytical RCS is obtained first in detail and simulations are presented which indicates the characteristic of electric dipole radiation. How to use the scale transformation theory to study the analytical scattering feature for a multilayer magnetized cold plasma target is our next research subject.

4. Acknowledgements

This project was supported by the National Natural Science Foundation of China (Grant No. 60971079, 60801047), the Natural Science Foundation of Shaanxi Province (Grant No. 2009JM8020) and Natural Science Foundation of Shaanxi Educational Office (Grant No. 09JK800).

5. References

[1] E. A. Soliman, A. Helaly and A. A. Megahed, **"**Propagation of Electromagnetic Waves in Planar Bounded Plasma Region," *Progress in Electromagnetics Research*, Vol. 67, 2007, pp. 25-37.

[2] H. Huang, Y. Fan, B. Wu, F. Kong and J. A. Kong, "Surface Modes at the Interfaces between Isotropic Media and Uniaxial Plasma," *Progress in Electromagnetics Research*, Vol. 76, 2007, pp. 1-14.

[3] L. Qi and Z. Yang, "Modified Plane Wave Method Analysis of Dielectric Plasma Photonic Crystal," *Progress in Electromagnetics Research*, Vol. 91, 2009, pp. 319-332.

[4] V. Kumar, K. S. Singh and S. P. Ojha, "Band Structure, Reflection Properties and Abnormal Behaviour of One-Dimensional Plasma Photonic Crystal," *Progress in Electromagnetics Research M*, Vol. 9, 2009, pp. 227-247.

[5] W. Ren and L. Q. Xiao, "Analysis of Electromagnetic Scattering by a Plasmas-Coated Conducting Sphere Using Simplified Wave Functions," *Journal of Hangzhou Dianzi University*, in Chinese, Vol. 28, 2008, pp. 1-6.

[6] S. B. Liu, J. J. Mo and N. C. Yuan, "Research on the Absorption of EM-Wave by Inhomogeneous Magnetized Plasmas," *Acta Electronica Sinica*, in Chinese, Vol. 31, 2003, p. 372.

[7] D. J. Gregolre, J. Santoru and R. W. Schumacher, "Electromagnetic Wave Propagation in Unmagnetized Plasmas," AD-A250 710, 1992.

[8] Y. Chang, W. F. Chen and N. Luo, "Analysis of the Spatial Scattering Characteristic for the Reentry Target Cloaked by Plasma Based on the Physical Optics Method," *Journal of Microwave*, in Chinese, Vol. 24, 2008, pp. 2-6.

[9] C. S. Gürel and E. Oncü, "Interaction of Electromagnetic Wave and Plasma Slab with Partially Linear and Sinusoidal Electron Density Profile," *Progress in Electromagnetics Research Letters*, Vol. 12, 2009, pp. 171-181.

[10] D. Klement and V. Stein, "Special Problems in Applying the Physical Optics Method for Backscatter Computations of Complicated Objects," *IEEE Transactions in Antennas and Propagation*, Vol. 36, No. 2, 1988, pp. 228-237.

[11] H. T. Chen, G.-Q. Zhu and S.-Y. He, "Using Genetic Algorithm to Reduce the Radar cross Section of Three-Dimensional Anisotropic Impedance Object," *Progress in Electromagnetics Research B*, Vol. 9, 2008, pp. 231-248.

[12] V. G. Gavrilenko, G. V. Jandieri, A. Ishimaru and V. G. Jandieri, "Peculiarities of Spatial Spectrum of Scattered Electromagnetic Waves in Anisotropic Inhomogeneous Medium," *Progress in Electromagnetics Research B*, Vol. 7, 2008, pp. 191-208.

[13] A. Ishimaru, "Wave Propagation and Scattering in Random Medium," Academic Press, New York, 1978, Part I, pp. 27-30.

[14] Y. L. Li and J. Y. Huang, "The Scale-Transformation of Electromagnetic Theory and its Applications," *Chinese Physics*, in Chinese, Vol. 14, 2005, pp. 646-656.

[15] Y. Li, L. J. Xu and N. C. Yuan, "The Parallel JEC-FDTD Algorithm for Magnetized Plasmas and its Application," *Acta Electronica Sinica*, in Chinese, Vol. 36, 2008, pp. 1119-1124.

[16] S. B. Liu, G. F. Zhang and N. C. Yuan, "Finite-Difference Time-Domain Analysis on Radar cross Section of Conducting Cube Scatter Covered with Plasmas," *Acta Physica Sinica*, in Chinese, Vol. 53, 2004, pp. 2633-2638.

[17] J. J. Mo, S. B. Liu and N. C. Yuan, "Analysis of Wide Band Scattering for Perfectly Conducting Cylinder Coated with Non-Uniform Plasma," *Journal of Microwave*, in Chinese, Vol. 19, 2003, pp. 20-25.

Energy and Power Engineering, **2010, 2, 127-130**
doi:10.4236/epe.2010.22018 Published Online May 2010 (http://www. SciRP.org/journal/epe)

Design of Multi-User Electric Power Management Device

Weiqing Tao, Jing Wang
School of Electric Engineering and Automation, Hefei University of Technology, Hefei, China
E-mail: *wqtao@mail.hf.ah.cn; tonado.wang@*163*.com*
Received December 28, 2009; *revised February* 2, 2010; *accepted April* 12, 2010

Abstract

The current consumption method of Electric Power Industry is "electricity consumption first, paying for it later". The trend of consumption method is Pre-order Electricity. If we adopt the Pre-order Electricity System, we need to replace Traditional Energy Meter with Prepayment Energy Meter. But this alteration is costly. And the alarm action of Prepayment Energy Meter are bells and alarm lamp, users can not receive alarm information timely. In this paper, we present the design of Multi-user Electric Power Management Device. The device uses TMS320F2812 as CPU, with peripheral devices such as mobile phone communication module MC55, so the device supports remote operation and sends alarm information via SMS, it also can communicate with the master station by GPRS. The device can be seamlessly integrated into the existing power system in order to read meter, achieve billing and Pre-order Electricity functions. In addition, the device has the Harmonic Measurement function, so it is a high cost-effective application.

Keywords: Electric Power Management, TMS320F2812, MC55, SMS, GPRS

1. Introduction

The current consumption method of Electric Power Industry is "electricity consumption first, paying for it later". The trend of consumption method is Pre-order Electricity. If we adopt the Pre-order Electricity System, we need to replace Traditional Energy Meter with Prepayment Energy Meter. But this alteration is costly.

Most Prepayment Energy Meter use IC card as voucher card. Once the IC card does not work properly, it will affect the normal operation of the Pre-order Electricity System. The most alarm action of IC card Prepayment Energy Meter are bells and alarm lamp, users can not receive alarm information timely.

In this paper, we present the design of Multi-user Electric Power Management Device. The device uses TMS320F2812 as CPU, with peripheral devices such as mobile phone communication module MC55, built-in a variety of electricity charge calculation method. The device can collect Energy Meters' electric energy information via RS485 Communication Interface or Pulse Collection Interface, and then do electricity charge calculation, choose alarm operation or power on/off operation according to the balance, and there is a SMS notification after every operation, so users can receive alarm and operating information timely. If the master station needs to do a lot of data communication, the device also can communicate with the master station by GPRS. The device can collect many Energy Meters' electric energy information via RS485 Communication Interface, to achieve Multi-user Electric Power Management purposes. We just install the device in commercial application, and avoid replacing the existing meter. In addition, the device has the Harmonic Measurement function, so it is a high cost-effective application.

2. Design of Multi-User Electric Power Management Device

2.1. Device Hardware Design

The device uses TMS320F2812 as CPU, with peripheral devices such as LCD Module, Key Module, Mobile Phone Communication Module, RS485 Communication Interface, Pulse Collection Interface, Data Storage Module, Clock Chip, Power on/off Execution Module, Signal Conditioning Module and Power Supply Module. The hardware block diagram of the device is shown in **Figure 1**.

TMS320F2812, a member of the TMS320C2000 DSP generation, is a 32-bit DSP of 150MHz maximum frequency. It has many General-Purpose Input/Output ports (GPIOA-GPIOF), 2 UART ports (UART1, UART2), with on-chip A/D sampling function. TMS320F2812

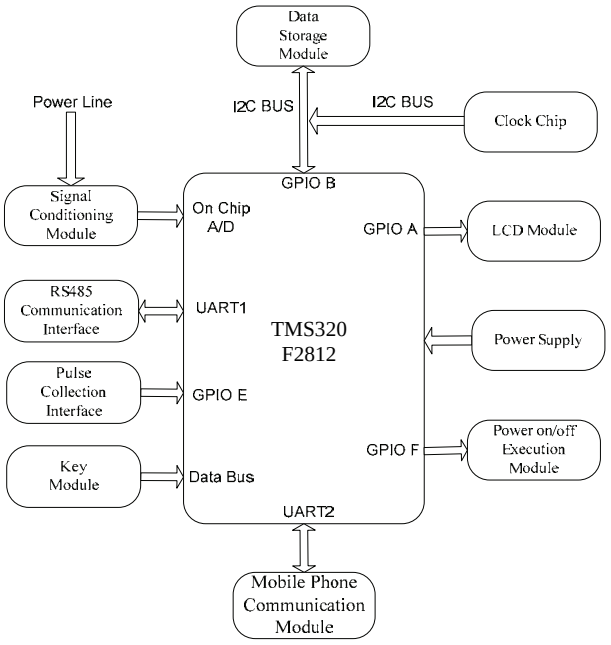

Figure 1. Hardware block diagram.

is highly integrated, high-performance solutions for demanding control applications [1].

LCD Module adopted 128*64 dot matrix LCD display, controlled by TMS320F2812's GPIOA. Because the processing speed of LCD is much slower than TMS320F2812, control signal is through the latch to control LCD. LCD refreshes every minute, displays the current power consumption and the current balance of user. It also can query information with the operation of the keys.

Key Module is connected to TMS320F2812's data bus, software control TMS320F2812 to scan data bus every 10 milliseconds. When a button is depressed, TMS320F2812 do corresponding processing according to data bus level changes.

Mobile Phone Communication Module adopted MC55 of SIEMENS, which is connected to TMS320 F2812's UART2. Administrator and user make SMS or GPRS remote operation to the device via the Mobile Phone Communication Module [3]. When the balance is insufficient, TMS320F2812 controls the module to use SMS to notify the user timely payment.

The device has two meter reading ports, RS485 Communication Interface and Pulse Collection Interface. RS485 Communication Interface connects to TMS320 F2812's UART1 via signal converter and optocoupler. UART1 sends a signal through the optocoupler and then through the signal converter to reach RS485 Communication Interface, RS485 Communication Interface receives a signal through the signal converter and then through the optocoupler to reach UART1. Pulse Collection Interface connects to TMS320F2812's GPIOE via optocoupler. When the pulse signal reaches GPIOE via optocoupler, TMS320F2812 gain electric energy information.

We use an EEPROM chip as Data Storage Module, Data Storage Module and Clock Chip is connected to TMS320F2812 via I2C Bus. Since TMS320F2812 has no hardware I2C Bus, using GPIOB simulate the I2C Bus Timing controlled by software. Data Storage Module stored device parameters information, user information and electricity consumption records. Clock Chip provides the device with time reference for time-billing.

Power on/off Execution Module is connected to TMS320F2812's GPIOF. The module is composed of optocoupler, relay and breaker. The controlling signals go through an optocoupler safety quarantined, and then go through the relay reach breaker, at last breaker responses the control signal.

Signal Conditioning Module is composed of CT and PT. The regulated signal followed by the filter circuit, voltage divider circuit. At last input TMS320F2812's on-chip A/D as differential mode to achieve Harmonic Measurement function.

Power Supply Module is composed of working power and backup power. Working power is obtained directly from the feeder and do battery charging at same time. Backup power is composed of battery.

2.2. Device SMS Function

The device can do Buy Operation, Inquire Operation, Power On/Off Operation, and Change Parameters Operation by SMS communication. It also can Send Alarm SMS on its own initiative.

Buy Operation means that administrator add user's balance by sending encrypted SMS. Inquire Operation means that administrator or user inquire balance by sending SMS. Power On/Off Operation means that administrator can make power on/off operation by sending encrypted SMS. Change Parameters Operation means that administrator can change electricity charge parameters by sending encrypted SMS [5]. Send Alarm SMS means that the device can send alarm SMS on its own initiative when the balance is less than some value.

The device stored some cell phone numbers. These numbers are divided into administrator number and user number. The device handles the messages as this flow: first Phone Number Analysis, then Operation Type Analysis, at last Response Operation. Received SMS processing flow is shown in **Figure 2**.

Phone Number Analysis means that, to judge the sender's number is administrator number or user number by comparing the sender's number with the numbers stored in the device. If the sender's number is not in the stored number list, delete this SMS, the device take no action.

Operation Type Analysis means that, the device gets

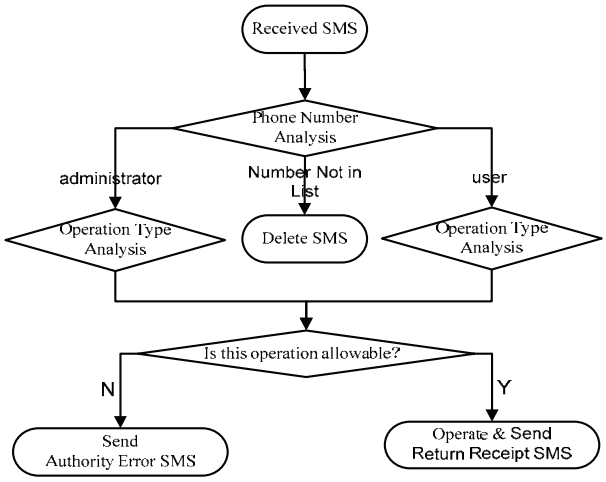

Figure 2. Received SMS processing flow.

operation information by analyzing SMS, and determines whether the operation is allowable. Administrator can do Buy Operation, Inquire Operation, Power On/Off Operation, and Change Parameters Operation. User can do Inquire Operation. If the SMS senders want to do limited operation, the device will return an authority error message to them.

Response Operation means that, the device makes different operations according to the type of operation. All operations have SMS receipt to inform the operator if the operation is successful or not.

In addition, the device send alarm SMS to administrator number and user number, when the balance is less than some value.

2.3. Device GPRS Function

The device also has GPRS communication function. Since the bytes of a SMS is limited, if we need to do a lot of data communication, using multiple SMS to communication is costly. For example, query operation history, query harmonic measurement records, in this case, the device communicates with the master station by GPRS.

3. Possible Commercial Applications

In this Pre-order Electricity System, PC master station controls a mobile phone communication module as an administrator with the Host Computer Software. Users carry mobile phones as a user number.

The device collects multiple Energy Meter's information via RS485 Bus. It can manage and control multiple meter users. In commercial applications, we do not need to replace the existing meter by Prepayment Energy Meter, just installing the Pre-order Electricity device on the basis of the existing system. The

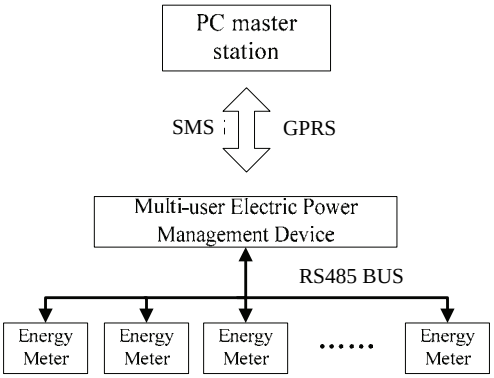

Figure 3. Application of multi-user electric power management device.

device used to collect Energy Meter's information, calculate electricity and achieve Pre-order Electricity functions. The possible application of Pre-order Electricity device is shown in **Figure 3**.

If the Energy Meter does not have RS485 Communication function, the device can collect electric energy information by Pulse Collection Interface. This situation the device can only manage one Energy Meter.

4. Conclusions

In this paper, we present a design of a Multi-user Electric Power Management Device. We use high-integrated and high-performance DSP TMS320F2812 as CPU, with peripheral devices such as mobile phone communication module MC55. The device can deal with complicated control information. It has three features:

1) Two kinds of electric energy information collect mode, it can manage and control multiple meter users.

2) Automatic calculation electricity charge based on different user information and electric energy information.

3) With the ability of remote operation via SMS and GPRS, and sending alarm information via SMS.

The device can be seamlessly integrated into the existing power system in order to read meter, achieve billing and Pre-order Electricity functions, can manage and control multiple meter users. In addition, the device has the Harmonic Measurement function. The application of the device can reduce the cost of the system reform, and it has been successfully used in Wuhu city of Anhui Province in China.

5. References

[1] Texas Instruments Incorporated, TMS320F281x Data Sheet, 2005.

[2] Texas Instruments Incorporated, TMS320F28x Optimizing C / C ++ Compiler User's Guide, 2005.

[3] SIEMENS Mobile, SIEMENS. MC55/56 Hardware Interface Description, 2006.

[4] SIEMENS Mobile, SIEMENS. MC55/56 AT Command Set, 2003.

[5] J. F. Wang, W. Q. Tao and L. L. Wang, "Design of Modify the Parameters of LTU by Using SMS," *Microcontrollers & Embedded Systems*, Vol. 6, 2009, pp. 40-42.

[6] Jiangsu Electric Power Company, Power Marketing Knowledge Q & A (Part of the electricity tariff), China Electric Power Press, Beijing, 2004.

[7] Z. B. Jiang, "Power Management/Technical Expertise for the Use of Electricity," China Electric Power Press, Beijing, 2002.

Energy and Power Engineering, **2010, 2, 131-136**
doi:10.4236/epe.2010.22019 Published Online May 2010 (http://www. SciRP.org/journal/epe)

Experimental Investigation of Unsteady Pressure on an Axial Compressor Rotor Blade Surface

Qingwei Wang, Bo Liu, Xiaorong Xiang, Xiangfeng Bo, Weimin Hou
School of Engine and Energy, Northwestern Polytechnical University, Xi'an, China
E-mail: *wqw@mail.nwpu.edu.cn*
Received March 16, 2010; *revised April* 21, 2010; *accepted* May 15, 2010

Abstract

The inherent unsteady pressure fluctuations on the rotating blade suction surface of an axial compressor were experimentally measured by directly mounting five high response miniature pressure transducers into the rotor blade along a streamline at 50% span respectively. The results show that the unsteady pressure fluctuations of rotor blade surface could be measured successfully by this means. The relations about the period, altitude of unsteady pressure with rotating speed, the discipline of pressure fluctuation along the streamwise direction were obtained.

Keywords: Kulite Transducer, Rotating Blade, Unsteady Pressure, Experimental Measurement

1. Introduction

It is well known that the flow fields in turbomachinery is inherently unsteady because of the aerodynamic blade row interaction, the viscous flows, secondary flows, tip clearance flows and so on. The efficiency of turbomachine blades and the overall performance of the machine strongly depend on the unsteady flow. Furthermore, the unsteady flow substantially influences blade forces and the high-cycle fatigue of blades. Therefore the research about unsteady pressure on blade surface, especially the rotor blade surface, is very necessary. During the past decades, an increasing experimental investigation of the unsteady pressure fluctuation on rotating blade surface have been carried out by directly embedding the high response miniature pressure transducers in rotor blades and got great successes [1-6].

In this paper, five high response miniature pressure transducers were directly mounted in the rotating blade of an axial compressor along a streamline at 50% span, to measure the unsteady pressure fluctuations on the rotor blade suction surface. During experiment, the data logger was fixed and rotated with the compressor axletree, which could directly sample, amplify and store the pressure signals.

2. Experimental Facilities

2.1. Axial Compressor Test Rig

The experimental study was conducted in a single stage axial compressor test rig at the Northwestern Polytechnical University, which consisted of 20 rotating blades and 23 stationary vanes, and work at the rotating speed from 0 to 3000 r/min. **Figure 1** shows the scheme of the axial compressor. Some the geometric data were: the tip radius was 290 mm, the hub radius was 174 mm, and the rotor blade tip clearance size was 1.0 mm. Design parameters of the compressor: design speed was 3000 r/min, mass flow was 5.97 kg/s, total pressure rise was 1870 Pa, and isentropic efficiency was 0.875. The compressor was driven by an AC motor (15 KW). The area of outlet was controlled by moving a throttle cone sited downstream of the test rig.

2.2. Pressure Transducer

Kulite model LQ-062 high response miniature pressure transducers were used in this study, as shown in **Figure 2**. The range of the transducer was ± 5PSI, sensitivity was 18.318 mV/PSI, and response frequency was 150 KHz. The pressure range of blade surface was about ± 0.5PSI relative to environmental pressure in this study, and the maximal response frequency of pressure fluctuations was low to 1000 Hz, so the transducers could content the experiment requirements. In order to prevent breaking the transducers during installing or taking down, the transducers were stuck into the guard sheaths firstly, and then be mounted into the holes drilled through the rotor blade. The scheme of guard sheath is shown in **Figure 3**. In the front of the guard sheath there was a hole with the diameter 2 mm where the transducer was installed. The

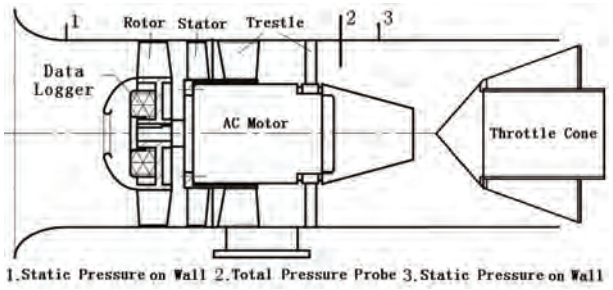

Figure 1. Axial compressor test rig.

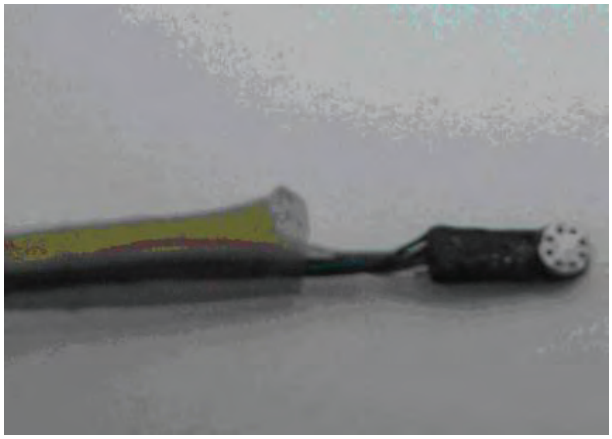

Figure 2. Kulite pressure transducer.

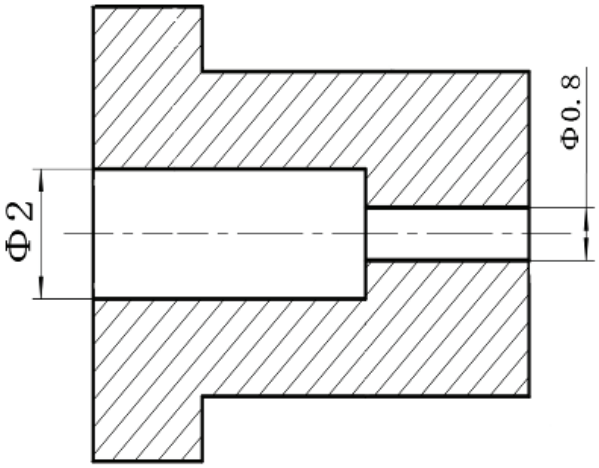

Figure 3. Guard sheath.

transducer sensed the pressure through a 0.8 mm diameter hole at another end of the guard sheath. The sketch of the transducer distributions is shown in **Figure 4**. Five transducers and guard sheaths were mounted at 5%, 20%, 40%, 60%, and 90% of axial chord position along the streamline at 50% span respectively. Just only five transducers were used in the investigation, to test and verify the experiment method and obtain some experiences. Next step, we will dispose more transducers on both the rotor suction and pressure surface, to obtain

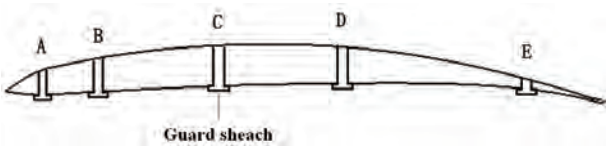

Figure 4. Distribution of pressure transducers.

more detailed unsteady pressure fluctuations on the rotor blade. The guard sheaths had some influence on flow fields of pressure surface side passage. However, the main purpose in this study was to measure the unsteady pressure on suction surface, and the suction surface configured a flow passage with the pressure surface of adjacent blade, so the effects of guard sheaths on the measurement flow fields were ignored.

2.3. Data Acquisition System

Figure 5 shows the data logger used in current study, which consisted of signal modulator, AD transform module, timer module, USB module and memorizer. The data logger had 8 channels and each channel sampled at the same time. The system sampling frequency was 100 KHz, the amplifying multiple was 186, and the memory capability was 1 G. The data would be continuously sampled for 10 minutes after the trigger infrared light aiming at the data logger. During experiment, the data logger was fixed and rotated with the drive shaft of the compressor as shown in **Figure 6**. The electrical wires of transducers were routed down along the blade pressure surface and through the hub to connect with the data logger, thus the data logger could supply powers for transducers. In additional, while the rotor was working, the data logger could directly amplified the electrical signals of transducers, and transform them to digital data, and then store to the memorizer. After the compressor stopping, the digital data stored in the memorizer was transferred to computer through a USB data line. Using the data logger could effectively avoid the distortion during data transmission and increased the data reliability.

3. Experimental Results and Discussion

In order to eliminate the electromagnetic interference of the AC motor, the shell of AC motor was connected with earth, and the electric wires of pressure transducers were shielded. In addition, the waves up 3000 Hz were sieved by software to reduce the effect of transducer noise signals, and that had little influence on the study. The interferences were weakened greatly by adopting the means above, which enhanced the reliability of pressure signals. The acquired dynamic pressure signals data consisted of time-average values and fluctuation values. For easy to analyze the unsteady pressure pulses, the time-average values was discarded from the gained signals data and

Figure 5. The data logger.

Figure 6. The fixing of data logger.

the fluctuation values was discussed only. The fluctuation values was defined using the following formula: $\tilde{p} = p - \overline{p}$. The $\tilde{p}$ was fluctuation value, the p was dynamic pressure sampled and the $\overline{p}$ was the time-average value of the sampled pressure using the formula $\overline{P} = (\sum_{i=0}^{n-1} P_i)/n$. Before experiment, the whole acquisition system had been static calibrated precisely, that ensure the veracity of the measurement results.

The unsteady pressure measurement covered different speeds and an extensive range of mass flow. The investigation focus on the inherent unsteady pressure on rotor blade suction surface, so there was no any disturb source in front of the rotor. **Figures 7-16** show the time-domain waves of 5 measurement points under 2000 r/min and 1000 r/min rotating speed while keeping the same outlet area. At the outlet area, the compressor was both near the peak value point of total pressure rise under 2000 r/min and 1000 r/min speed. From the figures it can be observed that the pressure fluctuations of rotor blade suction surface were periodical obviously. The period of waveforms at 2000 r/min speed was approximately 0.03 s, and was about 0.06 s at 1000 r/min speed. All these periods were just the times that the compressor revolving one circle at each rotating speed, which shows that the frequency response of inherent unsteady pressure were related to rotating speed. It is obviously that the altitudes of unsteady fluctuations declined as the rotating speed down. The maximal altitude of fluctuation was about 300 Pa at 2500 r/min speed, which was about 85 Pa at 1000 r/min speed. These show that the altitudes of the inherent pressure fluctuations were also related to the rotating speed. The periodical waveforms also contain some other complex pulses, which show the unsteady pressure fluctuations were very complicated. Because of the complication of unsteady flow fields, as well as the errors leading by the zero drift of transducers, each of the periodical waveforms is not absolutely the same with the other ones.

The reasons of blade surface unsteady pressure were various. The downstream stator was very far from the rotor. The axial distance between the rotor and stator was 268% of the rotor blade chord length at 50% span, so the stator gave little interaction to the flow fields of rotor blade passage. There were three main reasons of rotor blade surface unsteady pressure fluctuations. Firstly, although there were no any disturb source in front of the test rig, the flow fields of the blade passage was essentially unsteady because of the viscous flows, secondary flows, tip clearance flows and so on. Secondly, the inlet fairing of the compressor had a little warp and a bad concentricity, which resulted that the airflows passing by the inlet fairing and then flowing into the compressor were not absolutely uniform. Finally, there was a little vibration of test rig during experiment. As a result of fluid inherent characteristics, the inlet fairing and vibration of compressor, the pressure signals of the rotor blade surface were unsteady, and all the reasons were relate to the rotating speed, which were the reasons that the waveforms periods were approximately the same with the time compressor revolving one circle.

Figures 17-21 show the fairly typical time-domain waves and frequency spectral curves of 5 measurement transducers near peak value point of total pressure rise under 1500 r/min rotating speed. From the time-domain waves figures it can be observed that the waveforms periods of every measurement point were all approximately 0.04 s, which was the time the compressor revolving one circle. From the frequency spectral curves, it also can be seen that the dominant frequency was the fundamental frequencies of 25 Hz and its hormonics, which was the compressor rotating frequency. All these further prove that the periods of waveforms were related to rotating speed. From the frequency spectral curves, it can be

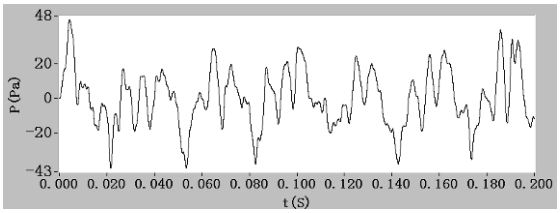

Figure 7. The time-domain waves of A under 2000 r/min.

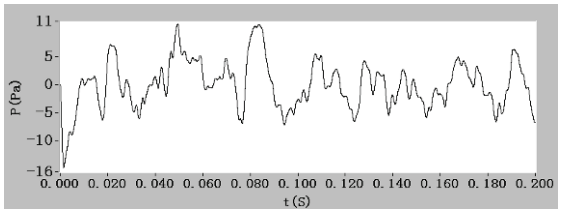

Figure 8. The time-domain waves of A under 1000 r/min.

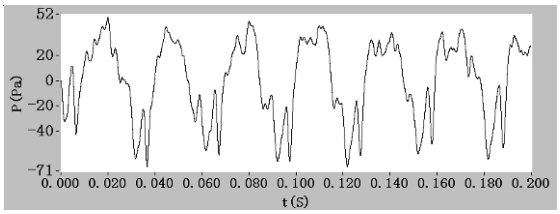

Figure 9. The time-domain waves of B under 2000 r/min.

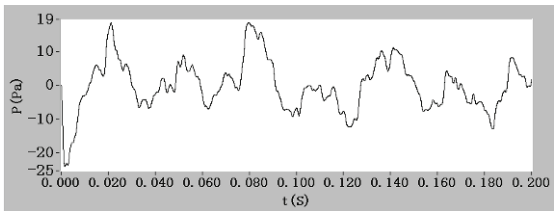

Figure 10. The time-domain waves of B under 1000 r/min.

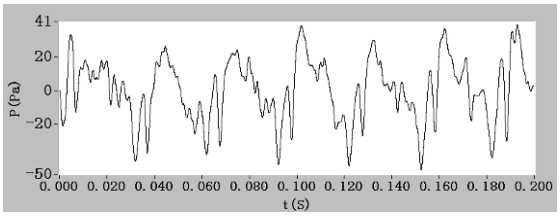

Figure 11. The time-domain waves of C under 2000 r/min.

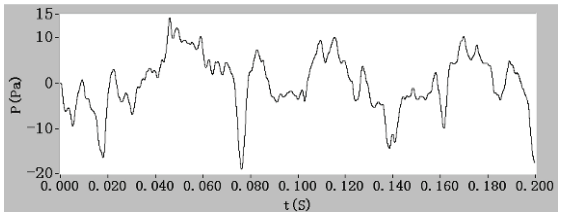

Figure 12. The time-domain waves of C under 1000 r/min.

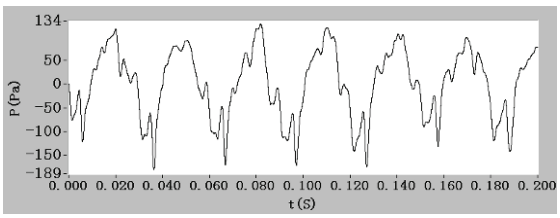

Figure 13. The time-domain waves of D under 2000 r/min.

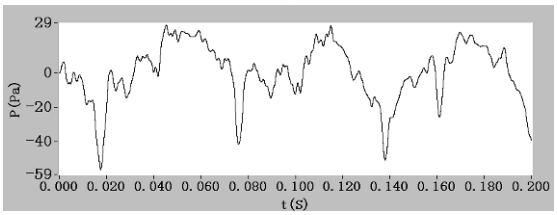

Figure 14. The time-domain waves of D under 1000 r/min.

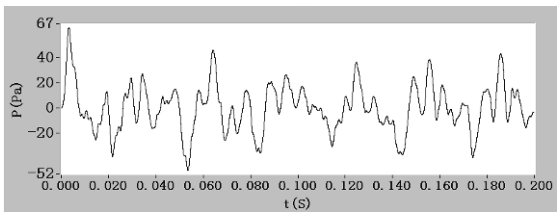

Figure 15. The time-domain waves of E under 2000 r/min.

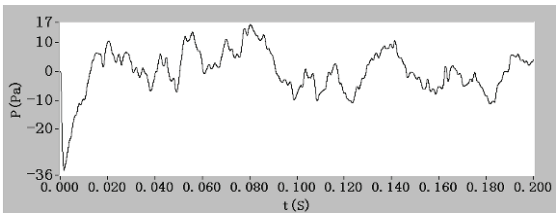

Figure 16. The time-domain waves of E under 1000 r/min.

seen that the peak values of the second, third, fourth and fifth order spectral were all remarkable at A point. From the relative Mach number contours at 50% span of the simulation as shown in **Figure 22**, it can be seen that the grads of the airflow velocity varied greatly near the blade leading edge, where the airflow began accelerating. Besides, the transducer at A point was located in the front of the blade, where the inlet no-uniform airflows had great influence. As a result of the two main reasons, the unsteady pressure fluctuation was complex at A point. **Figure 23** represents the peak values of the first order spectral of every measurement point. It was obvious that the peak values of the first order spectral gradually increased from A to D point, and then declined at E point. Because the blade surface pressure gradually increased from blade leading edge to trailing edge, accordingly the altitude of pressure fluctuation increased from A to D point. From **Figure 22** it can be seen that the boundary layers were thick near the blade trailing edge region, where the velocity and pulse of airflow were weak, so the boundary layers maybe the major contribution to the altitude of pressure fluctuation declining at E point.

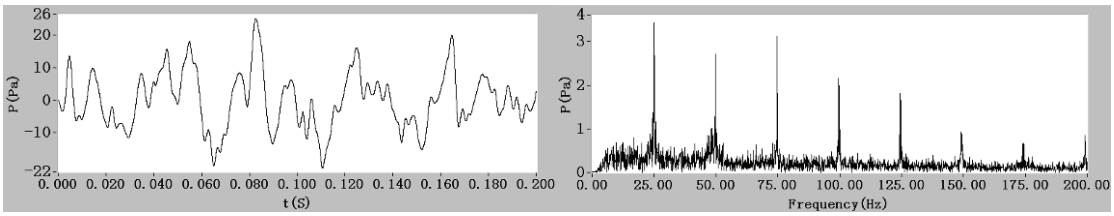

Figure 17. The time-domain waves and frequency spectral curves of A.

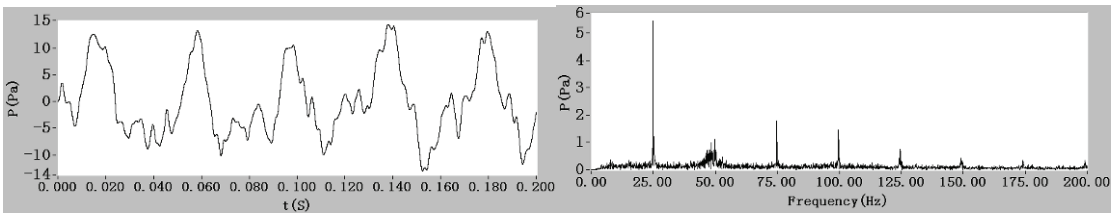

Figure 18. The time-domain waves and frequency spectral curves of B.

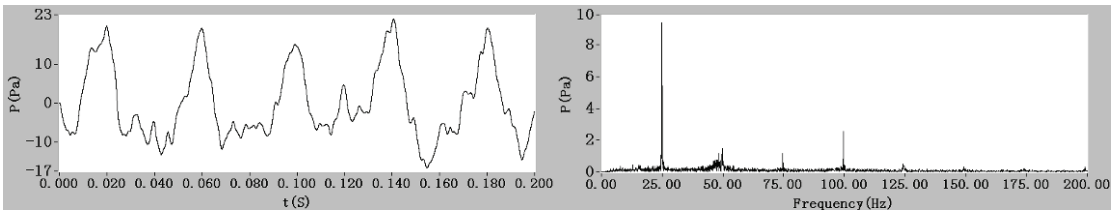

Figure 19. The time-domain waves and frequency spectral curves of C.

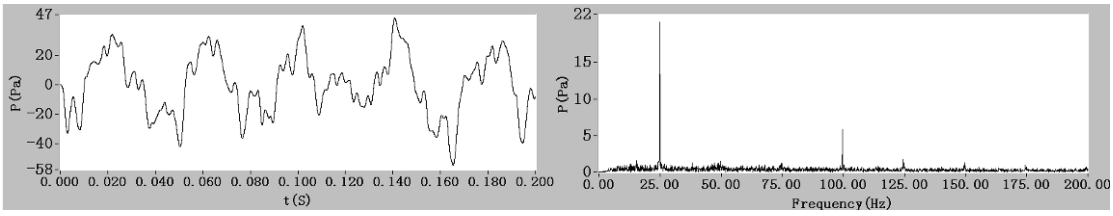

Figure 20. The time-domain waves and frequency spectral curves of D.

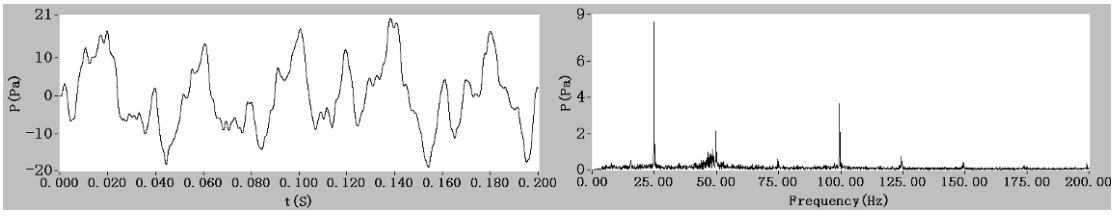

Figure 21. The time-domain waves and frequency spectral curves of E.

4. Conclusions

The unsteady pressure on rotor blade suction surface were measured using five miniature pressure transducers, directly mounted in the rotating blade along a streamline at 50% span. The results show:

1) The unsteady pressure fluctuations of blade surface could be measured successfully by this means. The pressure fluctuations were periodical obviously, and the periods and the altitudes of unsteady fluctuations were all related to the compressor rotating speed.

2) The periods of waveforms were the same with the time of compressor revolving one circle; the fluctuations were weakened as the rotating speed down.

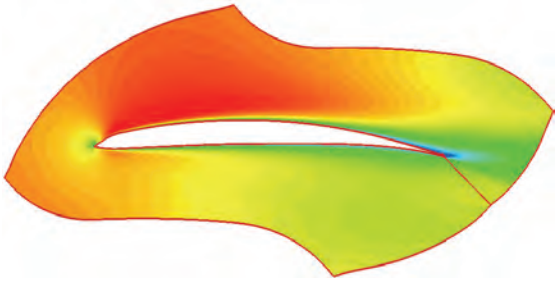

Figure 22. The relative mach number contours at 50% span.

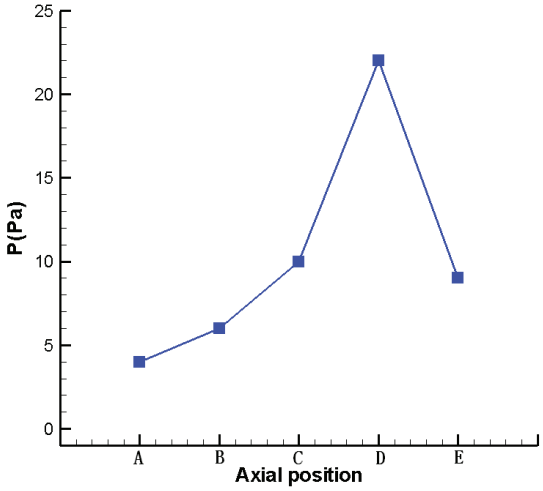

Figure 23. The peak values of the first order spectral.

3) The pressure fluctuations gradually increased from leading edge to trailing edge. But owing to the boundary layers near the blade trailing edge region, the fluctuations declined.

5. References

[1] Y. F. Wang, J. Hu, B. N. Luo and C. P. Li, "Effects of the Upstream Blade Wakes on the Spectrum of Rotor Blade Unsteady Surface Pressure," *Journal of Aerospace Power*, Vol. 21, No. 4, 2006, pp. 693-699.

[2] T. Maeda and H. Kawabuchi, "Surface Pressure Measurement on a Rotating Blade of Field Horizontal Axis Wind Turbine in Yawed Condition," *JSME International Journal Series B*, Vol. 48, No. 1, 2005, pp. 156-163.

[3] T. H. H. Carolus and M. Stremel, "Blade Surface Pressure Fluctuations and Acoustic Radiation from an Axial Fan Rotor Due to Turbulent," *Acta Acustica united with Acustica*, Vol. 88, No. 4, 2002, pp. 472-482.

[4] C. H. Sieverding, T. Arts, R. Denos and J. F. Brouckaert, "Measurement Techniques for Unsteady Flows in Turbomachines," *Experiments in Fluids*, Vol. 28, No. 4, 2000, pp. 285-321.

[5] R. W. Ainsworth, R. J. Miller, R. W. Moss and S. J. Thorpe, "Unsteady Pressure Measurement," *Measurement Science & Technology*, Vol. 11, No. 7, 2000, pp. 1055-1076.

[6] S. B. Yang, G. S. Song, J. Lin and K. M. Chen, "The Design of an Opti-Eletronic Pressure Measuring System for the Measurement of the Internal Flow Field in a Rotating Fan," *Journal of East China University of Technology*, Vol. 19, No. 2, 1997, pp. 41-51.

Call for Papers

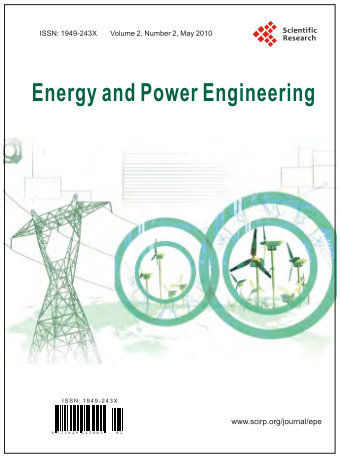

Energy and Power Engineering

ISSN 1949-243X (Print) ISSN 1947-3818 (Online)
http://www.scirp.org/journal/epe

Energy and Power Engineering(EPE), a quarterly journal, publishes research and review articles in all important aspects of electric power engineering and other professionals involved in the electric power industry. Both experimental and theoretical papers are acceptable provided they report important findings, novel insights, or useful techniques in these areas.

Editor in Chief

Editorial Advisory Board

Editorial Board

Subject Coverage

EPE aims to strengthen relations between the energy sector, research laboratories, and universities. Additionally, accepted ones will immediately appear online followed by printed in hard copy. The topics to be covered by Energy and Power Engineering include, but are not limited to:

- ◆Power Generation - Conventional and Renewable
- ◆Power System Management
- ◆Power Transmission and Distribution
- ◆Smart Grid

We are also interested in short papers (letters) that clearly address a specific problem, and short survey or position papers that sketch the results or problems on a specific topic. Authors of selected short papers would be invited to write a regular paper on the same topic for future issues of the EPE.

Notes for Intending Authors

Submitted papers should not have been previously published nor be currently under consideration for publication elsewhere. Paper submission will be handled electronically through the website. All papers are refereed through a peer review process. For more details about the submissions, please access the website.

Website and E-Mail

http://www.scirp.org/journal/epe **Email: epe@scirp.org**

Energy and Power Engineering, 2010, 2, 73-136
Published Online May 2010 in SciRes (http://www.SciRP.org/journal/epe/)

TABLE OF CONTENTS

Volume 2 Number 2 **May 2010**

